

**Design and Optimization of a Compliant Parallel
Robotic Surgical Instrument with Multifunctional
Forceps for Minimally Invasive Surgery**

by

Rifeng Hu

A Thesis Submitted in Partial Fulfillment

of the Requirements for the Degree of

Master of Applied Science

in

the Faculty of Engineering and Applied Science

Mechanical Engineering Program

University of Ontario Institute of Technology

November 2015

© Rifeng Hu, 2015

Abstract

Minimally Invasive Surgery (MIS) technique has seen its great success in the last few decades due to its significant advantages compared to the traditional open surgeries.

This technique requires only a few 10 mm incisions through which the surgical instruments can be inserted to perform operations inside the human body. The benefits it brings to surgeons and patients are so obvious that recent advances in MIS continue to demand the development of surgical tools for different types of MIS.

This thesis presents a surgical instrument based on compliant parallel mechanism with multifunctional forceps attempting to overcome the problems arise from the advances in MIS. Due to the inherent properties of compliant mechanism, the surgical tool can be designed very compact to meet the strict requirements of MIS with very restricted operation area. With parallel mechanism, this tool has multiple degrees of freedom and the stiffness to transmit motions dexterously and accurately. By integrating the PCB motor, the end-effector is able to rotate 360 degrees. The parallel mechanism was analyzed in terms of kinematics, workspace and stiffness modeling. Workspace and stiffness were optimized using Genetic Algorithm to get the optimal performance out of this parallel mechanism.

The multifunctional forceps with the functions of scissor-cutting, grasping and Cautery was also designed. The CAD model was constructed and Finite Element Analysis was conducted to make sure that the design meets the requirements.

Acknowledgements

First and foremost, I would like to thank my supervisor, Dr. Dan Zhang, for his guidance and continuous support through my research, without which my thesis could have never been completed. Under his supervision, it was a great experience to research in the field of parallel mechanism. I would also like to thank Dr. Zhang for his financial support during my Master program and giving me such a valuable opportunity to do my research in Robotics and Automation Laboratory at UOIT.

I would also like to thanks to my colleagues in Robotic and Automation Laboratory. The discussion with Mr. Xudong Wang helped me a lot to develop the ideas towards this thesis. Dr. Yaobin Tian also helped me a lot with MATLAB codes debugging. Thank for their help and support and making the lab a very friendly environment to study and research.

Last but not least, I would like to express my gratitude to my family. Thank you all for your support.

Contents

Abstract.....	I
Acknowledgements.....	II
Contents	III
List of Figures	VI
List of Tables.....	XI
Nomenclature.....	XII
Chapter 1 Introduction	1
1.1 Background.....	1
1.2 Literature Review.....	4
1.2.1 MIS surgical instruments	4
1.2.2 Compliant mechanisms for MIS	7
1.2.3 Lamina Emergent Mechanisms.....	8
1.2.4 Multifunctional surgical forceps	11
1.3 Motivation and Objectives	14
1.4 Outline.....	15
Chapter 2 Design and Analysis of the Compliant Parallel Robotic Surgical Instrument	17
2.1 Introduction.....	17
2.2 Proposed Design Scheme 1 of the Surgical Instrument.....	18
2.2.1 Conceptual Design.....	18

2.2.2 Simulation of Deflection of the Bending Mechanism	20
2.3 Proposed Design Scheme 2 of the Surgical Instrument.....	21
2.3.1 Compliant Parallel Robot Geometric Structure	22
2.4 Kinematics Analysis.....	26
2.4.1 Mobility Analysis.....	26
2.4.2 Inverse Kinematics.....	27
2.4.3 Workspace Evaluation.....	34
2.5 Jacobian Matrix.....	39
2.6 Summary	42
Chapter 3 Stiffness Modeling	43
3.1 Introduction.....	43
3.2 Stiffness Modeling of One Limb	48
3.3 Stiffness Modeling of the Compliant Parallel Mechanism	55
3.4 Stiffness mapping and Discussions.....	56
3.5 Summary	59
Chapter 4 Optimization of the Compliant Parallel Robotic Surgical Instrument	60
4.1 Introduction.....	60
4.2 Constraints and Optimization Setup	63
4.3 Optimization of the Workspace.....	64
4.4 Optimization of the Stiffness	68
4.5 Multiobjective Optimization.....	70
4.6 Summary	72

Chapter 5 Design and Analysis of the Multifunctional Forceps	74
5.1 Introduction.....	74
5.2 Multifunctional Forceps Geometric Structure and Design	75
5.3 Design Constraints and Parameters	77
5.4 Finite Element Modeling of the Multifunctional Forceps	79
5.5 Integration of Cautery Ability	84
5.6 Summary	88
Chapter 6 Conclusions, Contributions, and Future Work	89
6.1 Conclusions.....	89
6.2 Contributions.....	91
6.3 Future Work	93
References.....	96

List of Figures

Figure 1.1. Laparoscopic surgery.....	2
Figure 1.2. Inflated workspace and camera view.....	2
Figure 1.3. Laparoscopic cholecystectomy procedure and open cholecystectomy procedure.	3
Figure 1.4. Incision comparisons between open surgery and MIS through da Vinci system	4
Figure 1.5. Figure1.5. Da Vinci surgical system, Intuitive Surgical Inc., 1999.....	5
Figure 1.6. The Radius Surgical System. (A) Overview. (B) Deflection tip	6
Figure 1.7. A CAD model of the compliant kidney gripper	8
Figure 1.8. Prototype of outer shell type 2 DOF bending manipulator using spring-link mechanism	8
Figure 1.9. A SMA sheet metal used to achieve an out-of-plane moment, where the direction of the moment is indicated by the arrow	10
Figure 1.10. A MLEM composed of a crank-slider attached to a parallel-guiding mechanism, where the in-plane actuation force is indicated by the arrow	10
Figure 1.11. A MLEM composed of multiple crank-sliders, a spring, and a platform, where the in-plane actuation moment is indicated by the arrow	11
Figure 1.12. Scissors-Grasper-Articulator End-Effector. Closed (A), grasper open (B), scissors open (C), closed articulated (D), open articulated (E)	12
Figure 1.13. Compliant Scissors-Grasper End Effector. Closed (A), grasper open (B),	

scissors open (C), textured jaw surface (D).....	13
Figure 1.14. Multifunctional compliant scissors-forceps design.....	13
Figure 1.15. The design incorporating two sets of actuating wires	14
Figure 2.1. Scheme 1 Bending manipulator with compliant grasper jaws	19
Figure 2.2. Simulation of the deflection of the proposed mechanism driven by a pair of differential forces in opposite directions.	21
Figure 2.3. A 3D model of the conceptual design of the compliant parallel robotic surgical instrument with multifunctional forceps for MIS	22
Figure 2.4. A 3D model of the compliant parallel mechanism	23
Figure 2.5. A 3D model of the multifunctional forceps attached to its base.....	24
Figure 2.6. Simulation result of displacement of the compliant parallel mechanism...	24
Figure 2.7. Kinematically equivalent diagram of the compliant parallel mechanism ..	29
Figure 2.8. Workspace and volume (Top trimetric view), with $l_b = 13$ mm, $r_b = 13$ mm, $r_p = 12$ mm.	35
Figure 2.9. Workspace and volume (Bottom trimetric view), with $l_b = 13$ mm, $r_b = 13$ mm, $r_p = 12$ mm.....	36
Figure 2.10. Workspace and volume (Top trimetric view), with $l_b = 13.5$ mm, $r_b = 13$ mm, $r_p = 12$ mm.....	36
Figure 2.11. Workspace and volume (Bottom trimetric view), with $l_b = 13.5$ mm, $r_b =$ 13 mm, $r_p = 12$ mm.....	37
Figure 2.12. Workspace and volume (Top trimetric view), with $l_b = 13.5$ mm, $r_b = 13.5$ mm, $r_p = 12$ mm	37

Figure 2.13. Workspace and volume (Bottom trimetric view), with $l_b = 13.5$ mm, $r_b = 13.5$ mm, $r_p = 12$ mm.....	38
Figure 2.14. Workspace and volume (Top trimetric view), with $l_b = 13.5$ mm, $r_b = 13.5$ mm, $r_p = 12.5$ mm.....	38
Figure 2.15. Workspace and volume (Bottom trimetric view), with $l_b = 13.5$ mm, $r_b = 13.5$ mm, $r_p = 12.5$ mm.....	39
Figure 3.1. Right-circular flexure hinge and its local frame.....	44
Figure 3.2. Right-circular flexure hinge and its local frame.....	45
Figure 3.3. A serial chain	48
Figure 3.4. A parallel mechanism with local and reference coordinates	50
Figure 3.5. The link–pair relationship diagram of the compliant parallel mechanism.	51
Figure 3.6. Geometry relationships among coordinate systems	52
Figure 3.7. Geometry relationships among coordinate systems	55
Figure 3.8. Stiffness factor f_x - u_x versus parameters l_b and l_c	57
Figure 3.9. Stiffness factor f_y - u_y versus parameters l_b and l_c	57
Figure 3.10. Stiffness factor f_z - u_z versus parameters l_b and l_c	58
Figure 4.1. Schematic representation of the optimization rationale based on Genetic Algorithms	62
Figure 4.2. Optimization of workspace using MATLAB optimization toolbox	65
Figure 4.3. Optimization result of workspace.....	66
Figure 4.4. Optimization result of workspace.....	67
Figure 4.5. Optimized workspace and volume (view from the top).....	67

Figure 4.6. Optimized workspace and volume (view from the bottom).....	68
Figure 4.7. Stiffness optimization and the results.....	69
Figure 4.8. Stiffness optimization and the results.....	69
Figure 4.9. Multiobjective optimization and results	71
Figure 4.10. Pareto front data plot of multiobjective optimization results.....	71
Figure 4.11. Exported Pareto Front data, stiffness results after optimization.....	72
Figure 5.1. 3D model of the multifunctional forceps mounted on the upper base, actuated by a linear piezoelectric motor	76
Figure 5.2. 3D model of the fixed jaw (left), and the moving jaw (right)	77
Figure 5.3. Side view of the 3D model of multifunctional forceps-scissors	77
Figure 5.4. Representation of the jaw design with parameters.....	78
Figure 5.5. Jaw geometry with small teeth (left), FEA model geometry without small teeth (right)	80
Figure 5.6. 2N force is applied to the grasping surface and the fixed jaw was fixed at the pin hole and meshed.....	81
Figure 5.7. FEA result of stress distribution of the fixed jaw	82
Figure 5.8. FEA result of displacement (left) and strain distribution (right) of the fixed jaw.....	82
Figure 5.9. 2N force is applied to the grasping surface and the moving jaw was fixed at the pin hole and meshed.....	83
Figure 5.10. FEA result of stress distribution of the fixed jaw	83
Figure 5.11. FEA result of displacement (left) and strain distribution (right) of the	

fixed jaw	84
Figure 5.12. Diagram of current paths for unipolar Cautery technique.....	86
Figure 5.13. Applications of different current frequencies.....	86
Figure 5.14. Common voltage waveform outputs for electrosurgical generators	87
Figure 5.15. Tip of the instrument with forward pushed rod in coagulating position ..	88

List of Tables

Table 2.1. Input angles (unit radian) at a specifically given position for example.	33
Table 2.2. Parameters of the mechanism for preliminary design.....	33
Table 3.1. Factors of the Compliance matrix of right-circular flexure hinge.	46
Table 3.2. Factors of the Compliance matrix of right- circular flexure spherical hinge..	47
Table 4.1. Boundaries of the geometric parameters to be optimized (mm).....	33
Table 5.1. Relevant material properties for 316 stainless steel.....	80

Nomenclature

B_i Vertices of the triangle in fixed base

c Cosine function

C Compliant matrix

E Young's modulus

F Number of degree of freedom

F External force

f_i Number of degrees of freedom permitted by joint i

j Number of joints

J Jacobian matrix

K Stiffness matrix

l_a Length of link a

l_b Length of link b

l_c Length of link c

l_d Length of link d

l_e Length of link e

P_i Vertices of the triangle in moving platform

q Vector described the actuated joint variables

r_i Position vector

r_b Radius of base

r_p Radius of platform

R Rotation matrix

s Sine function

S Skew-symmetric operator

T Transformation matrix

Greek Letters

α_i Angles between GP_i and the axis Gu, Gv, Gw

λ Degree of freedom of each unconstrained individual body

ν Poisson's ratio

σ_y Yield strength

Coordinate System

$G\{u, v, w\}$ Coordinate frame attached to the moving platform

$O\{x, y, z\}$ Coordinate frame attached to the fixed base

$(\theta_x, \theta_x, \theta_y)$ Orientation of moving platform with respect to reference frame

Acronyms

CPM Compliant Parallel Mechanism

DOF Degree of Freedom

EDM Electrical Discharge Machining

GA Genetic Algorithm

LEM Lamina Emergent Mechanism

Max Maximize

MIS Minimally Invasive Surgery

Chapter 1 Introduction

1.1 Background

Minimally Invasive Surgeries (also known as minimally invasive procedures) refer to surgical techniques that limit the size of incisions needed and so lessen wound healing time, associated pain and risk of infection [1]. Since Dr. J. Barry McKernan successfully performed the first laparoscopic cholecystectomy in the United States of America in 1988, by cutting a 10 mm incision, inserting a miniature camera into a patient's abdomen and removing a gall bladder, the minimally invasive surgery (MIS) has made great advance and been researched extensively for the last three decades. It is considered as one of the most promising trends for surgical procedures [2-4].

Laparoscopic surgery as shown in Figure 1.1, a type of MIS, is a procedure performed through incisions 5-12 mm in diameter. Surgeons insert the needed surgical instruments through trocars after obtaining enough workspace below abdominal wall, and operate instruments to perform procedures under laparoscopic control [5]. The abdomen is inflated with carbon dioxide gas in order for the surgeons to have sufficient workspace while performing procedures [4], as shown in Figure 1.2.

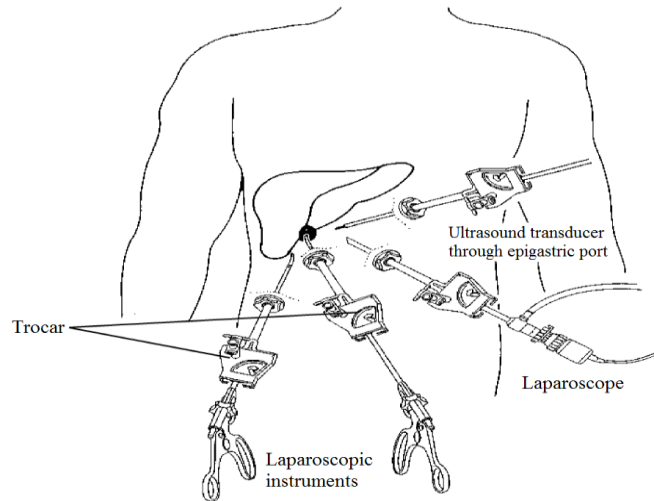


Figure 1.1. Laparoscopic surgery [6].

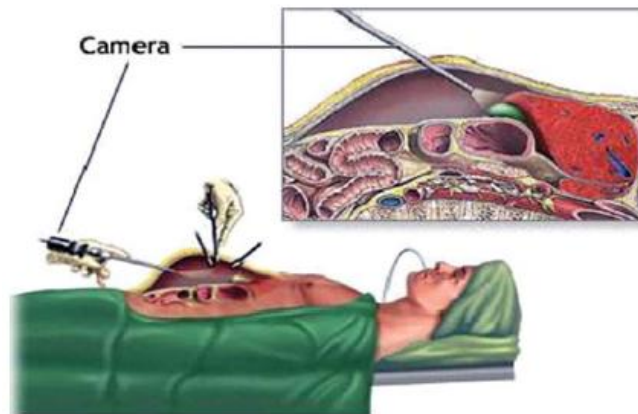


Figure 1.2. Inflated workspace and camera view [7].

Traditional open surgery as shown in Figure 1.3 requires a large incision to fully expose the surgical site for surgeons to reach the organs of patients. The hole must be large enough to fit the surgeons' hands and surgical instruments in patients' body. Besides, surgeons visualize the surgery through the hole as well. Since the surgeons remain a wide hole while performing the surgery and it is very likely that the patients get infected. After the surgery, patients may need a much longer time to stay at the hospital to recover, during which patients may suffer from huge pain and complications that sometimes are deadly. However, MIS allows the incision much

smaller, thus reducing the surgical invasiveness to patients. The benefits it brings are obvious.

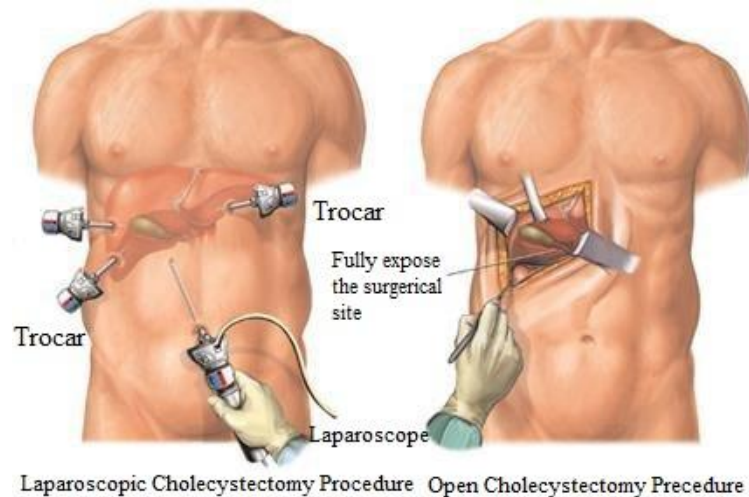


Figure 1.3. Laparoscopic cholecystectomy procedure and open cholecystectomy procedure [8].

First of all, MIS reduces surgical trauma leading to better outcome and shorter recovery time compared with that achieved by traditional open surgery. Since the incisions are small instead of one single large one in conventional open surgery as depicted in Figure 1.4, MIS further decreases the probability of infections and thus the patients have less need in high-intensity nursing care. Besides, due to their shorter recovery time, for example, from 10 to 3.5 days for cholecystectomy [9, 10], patients may save money and time by shortened hospital stays. Finally, they can return to daily life earlier. Because of these advantages, it is desired that such technique should be improved and implemented when possible to benefit both the surgeons and the patients [11-13].

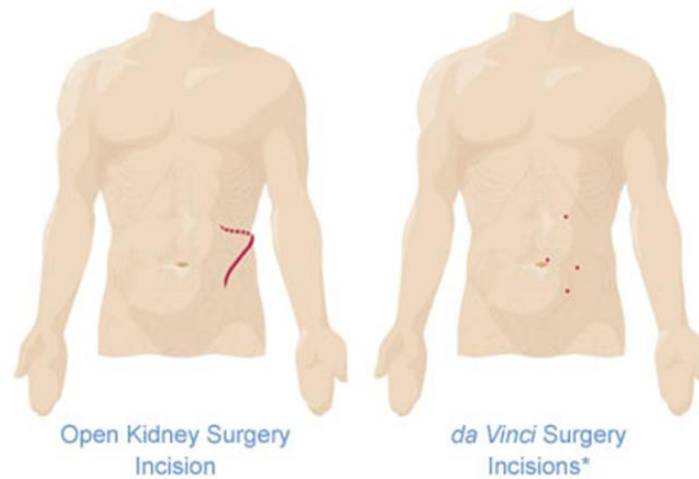


Figure 1.4. Incision comparisons between open surgery and MIS through da Vinci system [14].

1.2 Literature Review

1.2.1 MIS surgical instruments

In order to apply this MIS technique to more types of surgeries with better outcomes even under critical medical situations, different surgical systems and instruments have been extensively researched and developed by researchers and scientists. Among them, there are quite a few successful examples being used widely in all kinds of MIS worldwide, which provide significant insights to developing new systems and instruments. However, there are also many limitations along with them which should be avoided or tackled.

The challenges of MIS come from the very limited workspace and complex

operations to be done inside the human body through a few millimeters diameter incisions. Therefore, a robotic system named the da Vinci system was developed and introduced to MIS, attempting to cope with these shortcomings. Such robotic system provides humanlike dexterity and a high resolution three dimensional endoscopic image allowing the surgeon sitting on the console to control the robot arms to conduct the surgical procedures, as shown in the Figure 1.5. However, one such system costs over \$ 1 million making it unaffordable for most medical departments.

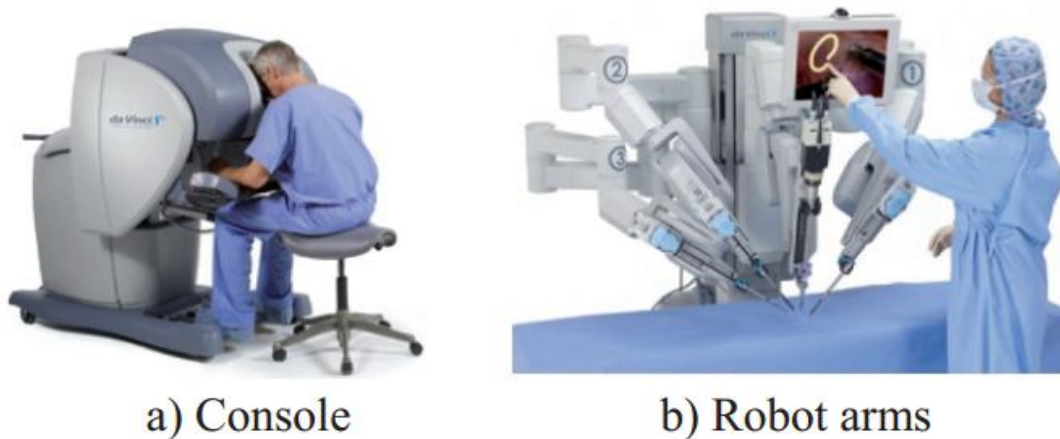


Figure1.5. Da Vinci surgical system, Intuitive Surgical Inc., 1999 [15].

Despite the fact that da Vinci system is very expensive and unaffordable most of the time, surgeons have the lack of the force feedback and the sense of distance when performing surgeries on the console. In addition, it takes a big amount of time for surgeons to get training before applying this technique to medical applications. Therefore, it is reasonable to develop handheld instruments with multiple degrees of freedom which can also improve the outcomes of MIS if these instruments are properly designed. Meanwhile, lots of work have been done in this field and it is proven that handheld instruments lead the trend in the field of surgical instruments

development for MIS.



Figure 1.6. The Radius Surgical System. (A) Overview. (B) Deflection tip. (C) Rotation of the tip [16].

Figure 1.6 shows a device for MIS in urology developed by the Radius Surgical System. This system offers the advantages of conventional laparoscopy (low costs, tactile feedback) combined with the advantages of robotics (greater degrees of freedom, short learning curve) [16].

1.2.2 Compliant mechanisms for MIS

Generally, most instruments used in MIS nowadays are very complex with many interacting mechanical components [17]. This design has the disadvantages of decreased dexterity, reduced force feedback, nonintuitive control, etc., leading to compromises in surgical technique [18]. In addition, the complexity of this design increases the number of parts, which in turns increases the time spent in arriving at a suitable design and increases the cost of manufacturing and assembly [19]. However, if surgical instruments are designed utilizing compliant mechanisms, they can offer many potential advantages over traditional MIS instruments [18], including reduced wear/friction, reduced maintenance, increased precision, increased reliability, scalable, and fewer assembly steps. Therefore, many researchers have been doing research in the field of compliant mechanism with which they are attempting to overcome these drawbacks and improve MIS.

Kota et al. designed and constructed a compliant organ (kidney) gripper (Figure 1.7) for use in MIS [18]. Due to the compliance of the fingers, they can be contained within a tube with small diameter to make the invasiveness minimal, which demonstrates the advantages of monolithic, flexible tool. Arata et al. developed an outer shell type 2 DOF bending manipulator using a spring-link mechanism for a surgical robot, as shown in the Figure 1.8 [20]. The spring-link mechanism consists of a flat spring and a rigid link. They are connected by a passive joint connection. Designs based on compliant mechanisms can be found in the literatures [21-24].

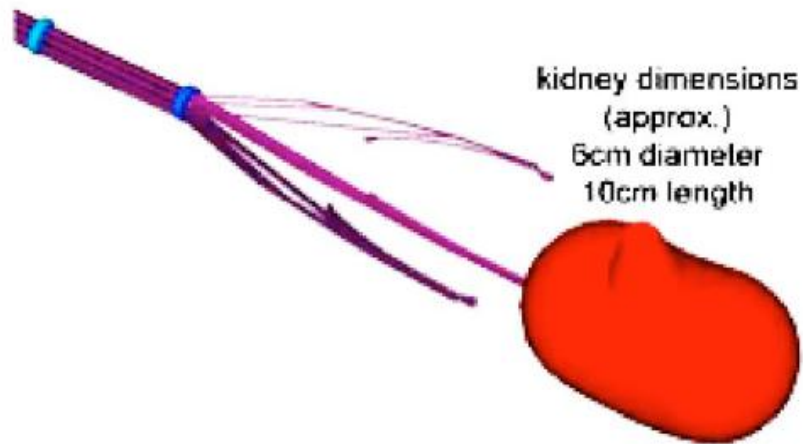


Figure 1.7. A CAD model of the compliant kidney gripper. Beam cross sections are all 3 mmx0.9 mm [18].

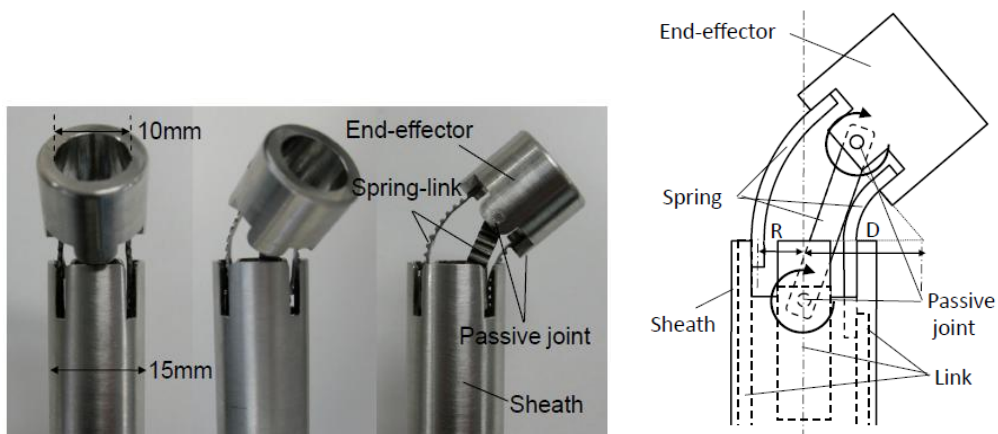


Figure 1.8. Prototype of outer shell type 2 DOF bending manipulator using spring-link mechanism [19].

1.2.3 Lamina Emergent Mechanisms

Lamina emergent mechanisms (LEMs) are compliant mechanisms that are manufactured from planar materials (Lamina) and have motions that emerge out of the manufacturing plane [25, 26], as shown in Figure 1.10. LEMs achieve their

motions from the deflection of flexible members like other compliant mechanisms, and have the same advantages. They can be fabricated in plane through cost-efficient processes, such as stamping, blanking, punching, etc. The LEMs planar nature reduces the costs in shipping as well as storage [25]. Some sophisticated components and miniaturized parts with high precisions can be achieved through wire electrical discharge machining (EDM), making it well suited for MIS applications, where really compact instruments with high dexterity and highly flexible tools are desired. Once the desired operation location is arrived, they can be deployed and used in highly constrained space.

Jacobsen et al. presented the Lamina Emergent Torsional Joint to allow LEMs to achieve large angular rotation, where high off-axis stiffness is not so critical [28]. The approach of Pseudo-Rigid Body Model was used to analyze the stiffness of LET, and support the design of LET. Figure 1.10 shows a 4-bar LEM with LET joints. Wilding et al. introduced planar compliant joints for LEMs and improved off-axis stiffness in tensile and/or compressive stiffness [29]. Winder et al. studied joints suitable for LEMs [30], thus further facilitating the design of LEMs. Ferrell explored joints with particular application to metal LEMs [31]. Gollnick et al. investigated different actuation approaches including shape memory alloys, piezoelectric, and dielectric elastomers to set Multi-layer LEMs to motion [27]. The exploration and research of LEM joints and actuation approaches is important for the applications of LEMs in various situations.

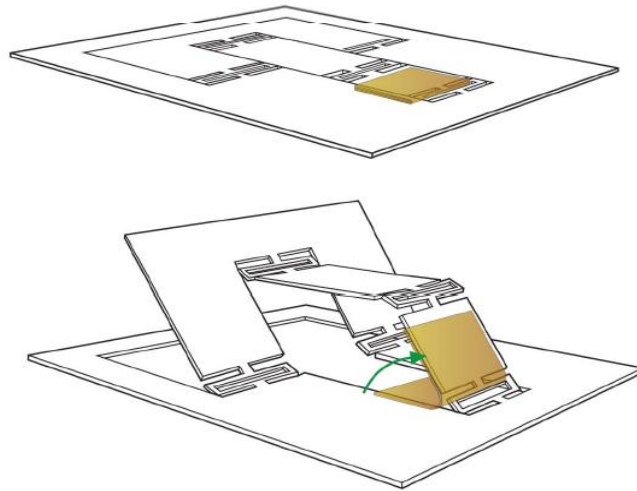


Figure 1.9. A SMA sheet metal used to achieve an out-of-plane moment, where the direction of the moment is indicated by the arrow [27].

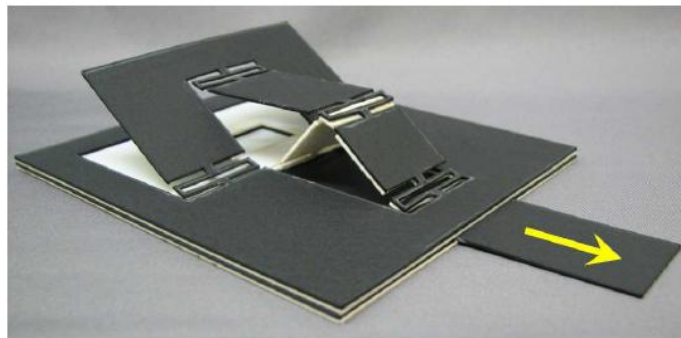


Figure 1.10. A MLEM composed of a crank-slider attached to a parallel-guiding mechanism, where the in-plane actuation force is indicated by the arrow [27].

In addition to single-layer LEM, Multi-layer LEM (MLEM) could be formed by adding new layers to it (see Figure 1.11, 1.12). Since MLEM are formed by additional single layers, interactions between these layers offer MLEMs enhanced capabilities [32]. However, with the enhancement of capabilities, the complexity of MLEMs also increases.

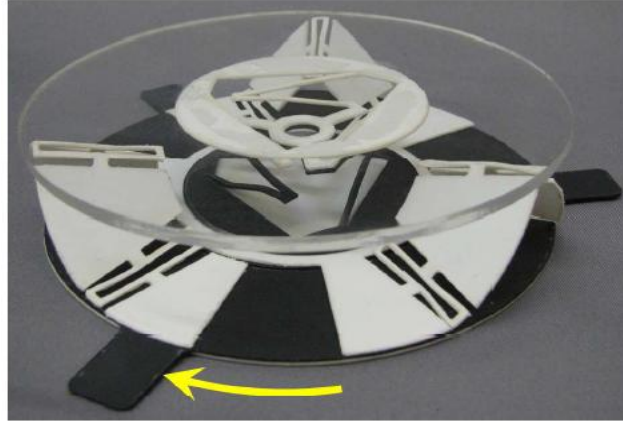


Figure 1.11. A MLEM composed of multiple crank-sliders, a spring, and a platform, where the in-plane actuation moment is indicated by the arrow [27].

1.2.4 Multifunctional surgical forceps

Surgical instruments are constantly exchanged throughout the MIS procedures, such as the frequent exchanges between forceps and scissors. Instrument exchanges add extra procedure time to total time by 10% to 30% [33], making the surgeons less efficient. The exchanges may also disrupt the surgeon's train of thought, damage healthy tissues or organs, and potentially compromise the patient's safety [34].

Therefore, in order to reduce the total surgery time, to improve the efficiency, and to decrease the possibility of compromising patients' health and safety, it is desired that multifunctional instruments, which are able to conduct more than one task with a single set of working jaws [35], for example, one single instrument providing both scissors and forceps functions, to be developed and used in MIS. Such advance will further support developing MIS.

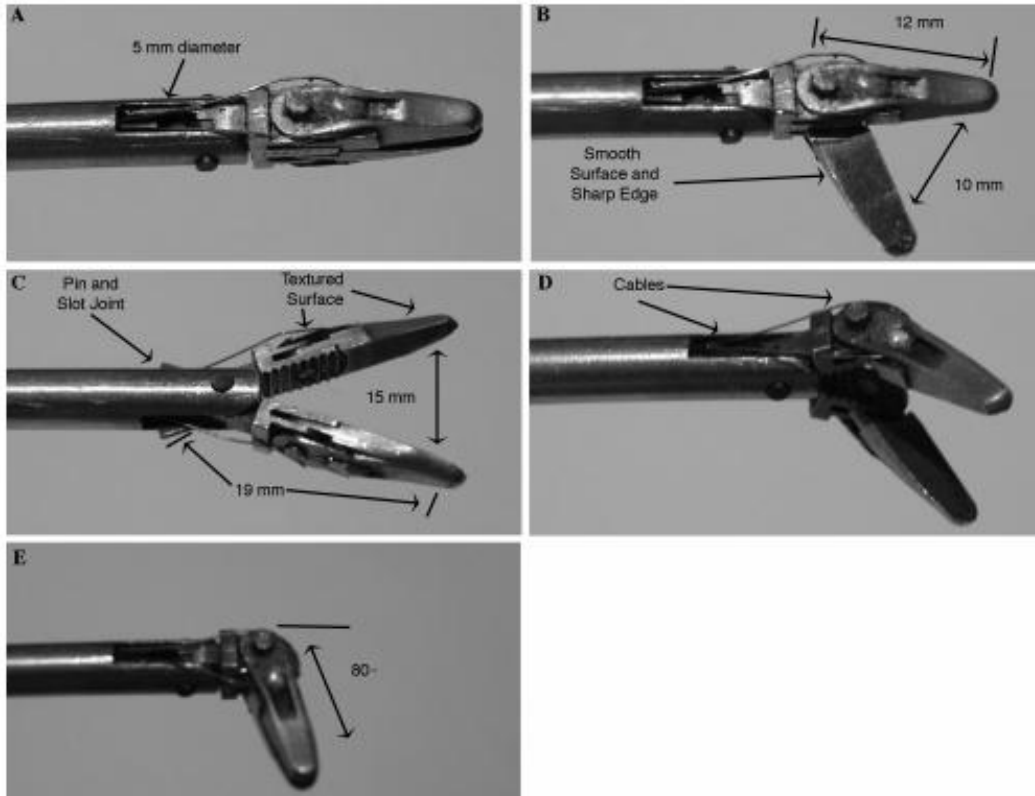


Figure 1.12. Scissors-Grasper-Articulator End-Effector. Closed (A), grasper open (B), scissors open (C), closed articulated (D), open articulated (E) [35].

Multifunctional instruments with forceps and scissors functions are identified as useful, as they can cut, dissect, and hold tissue without exchanges between different tools [36]. Frecker et al. [35] designed and tested multifunctional instruments designed by conventional rigid links and hinges (Figure 1.13)]. Frecker et al.[35] also investigated compliant multifunctional tools as presented in Figure 1.14. Aguirre et al. [37] developed and optimized a 1.0 mm multifunctional compliant forceps-scissors surgical instrument as shown in Figure 1.15. With the housing sheath advancing and rotating, it realizes both grasping and cutting functions. Such design simplifies the manufacturing and assemblies by making the working jaws compliant and monolithic. Figure 1.15 shows a 3.0 mm diameter multifunctional forceps for use in endoscopic

surgery by Rau et al.. Design and experiments are presented to demonstrate multifunctional capabilities, which include grasping, spreading, and cauterizing [39].

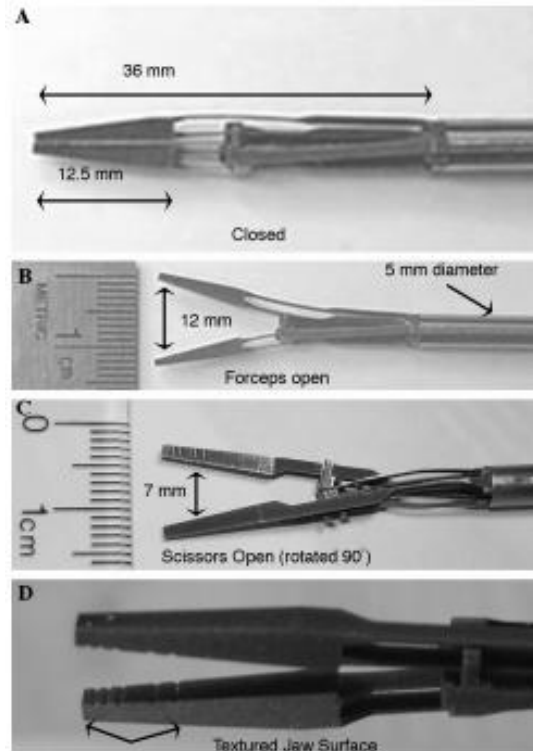


Figure 1.13. Compliant Scissors-Grasper End Effector. Closed (A), grasper open (B), scissors open (C), textured jaw surface (D) [35].

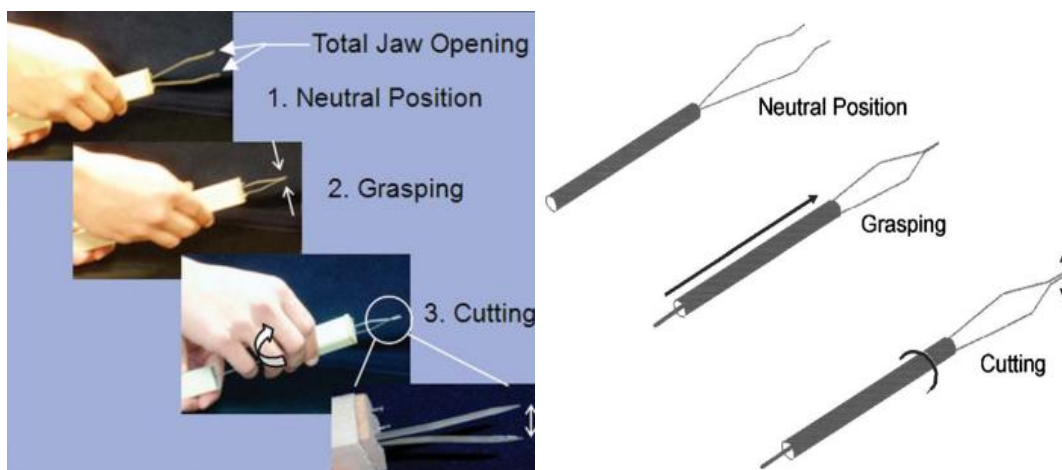


Figure 1.14. Multifunctional compliant scissors-forceps design [37][38].

More research on multifunctional instruments can be found in literature [40-42] and patent filings [43-45]. There are also some other combinations through parallel channels, utilizing different types of tools at the same time, thus making it multifunctional. However, here in this thesis the design of one single set of working jaws as the end-effector which is able to provide multiple functions will be focused.

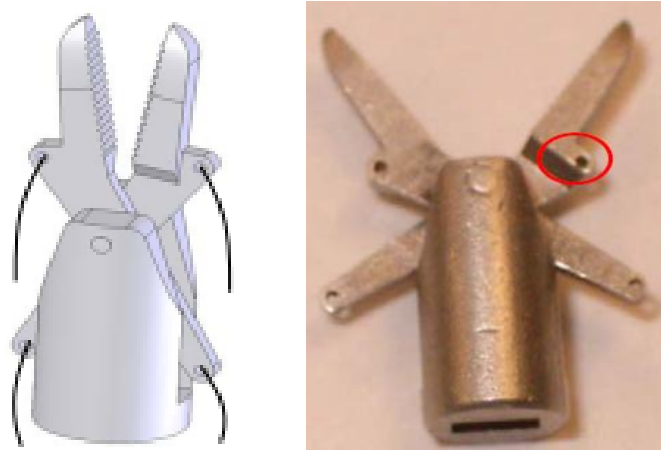


Figure 1.15. The design incorporating two sets of actuating wires [39].

1.3 Motivation and Objectives

With the advances in Minimally Invasive Surgery, it is desired that surgical instruments with smaller shaft size, and thus smaller end-effector to be developed such that the MIS techniques can be less invasive. As previously mentioned, conventional end-effectors with rigid links and hinges will be difficult to miniaturize furthermore, since the manufacturing process will get complex, the cost will increase, and the assembly will be very difficult as well. In addition, sterilization of the tools,

wear and backlash could be other problems. Consequently, a compliant parallel robotic mechanism is necessary to be developed to overcome these drawbacks. In addition, due to the constrained operation space of MIS, it is preferable that this instrument has more degrees of freedom so that it is dexterous enough to perform different operations. Thus, another objective of this research is to integrate the rotational platform to the system, providing the end-effector with 360-degree rotational degree of freedom, in addition that the parallel mechanism provides three degrees of freedom already.

With multifunctional instruments, surgeons do not have to switch between the tools so frequently and thus the surgery time can be further reduced. Therefore, developing multifunctional forceps combining useful functions of different types of surgical instruments is another goal of this thesis. The forceps are able to cut and grasp tissues without interfering with each other. The electrical Cautery ability to arrest bleeding and cut tissues is also integrated in the design.

1.4 Outline

Chapter 2 proposes two sets of system schemes of the compliant parallel robotic surgical instrument with CAD models being shown, and then these two sets of schemes are discussed and compared in terms of advantages and disadvantages. Afterwards one of the schemes is chosen. What follows is the geometric description of the compliant parallel robotic surgical instrument. The kinematic analysis

composed of mobility analysis, inverse kinematics and workspace evaluation is presented in details. Jacobian and stiffness matrices of the parallel mechanism are derived and discussed at the end of this chapter, which give a better understanding of the parallel mechanism.

Chapter 3 presents stiffness modeling including the stiffness modeling of one linear limb with parallel mechanism and the stiffness modeling of the compliant parallel robot comprising three identical limbs. It is followed by the stiffness analysis with respect to different parameters. The stiffness was evaluated in MATLAB, and the trends of stiffness with respect to different parameters was revealed.

Chapter 4 focuses on the optimization of the compliant parallel robotic platform. First, single variable optimizations with respect to workspace and stiffness are performed using Genetic Algorithm in MATLAB. Then workspace and stiffness are combined to form one single objective function and such a multi variable optimization problem is solved using the same method. Results and discussion are presented at the end.

Chapter 5 deals with the design of the multifunctional forceps with the abilities of scissor-cutting, grasping and electrical Cautery. Finite element modeling of the multifunctional forceps is conducted in SolidWorks, and then it is optimized by trial and modification until the requirements are met and the design is finalized.

Chapter 6 gives the conclusions and specifies the contributions of the thesis. Besides, some recommendations are suggested for future work to improve the surgical instruments for MIS to have better performance.

Chapter 2 Design and Analysis of the Compliant Parallel Robotic Surgical Instrument

2.1 Introduction

In this chapter, two design schemes will be proposed. The advantages and disadvantages will be discussed and then it is decided that the one with better mechanical properties will be chosen as the surgical instrument for MIS.

The two schemes proposed in this study both have the feature of compliant parallel mechanism. The compliant parallel mechanisms were adopted mainly due to the advantages of compliant mechanisms over the traditional rigid mechanisms which was illustrated in the previous chapter and the advantages of the parallel mechanisms over its serial counterpart, including higher stiffness, higher payload capacity, and lower inertia to the manipulator. Typically, a parallel robot is composed of a fixed base which is connected to the moving platform by several limbs. Each limb is controlled by one actuator and all the actuators can be placed at the fixed base. Since the external load applied on the moving platform can be shared by actuators, parallel mechanisms tend to have a large payload capacity.

Geometric formation of the compliant parallel mechanism will be described. Geometric description discloses how this compliant parallel mechanism is formed and

via calculation, the relationship between the output movements and the input angles can be found. As of inverse kinematics, it reveals a reachable position and orientation of the moving platform

Jacobian matrix will be derived afterwards. The Jacobian matrix has significant meaning for parallel robot. It is not only the fundamental part to calculate many other performance indices, such as stiffness, dexterity and manipulability, it is also important to implement the static analysis, such as the singularity analysis.

2.2 Proposed Design Scheme 1 of the Surgical Instrument

2.2.1 Conceptual Design

In this scheme, a surgical instrument features a two Degrees of Freedom bending manipulator with a compliant grasper is presented. The bending mechanism consists of four flat compliant links with Lamina Emergent Joints (LEJs). Each compliant link connects the rigid links and the end-effector with passive joints. These four flat compliant links are located around the sheath, allowing an inner space for other devices going through inside. This manipulator bends when the pair of compliant links facing to each other are driven to bend by the differential motions of the rigid links which are connected to them through passive joints. When one pair of the compliant links is bending, it affects the other pair of compliant links. That is what the

passive joints are introduced here for. The effects can be compensated by the passive joints [20], as the other pair of compliant joints can rotate around the joints when that pair of compliant links are bending.

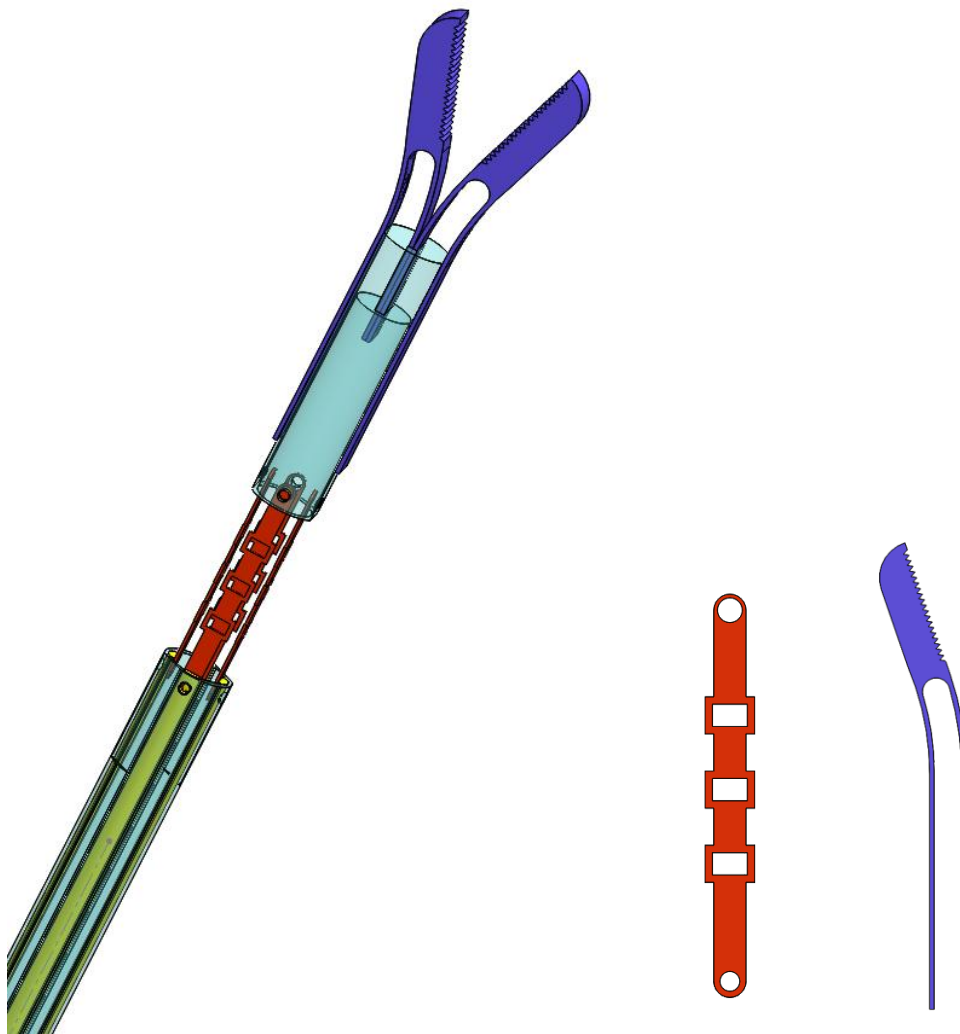


Figure 2.1. Scheme 1 bending manipulator with compliant grasper jaws.

The compliant grasper jaws can be designed as shown in Figure 2.1. Two jaws are assembled in pair inside the end effector. Since the jaws are compliant, then they can be closed by pulling the wire connected to the inside end of the jaws, making them to deflect towards each other.

2.2.2 Simulation of Deflection of the Bending Mechanism

In the simulation, the model was simplified equivalently by replacing the end effector with just a rigid link and without caring about the shape of the rigid link connected with the compliant link and sheath. After the simulation, the deflection result is shown below in Figure 2.2, in which it shows that the bending displacement is on the order of micro meters, which is too small for the surgical application. Even when the driving forces are increased and the shape of the flat compliant links are changed to make them more compliant, the deflections are still not large enough. This is mainly due to the effects imposed by the other pair of compliant links when one pair of compliant links are driven to bend. The passive joints used here to compensate the effects are not enough. Another way to further compensate the effects is to change the geometries of the compliant links to make them even more compliant. However, since the compliant grasper jaws are driven by pulling the wire in order to close up the jaws and the pulling force will also be exerting on the compliant links. If they are not stiff enough to withstand the force, the compliant links will bend randomly in all directions which is unwanted in the application. Therefore, although this kind of mechanism is compact and in simple structure, its mechanical performance does not meet the requirements of this application. Finally, it is decided that this mechanism is abandoned and another type of mechanism will be proposed and analyzed in more details.

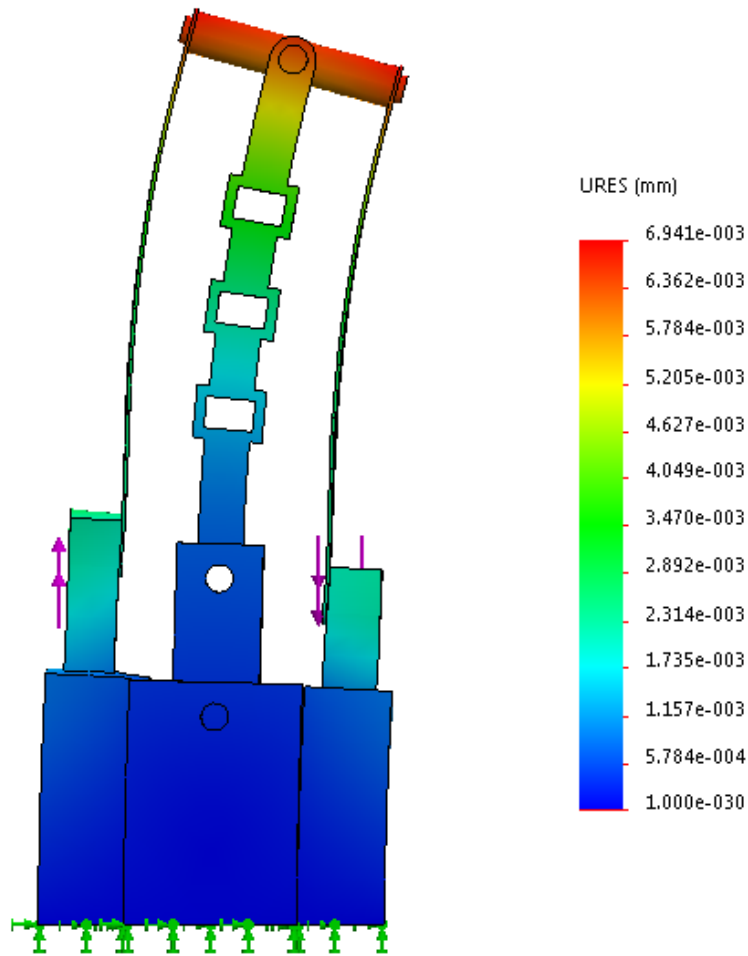


Figure 2.2. Simulation of the deflection of the proposed mechanism driven by a pair of differential forces in opposite directions.

2.3 Proposed Design Scheme 2 of the Surgical Instrument

In this section the conceptual design of a compliant parallel robotic surgical instrument with multifunctional forceps for Minimally invasive Surgery is presented. In addition, the pros and cons will be discussed and the reasons for choosing it for the application will be explained.

2.3.1 Compliant Parallel Robot Geometric Structure

Figure 2.3 shows the 3D model of the conceptual design of the compliant parallel robotic surgical instrument with multifunctional forceps for MIS. This instrument consists of five parts, including the shaft, the rotational platform, the compliant parallel mechanism, the upper base and the multifunctional forceps. The shaft is connected to the handler with which surgeons can hold and use to control the other parts of the instrument. In addition, the shaft is hollow, leaving the space for the wires connected to the actuators. The rotational platform provides the rotational degree of freedom to the manipulator. This can be realized by integrating a piezoelectric motor. This piezoelectric motor should have enough torque to rotate the manipulator and enough holding torque to prevent itself from damaging when it is held from rotating.

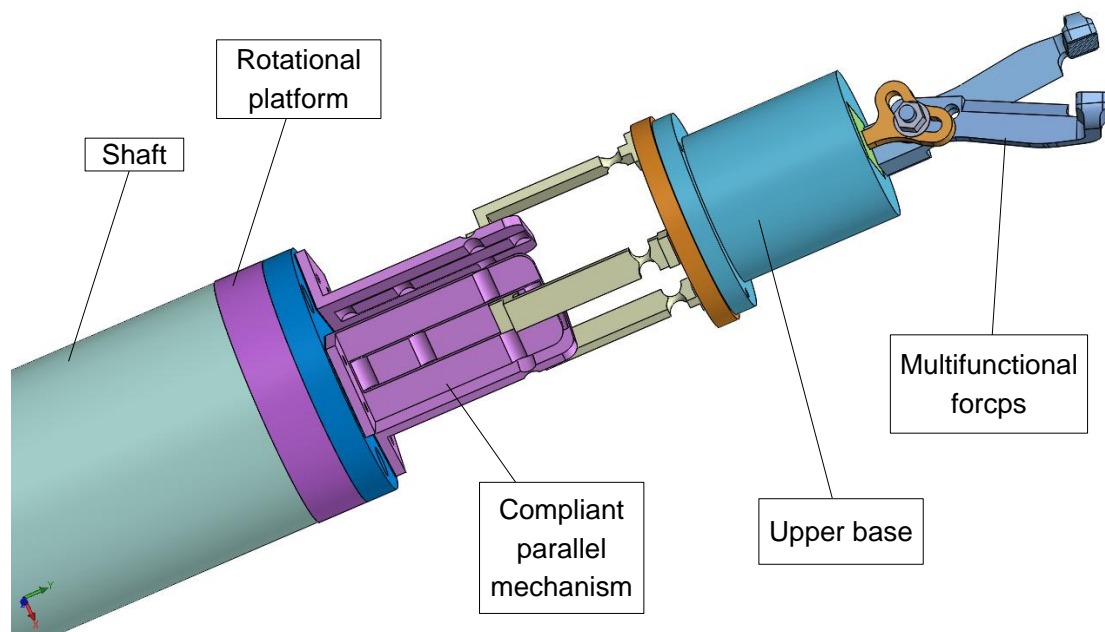


Figure 2.3. A 3D model of the conceptual design of the compliant parallel robotic surgical instrument with multifunctional forceps for MIS.

Figure 2.4 shows that the compliant parallel mechanism is composed of a base which is attached to the rotational platform, a moving platform, and LEMs with flexure hinges. These LEMs connect the base with the moving platform to form a compliant parallel mechanism. Essentially, the LEM is a 4-bar mechanism, as shown in Figure 1.10, through the connections of circular flexure hinges. The circular flexure hinges can provide large displacements when bent and thus generates the out-of-plane movements from the LEM manufactured plane, as shown in Figure 2.6. From the simulation result, it can be noted that the displacement is quite large enough for the application in MIS.

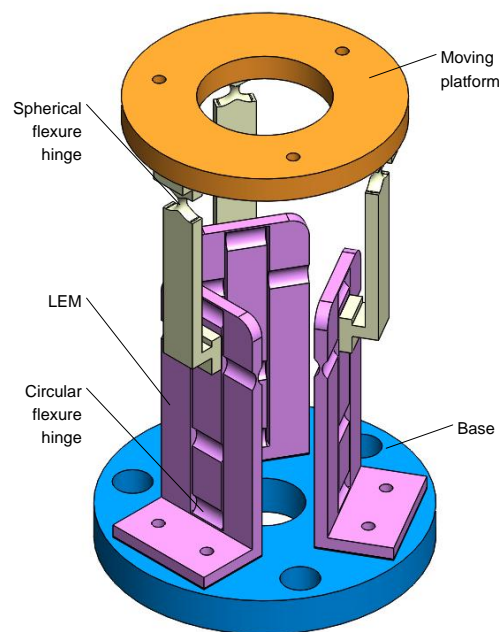


Figure 2.4. A 3D model of the compliant parallel mechanism.

Figure 2.5 shows the upper base with a multifunctional forceps mounted on it. The linear piezoelectric motor actuating the forceps to open and close can be mounted inside the upper base.

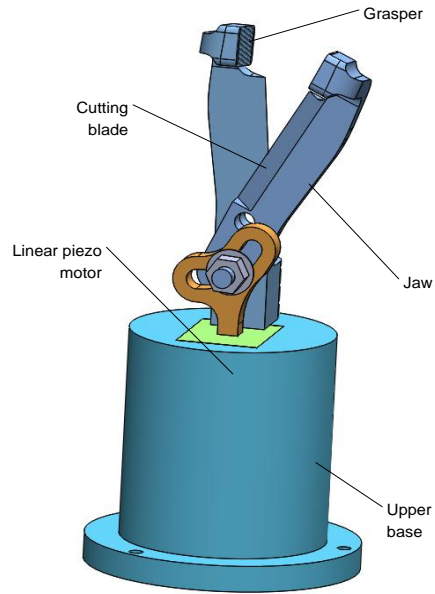


Figure 2.5. A 3D model of the multifunctional forceps attached to its base.

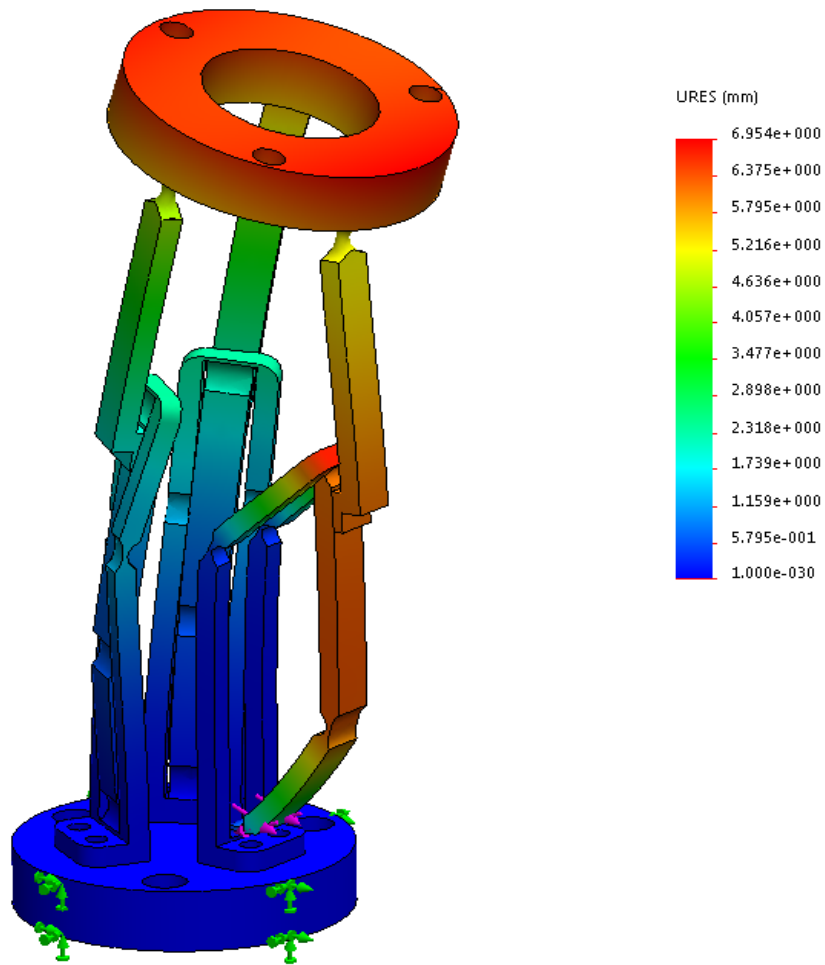


Figure 2.6. Simulation result of displacement of the compliant parallel mechanism.

Compared with the first proposed scheme, the second scheme has more degrees of freedom since the rotational platform and the multiple degree-of-freedom compliant parallel mechanism are integrated into the system. As the LEMs are adopted in this design, it is able to design the mechanism really compact while still possess large movement outside of the initial plane. The forceps that is able to conduct at least two functions with one set of tool is another feature of this design. With this multifunctional forceps, surgeons will be able to perform surgery more effectively.

However, there are some challenges this design may face. One of them is the limitations of the actuators in the existing market. Since this surgical instrument is dedicated to Minimally Invasive Surgery, the instrument must be designed within 10 millimeters so that it can be inserted through the incisions to perform operations inside the human body. With this design, the actuators have to be installed at the points where need to be actuated, requesting the actuators be very miniature yet still powerful enough to actuate. Even though there are some miniature piezoelectric motor in the market, the ability to install them on site to control the compliant parallel mechanism remains susceptible. Nonetheless, these limitations will be resolved in the near future with the fast development of mini scale piezoelectric motors.

Next, the kinematics of the compliant parallel mechanism will be examined to understand the how it works and other performance indices, such as workspace and stiffness will also be analyzed in later chapters.

2.4 Kinematics Analysis

2.4.1 Mobility Analysis

Mobility or the degree of freedom (DOF) of a mechanism refers to the number of independent variables or inputs needed to specify the configuration of the mechanism completely [46]. The degree of freedom F of a mechanism can be calculated from the Chebychev-Grübler-Kutzbach formula.

$$F = \lambda(n - j - 1) + \sum_{i=1}^j f_i, \quad (2.1)$$

where F is the degree of freedom of the mechanism; λ is the degree of freedom of each unconstrained individual body, $\lambda = 3$ for planar and spherical mechanisms and $\lambda = 6$ for spatial mechanisms; n is the number of links in a mechanism including the fixed base and moving platform; j is the number of joints; and f_i is the number of degrees of freedom permitted by joint i .

The parallel mechanism consists of one fixed base, one moving platform, and three identical limbs. Each limb is composed of one 4-bar LEM link and another link with a spherical compliant hinges connected the moving platform with the 4-bar LEM link. The 4-bar LEM link provides one rotational degree of freedom, so it can be seen as one revolute joint. Between the 4-bar LEM link and the base, there is a revolute joint connecting these two parts. As we know, the revolute joint allows 1 degree of

freedom and the spherical joint allows 3 degrees of freedom. Each of the three limbs consists of 2 links. Combining the base and the platform, there are 8 links altogether. Since each limb has 2 revolute joints and 1 spherical joint, the mechanism has 9 joints in total. Therefore, the degree of freedom of this compliant parallel platform can be calculated by:

$$F = \lambda(n - j - 1) + \sum_{i=1}^j f_i = 6(8 - 9 - 1) + 3(1 + 1 + 3) = 3. \quad (2.2)$$

2.4.2 Inverse Kinematics

In order to analyze the kinematics of the compliant parallel mechanism mathematically, the pseudo-rigid-body model (PRBM) theory was adopted. PRBM is a simple method which is used to model the deflection of flexible members with rigid-body components that have equivalent force-deflection characteristics [47], so that the rigid-body theory can then be used to analyze the compliant mechanism. With this method, one can easily analyze compliant systems that undergo large, nonlinear deflections.

As shown in Figure 2.7, a kinematically equivalent graph of the proposed compliant parallel mechanism is presented. There are three identical limbs with one end connecting to the fixed base and the other end to the moving platform. The lower ends of the limbs, also the vertices of the equilateral inner triangle with the length t , of the base circle, points B_1 , B_2 , B_3 , are connected to the fixed base through circular

flexure hinges. The upper end of the limbs, also the vertices of the equilateral inner triangle with the length r_p of the platform circle, points P_1, P_2, P_3 , are connected to the moving platform through spherical flexure hinges. The reference coordinate frame $O\{x, y, z\}$ is attached to the base with the origin O located at the centroid of the triangle $B_1B_2B_3$. The x axis is in the direction along OB_2 pointing to point B_2 , while the y axis is perpendicular to the side B_1B_2 . Both x and y axes are lying on the same plane as the triangle $B_1B_2B_3$ plane. The z axis is perpendicular to the x - y plane and pointing to the moving platform. The coordinate frame $G\{u, v, w\}$ is attached to the moving platform with the origin G located at the centroid of the triangle $P_1P_2P_3$. The u axis is in the direction along GP_2 pointing to point P_2 , while the v axis is perpendicular to the side P_1P_2 . Both u and v axes are lying on the same plane as the triangle plane $P_1P_2P_3$. The w axis is perpendicular to the u - v plane and pointing upwards. The radius of the fixed base circle is r_b and the radius of the moving platform circle is r_p .

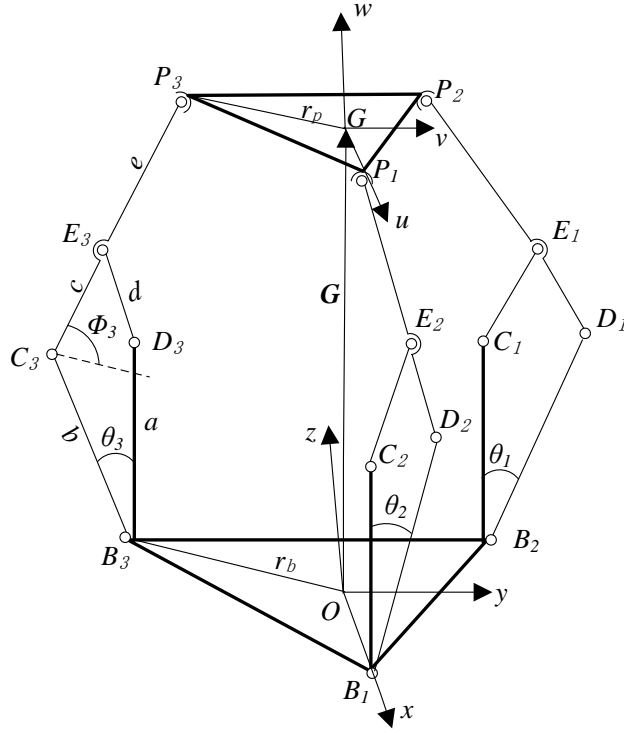


Figure 2.7. Kinematically equivalent diagram of the compliant parallel mechanism

The inverse kinematics deals with a problem which can be stated as follow: given a the position of a point $G(G_x, G_y, G_z)$ and its orientation, the orientation of the platform $(\theta_x, \theta_y, \theta_z)$, in the fixed base reference frame, the problem is to find the input angles θ_1, θ_2 , and θ_3 .

The homogeneous transformation matrix T from the moving platform frame to the fixed base reference frame is given by:

$$T = \begin{bmatrix} \mathbf{R}_G^0 & \mathbf{Q} \\ \mathbf{0}_{1 \times 3} & 1 \end{bmatrix} = \begin{bmatrix} u_x & v_x & w_x & G_x \\ u_y & v_y & w_y & G_y \\ u_z & v_z & w_z & G_z \\ 0 & 0 & 0 & 1 \end{bmatrix}, \quad (2.3)$$

where $\mathbf{Q}(G_x, G_y, G_z)$ is the position vector of the center of the base O pointing to the center of the platform G , and \mathbf{R}_G^0 is the rotation matrix of the moving platform.

Coordinate of point P_i that is embedded in frame $G\{u, v, w\}$ with respect to the base reference frame can be expressed as:

$$\mathbf{P}_{i,0} = \begin{bmatrix} P_{i,x} \\ P_{i,y} \\ P_{i,z} \\ 1 \end{bmatrix} = \mathbf{T}\mathbf{P}_{i,G} = \begin{bmatrix} c\theta_x c\theta_y & c\theta_x s\theta_y s\theta_z - s\theta_x c\theta_z & c\theta_x s\theta_y c\theta_z + s\theta_x s\theta_z & G_x \\ s\theta_x s\theta_y & s\theta_x s\theta_y s\theta_z + c\theta_x c\theta_z & s\theta_x s\theta_y c\theta_z - c\theta_x s\theta_z & G_y \\ -s\theta_y & c\theta_x s\theta_z & c\theta_y c\theta_z & G_z \\ 0 & 0 & 0 & 1 \end{bmatrix} \begin{bmatrix} r_p c\alpha_i \\ r_p s\alpha_i \\ 0 \\ 1 \end{bmatrix}, \quad (2.4)$$

where $c\theta_x$ represents $\cos\theta_x$, $s\theta_x$ representing $\sin\theta_x$. θ_x , θ_y , and θ_z are the roll, pitch and yaw angles of the moving platform; r_p is the length of GP_i as shown in the Figure. The angles α_i ($i = 1, 2, 3$) are the angles between GP_i and the axis Gu as shown in the Figure. Therefore, we have

$$\begin{bmatrix} \alpha_1 \\ \alpha_2 \\ \alpha_3 \end{bmatrix} = \begin{bmatrix} 0 \\ 2\pi/3 \\ 4\pi/3 \end{bmatrix}. \quad (2.5)$$

The vector-loop equation for limb 3 is written as:

$$\overrightarrow{OP_3} = \overrightarrow{OB_3} + \overrightarrow{B_3C_3} + \overrightarrow{C_3P_3}. \quad (2.6)$$

Rewriting Equation (2.6) for each components x , y , and z separately gives

$$P_{3,x} = r_b c\alpha_3 + bs\theta_3 c\alpha_3 + (c + e)c\phi_3 c\alpha_3, \quad (2.7)$$

$$P_{3,y} = r_b s\alpha_3 + bs\theta_3 s\alpha_3 + (c + e)c\phi_3 s\alpha_3, \quad (2.8)$$

$$P_{3,z} = 0 + bc\theta_3 + (c + e)s\phi_3, \quad (2.9)$$

where r_b is the length of Ob_i , c and e the lengths of links C_3E_3 and E_3P_3 respectively as shown in Figure 2.7.

In order to obtain the relationship between the desired pose (position and

orientation) of the platform and the input angles, it is necessary to eliminate the extra variable ϕ . So we rewrite Equations (2.7) through (2.9) as follows:

$$c\phi_3 = \frac{P_{3,x} - r_b c\alpha_3 - bs\theta_3 c\alpha_3}{(c + e)c\alpha_3}, \quad (2.10)$$

$$c\phi_3 = \frac{P_{3,y} - r_b s\alpha_3 - bs\theta_3 s\alpha_3}{(c + e)s\alpha_3}, \quad (2.11)$$

$$s\phi_3 = \frac{P_{3,z} - bc\theta_3}{c + e}. \quad (2.12)$$

Multiplying Equation (2.10) by (2.11), and adding it to the square of Equations (2.12) gives

$$\begin{aligned} & (c + e)^2 c\alpha_3 s\alpha_3 \\ &= (P_{3,x} - r_b c\alpha_3 - bc\alpha_3 s\theta_3)(P_{3,y} - r_b s\alpha_3 - bc\alpha_3 s\theta_3) \\ &+ (P_{3,z} - bc\theta_3)^2 c\alpha_3 s\alpha_3. \end{aligned} \quad (2.13)$$

Similarly, two other equations can be derived for limb 1 and limb 2 as follows:

$$\begin{aligned} & (c + e)^2 c\alpha_1 s\alpha_1 \\ &= (P_{1,x} - r_b c\alpha_1 - bc\alpha_1 s\theta_1)(P_{1,y} - r_b s\alpha_1 - bc\alpha_1 s\theta_1) \\ &+ (P_{1,z} - bc\theta_1)^2 c\alpha_1 s\alpha_1, \end{aligned} \quad (2.14)$$

$$\begin{aligned} & (c + e)^2 c\alpha_2 s\alpha_2 \\ &= (P_{2,x} - r_b c\alpha_2 - bc\alpha_2 s\theta_2)(P_{2,y} - r_b s\alpha_2 - bc\alpha_2 s\theta_2) \\ &+ (P_{2,z} - bc\theta_2)^2 c\alpha_2 s\alpha_2. \end{aligned} \quad (2.15)$$

To solve the input angles θ_i with respect to the known output position (G_x, G_y, G_z) ,

Equation (2.13) can expand and rearrange in the following form:

$$e_1 s\theta_3 + e_2 c\theta_3 + e_3 = 0, \quad (2.16)$$

where

$$e_1 = 2br_b c\alpha_3 s\alpha_3 - P_{3,x} b s\alpha_3 - P_{3,y} b c\alpha_3 ,$$

$$e_2 = -2P_{3,z} b c\alpha_3 s\alpha_3 ,$$

$$e_3 = (P_{3,z}^2 + r_b^2 + b^2) c\alpha_3 s\alpha_3 + P_{3,x} P_{3,y} - P_{3,x} r_b s\alpha_3 - P_{3,y} r_b c\alpha_3 .$$

To solve Equation (2.16) , the trigonometric identities is used.

Let

$$s\theta_i = \frac{2t_i}{1 + t_i^2} ,$$

$$c\theta_i = \frac{1 - t_i^2}{1 + t_i^2} ,$$

where

$$t_i = \tan \frac{\theta_i}{2} .$$

Substituting the trigonometric identities above into Equation (2.16) yields

$$(e_3 - e_2)t_3^2 + 2e_1 t_3 + (e_3 + e_2) = 0 .$$

Solving Equation (2.16) for t_3 gives

$$\theta_3 = 2 \tan^{-1} \frac{-e_1 \pm \sqrt{e_1^2 + e_2^2 - e_3^2}}{e_3 - e_2} .$$

It can be found from Equation (2.18) that there are normally two solutions of each input angle θ_i regarding a given position of the moving platform, and hence there are two configuration of each limb and in total six configuration of the mechanism. When Equation (2.16) yields no real roots, it means the given particular position of the moving platform is not reachable. Similarly, the configurations of the other two limbs can be obtained by following the same procedures. Since there are multiple configurations corresponding to one specified location of the moving platform, it is

required that one specific solution should be chosen considering the working conditions, control strategies and other constraints on this parallel robotic mechanism.

For example, a position ($G_x = 3, G_y = 3, G_z = 9$) and orientation ($\theta_x = 0.2, \theta_y = 0.02, \theta_z = 0.2$.) of the center of the platform are given, the input angles are to be found. After calculation via the relationship equations above, the input angles are obtained as shown in Table 2.1. The dimensional parameters of the mechanism are displayed in Table 2.2.

Table 2.1. Input angles (unit radian) at a specifically given position for example.

Angle	Solution 1	Solution 2
θ_1	3.0911	0.0505
θ_2	-0.4788	0.0757
θ_3	-0.5534	-1.0195

Table 2.2. Parameters of the mechanism for preliminary design.

parameters of the links	l_a	l_b	l_c	l_d	l_e
unit (mm)	15	12	8	5	10
parameters of base and platform	r_b	r_p			
unit (mm)	12	10			

2.4.3 Workspace Evaluation

Workspace of a parallel manipulator refers to the region consisted of all the reachable points by the origin of a coordinate system attached to the center of the end-effector [48]. Workspace is an important index to evaluate the performance of a parallel robot, since with the larger workspace, the wider area the manipulator can cover. In this application of Minimally Invasive Surgery, it is meaningful that even though the surgical instrument is designed compact, it is still possible for surgeons to reach as wide an area as possible during the procedures without compromising other aspects. So workspace has to be found out, such that further work can be done to optimize it in order to get better performance, a larger workspace in this scenario.

Speaking of evaluating workspace of parallel manipulator, the kinematics analysis has to be done. From the aforementioned kinematics analysis, the workspace varies as some other parameters vary, such as the lengths of the links, the radii of the base circle and the moving platform circle, and the input angles. With these parameters as variables accounted for the calculation, all reachable points can be obtained. In order to visualize the workspace which consists of all the reachable points, an algorithm presented in [49] was adopted and programmed in MATLAB to evaluate the volume and to graphically display the landscape of the workspace.

In Figure 2.8 and 2.9, they show the workspace from different views with the volume equal to 209.35171 mm^3 . In this case of the evaluation, the preliminary

parameters are given as the length of link b $l_b = 13$ mm, the radius of the base circle $r_b = 13$ mm, the radius of the platform circle $r_p = 12$ mm and all three input angles ($\theta_1, \theta_2, \theta_3$) from 0 to $\pi/6$.

With the values of the design parameters varying, it can be seen from the results of workspace and volume shown in Figure 2.10 through 2.15 that the workspace and volumes are changing, but changing without any linear relation to these parameters. Therefore, these design parameters need to be optimized within constraints to get largest workspace and largest volume in order to obtain the most performance of the parallel manipulator. The optimization will be explained in details in Chapter 5.

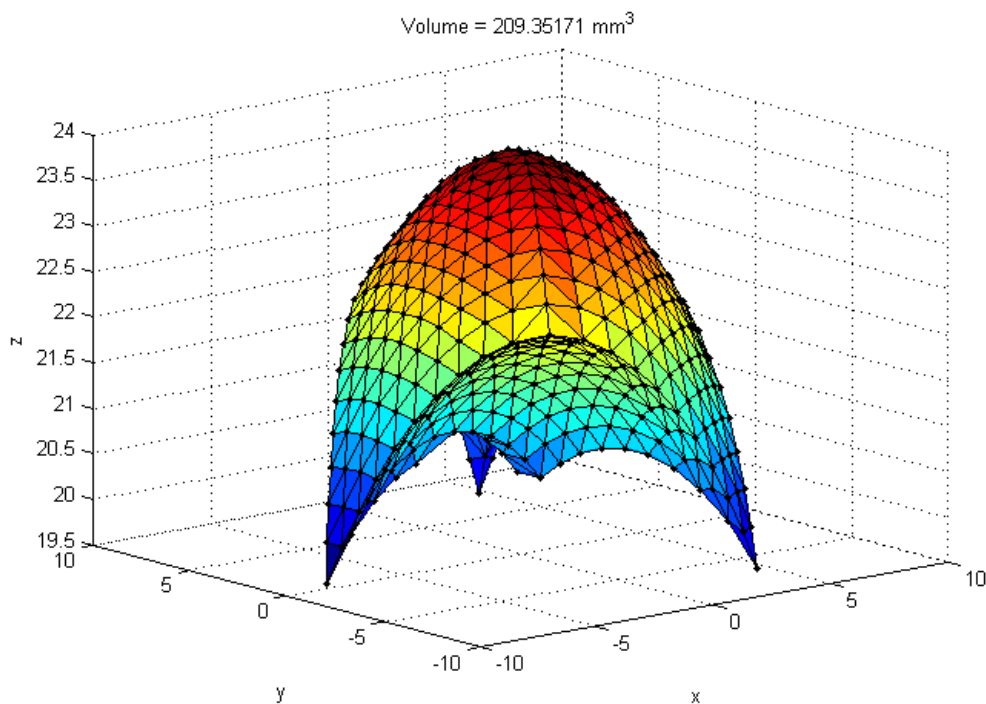


Figure 2.8. Workspace and volume (Top trimetric view),
with $l_b = 13$ mm, $r_b = 13$ mm, $r_p = 12$ mm.

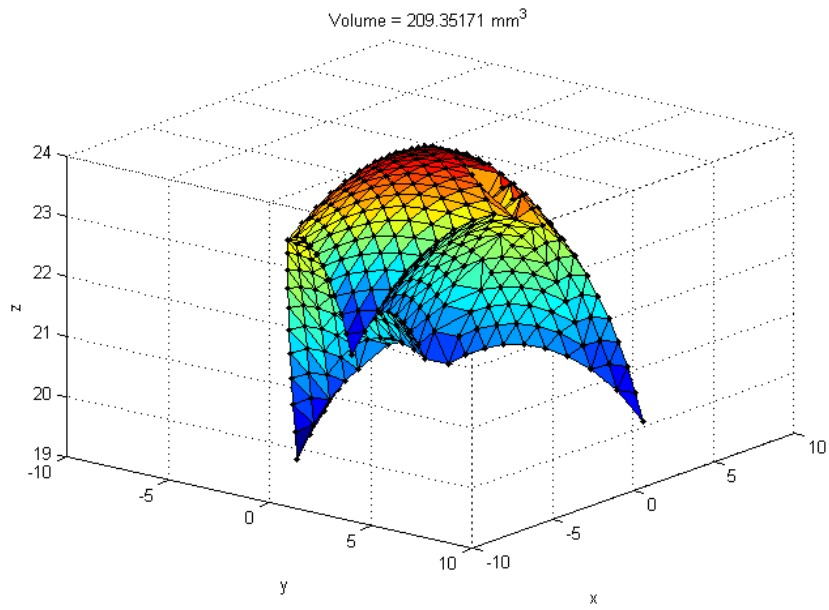


Figure 2.9. Workspace and volume (Bottom trimetric view),
with $l_b = 13$ mm, $r_b = 13$ mm, $r_p = 12$ mm.

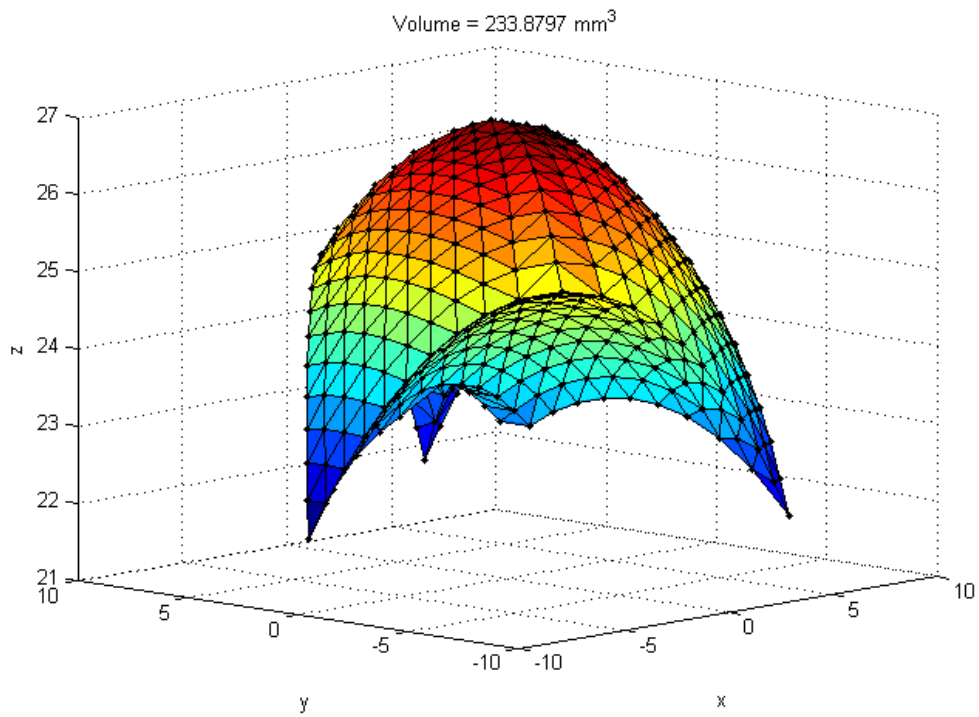


Figure 2.10. Workspace and volume (Top trimetric view),
with $l_b = 13.5$ mm, $r_b = 13$ mm, $r_p = 12$ mm.

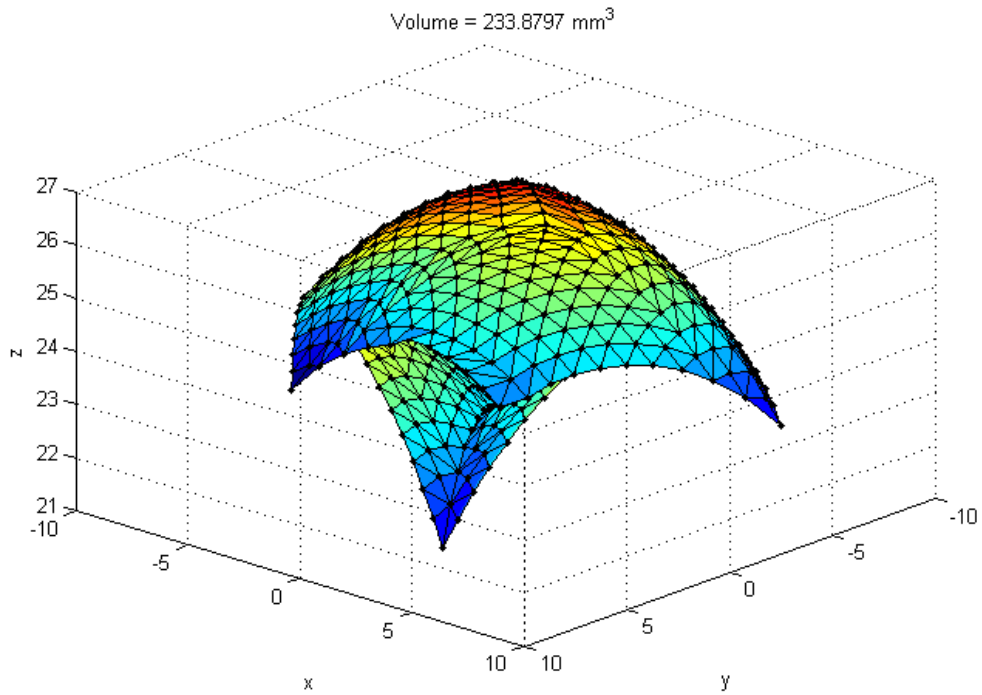


Figure 2.11. Workspace and volume (Bottom trimetric view),
with $l_b = 13.5$ mm, $r_b = 13$ mm, $r_p = 12$ mm.

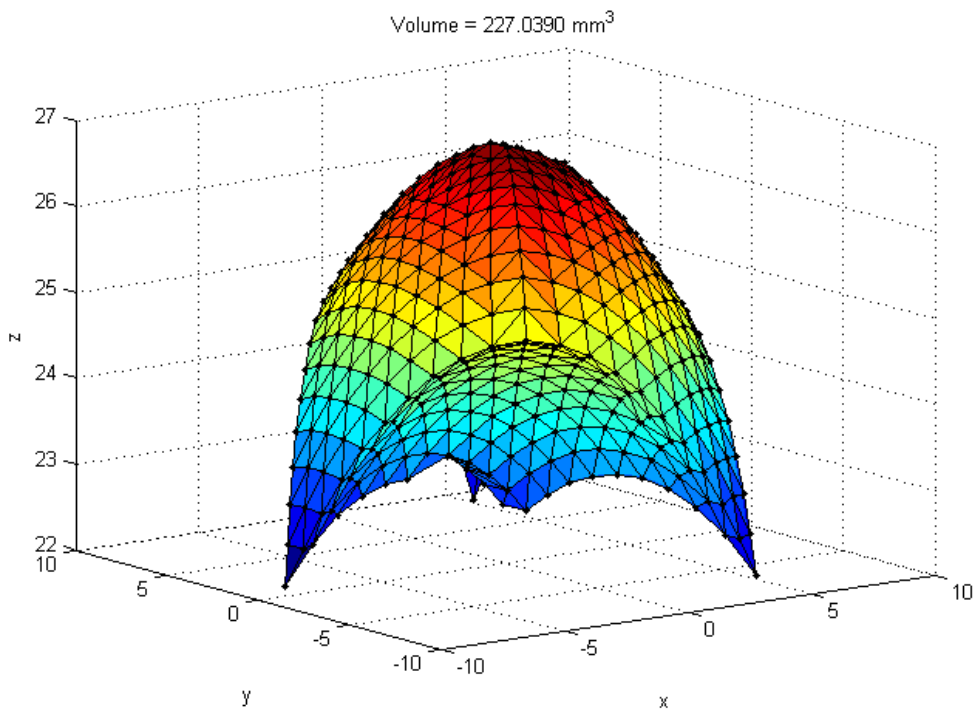


Figure 2.12. Workspace and volume (Top trimetric view),
with $l_b = 13.5$ mm, $r_b = 13.5$ mm, $r_p = 12$ mm.

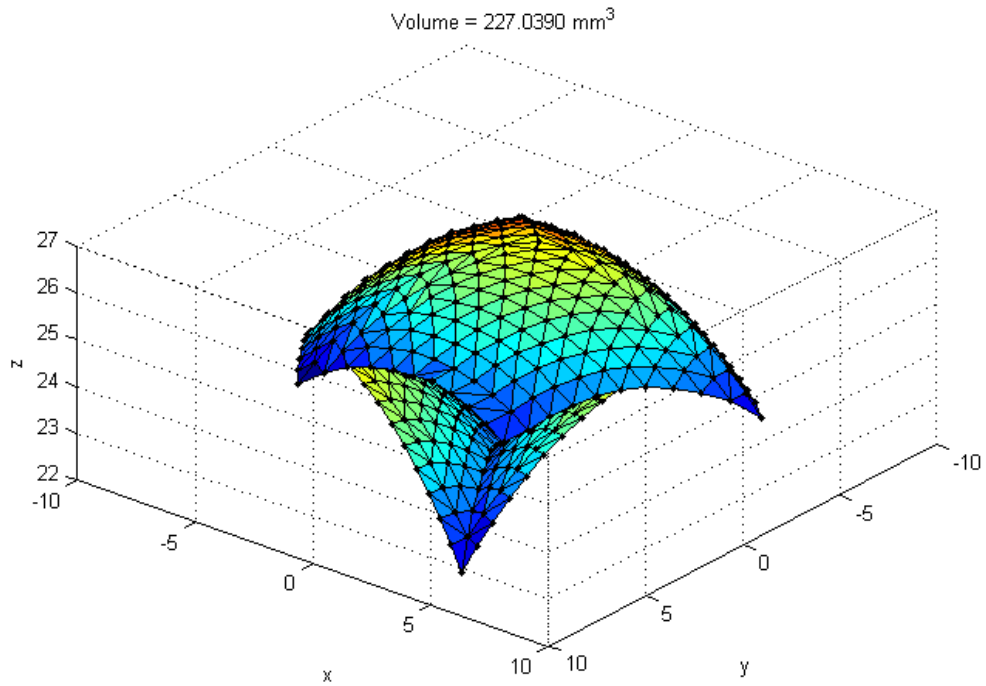


Figure 2.13. Workspace and volume (Bottom trimetric view),
with $l_b = 13.5$ mm, $r_b = 13.5$ mm, $r_p = 12$ mm.

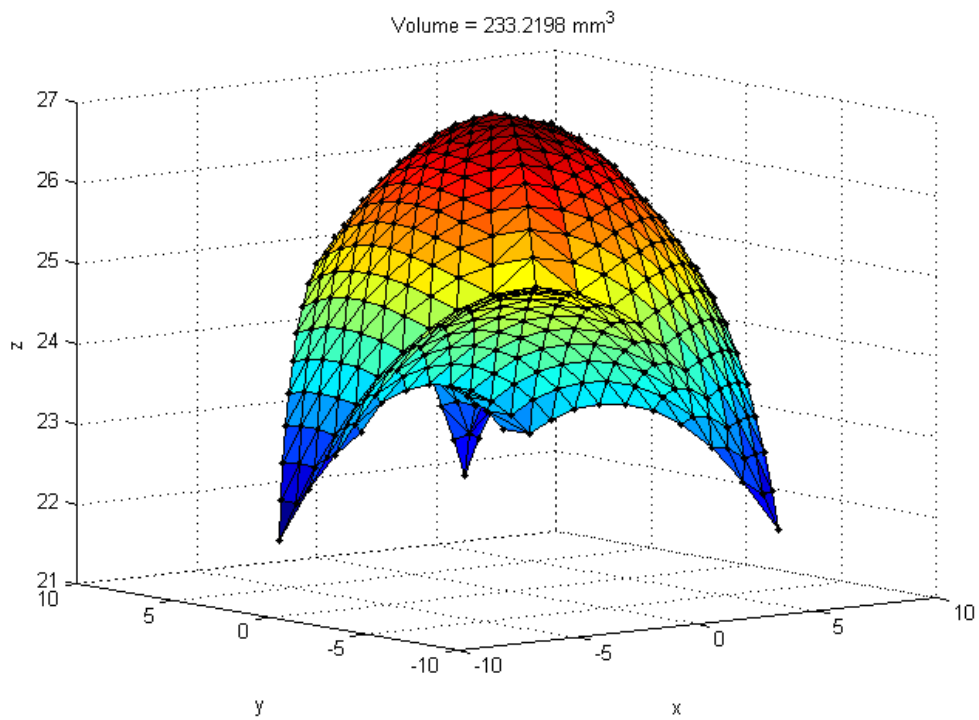


Figure 2.14. Workspace and volume (Top trimetric view),
with $l_b = 13.5$ mm, $r_b = 13.5$ mm, $r_p = 12.5$ mm.

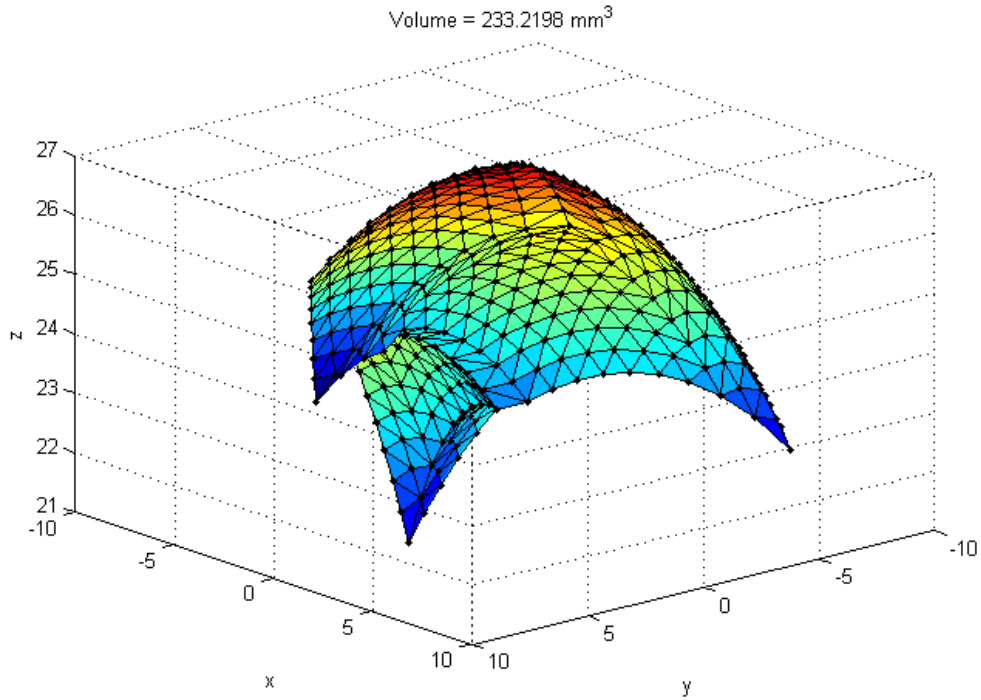


Figure 2.15. Workspace and volume (Bottom trimetric view),
with $l_b = 13.5$ mm, $r_b = 13.5$ mm, $r_p = 12.5$ mm.

2.5 Jacobian Matrix

Jacobian matrix maps the relation between the speed at actuator and the speed at the moving platform. The Jacobian matrix of the parallel robot refers to the matrix represents the transformation from Cartesian velocities into the joint rates in the platform [46].

Since the Jacobian matrix is significant to the analysis of performance of parallel mechanisms, many researchers have done a lot of work and many theories have been proposed related to this topic. Here the method of velocity vector-loop equations is adopted to derive the Jacobian matrix of the parallel robot. Once the Jacobian matrix

is obtained, the singularity conditions of the manipulator can be analyzed and later the dexterity of the parallel robot can be derived as well.

Generally, in parallel manipulator we have a vector \mathbf{x} to denote the location of the moving platform and a vector \mathbf{q} to describe the actuated joint variables. Then the kinematic constraints imposed by the limbs can be written as

$$\mathbf{f}(\mathbf{x}, \mathbf{q}) = \mathbf{0} \quad , \quad (2.19)$$

where \mathbf{f} is an n-dimensional implicit function of \mathbf{x} and \mathbf{q} and $\mathbf{0}$ is an n-dimensional zero vector. The relationship between the output velocity $\dot{\mathbf{x}}$ of the platform and the input joint rates $\dot{\mathbf{q}}$ can be found by differentiating Equation (2.19) with respect to time as:

$$J_x \dot{\mathbf{x}} = J_q \dot{\mathbf{q}} \quad , \quad (2.20)$$

where

$$J_x = \frac{\partial \mathbf{f}}{\partial \mathbf{x}} \quad , \text{ and}$$

$$J_q = - \frac{\partial \mathbf{f}}{\partial \mathbf{q}} \quad .$$

Two different Jacobian matrices, J_x and J_q are obtained through the derivation above. So the overall Jacobian matrix J can be expressed as

$$\dot{\mathbf{q}} = J \dot{\mathbf{x}} \quad , \quad (2.21)$$

where $J = J_q^{-1} J_x$.

Referring to Figure 2.7, the loop-closure equation can be written for each limb as:

$$\overrightarrow{OG} = \overrightarrow{OB_i} + \overrightarrow{B_iC_i} + \overrightarrow{C_iP_i} + \overrightarrow{P_iG} , \quad (2.22)$$

Differentiating Equation (2.22) with respect to time gives the vector-loop equation,

$$\mathbf{v}_g = 0 + \dot{\theta}_i (\mathbf{k} \times \mathbf{b}_i) + \dot{\phi}_i (\mathbf{k} \times \mathbf{f}_i) + 0 , \quad (2.23)$$

where \mathbf{v}_g is the velocity of point G and \mathbf{k} is a unit vector pointing in the positive z -axis direction, \mathbf{b}_i and \mathbf{f}_i ($f = c + e$) are the vectors along the link B_3C_3 and C_3P_3 respectively. Since $\dot{\phi}_i$ is a passive variable, it should be eliminated from Equation (2.23). To achieve this goal, we dot-multiply both sides of Equation (34) by \mathbf{f}_i , which leads to

$$\mathbf{f}_i \cdot \mathbf{v}_g = \dot{\theta}_i \mathbf{f}_i \cdot (\mathbf{k} \times \mathbf{b}_i) . \quad (2.24)$$

Equation (2.24) can be rewritten as

$$\mathbf{f}_i \cdot \mathbf{v}_g = \dot{\theta}_i \mathbf{k} \cdot (\mathbf{b}_i \times \mathbf{f}_i) . \quad (2.25)$$

Writing Equation (2.25) three times, once for each limb $i = 1, 2,$ and 3 , three scalar equations are obtained. They can be rearranged in matrix form as below:

$$J_x \dot{\mathbf{x}} = J_q \dot{\mathbf{q}} . \quad (2.26)$$

where $\dot{\mathbf{q}} = [\dot{\theta}_1, \dot{\theta}_2, \dot{\theta}_3]^T$ and $\dot{\mathbf{x}} = [v_{gx}, v_{gy}, v_{gz}]^T$, and where

$$J_q = \begin{bmatrix} b_{1x}f_{1y} - b_{1y}f_{1x} & 0 & 0 \\ 0 & b_{2x}f_{2y} - b_{2y}f_{2x} & 0 \\ 0 & 0 & b_{3x}f_{3y} - b_{3y}f_{3x} \end{bmatrix}, \text{ and}$$

$$J_x = \begin{bmatrix} f_{1x} & f_{2x} & f_{3x} \\ f_{1y} & f_{2y} & f_{3y} \\ f_{1z} & f_{2z} & f_{3z} \end{bmatrix}, \quad (2.27)$$

where

$$b_{ix} = b \cos\theta_i \cos\alpha_i , b_{iy} = b \cos\theta_i \sin\alpha_i , f_{ix} = f \cos (\theta_i + \phi_i) \cos\alpha_i ,$$

$$f_{iy} = f \cos (\theta_i + \phi_i) \sin\alpha_i , f_{iz} = f \sin (\theta_i + \phi_i) , \text{ and } [\alpha_1, \alpha_2, \alpha_3] = [0, \frac{2\pi}{3}, \frac{4\pi}{3}] .$$

Therefore, the Jacobian matrix J of the parallel manipulator is found $J = J_q^{-1} J_x$.

2.6 Summary

In this chapter, two ideas of conceptual design for the application in Minimally Invasive Surgery were proposed. These two proposals were also analyzed mathematically with practical challenges considered as well. It is found that the scheme of compliant parallel robotic instrument with multifunctional forceps is better than the other one. Afterwards, the further analyses of the parallel manipulator were conducted, such as kinematics analysis, workspace evaluation and Jacobian matrix derivation. These analyses are important to us to better understand how the parallel manipulator works, what are the performances, and how to improve the performances such that we can take the most advantages of the manipulator during surgeries as a surgical instrument.

Chapter 3 Stiffness Modeling

3.1 Introduction

In conventional stiffness studies of rigid-body parallel robots, it is assumed that the links are perfectly rigid and that the servo systems and mechanical transmission mechanisms are considered as the only sources of compliance (inverse of the stiffness) [46]. However, it is not the same case when analyzing the stiffness of compliant parallel robots. Unlike the rigid-body parallel robots whose stiffness is determined by the stiffness of mechanical transmission mechanisms and servo systems, the stiffness of compliant parallel manipulators is bound up with the stiffness of the compliant hinges.

Different from the conventional parallel mechanisms, the stiffness of compliant parallel mechanisms is not up to the stiffness of actuators but the stiffness of the compliant joints. In this chapter, the stiffness matrix method is employed to develop the stiffness matrix for the compliant parallel manipulator by first modeling the stiffness of one limb and then modeling the stiffness of the whole mechanism.

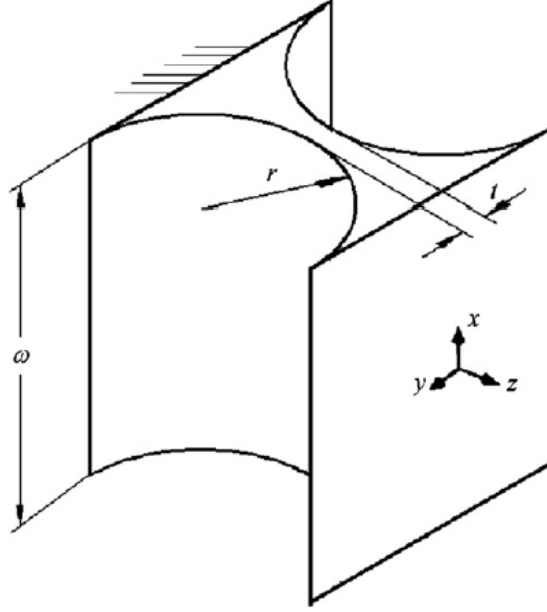


Figure 3.1. Right-circular flexure hinge and its local frame.

In this thesis, right-circular flexure hinges and right-circular flexure spherical hinges as shown in Figure 3.1 and 3.2, are used as the compliant joints. First of all, the local coordinate systems of a right-circular flexure hinge and a right-circular flexure spherical hinge are defined as shown in Figure 3.1 and 3.2 respectively. Given the linear relation between the applied load and deformation, when the load \mathbf{F} is exerted on a certain point, the infinitesimal translational and rotational displacements \mathbf{X} of that point are formulated [50]:

$$\mathbf{F} = [f_x, f_y, f_z, M_x, M_y, M_z]^T = \mathbf{K}\mathbf{X} = \mathbf{K}[\delta_x, \delta_y, \delta_z, \theta_x, \theta_y, \theta_z]^T, \quad (3.1)$$

$$\mathbf{X} = [\delta_x, \delta_y, \delta_z, \theta_x, \theta_y, \theta_z]^T = \mathbf{C}\mathbf{F} = \mathbf{C}[f_x, f_y, f_z, M_x, M_y, M_z]^T, \quad (3.2)$$

where \mathbf{K} is the stiffness matrix, and \mathbf{C} the compliance matrix. \mathbf{C} and \mathbf{K} are regular and symmetric, and inverse matrices of each other.

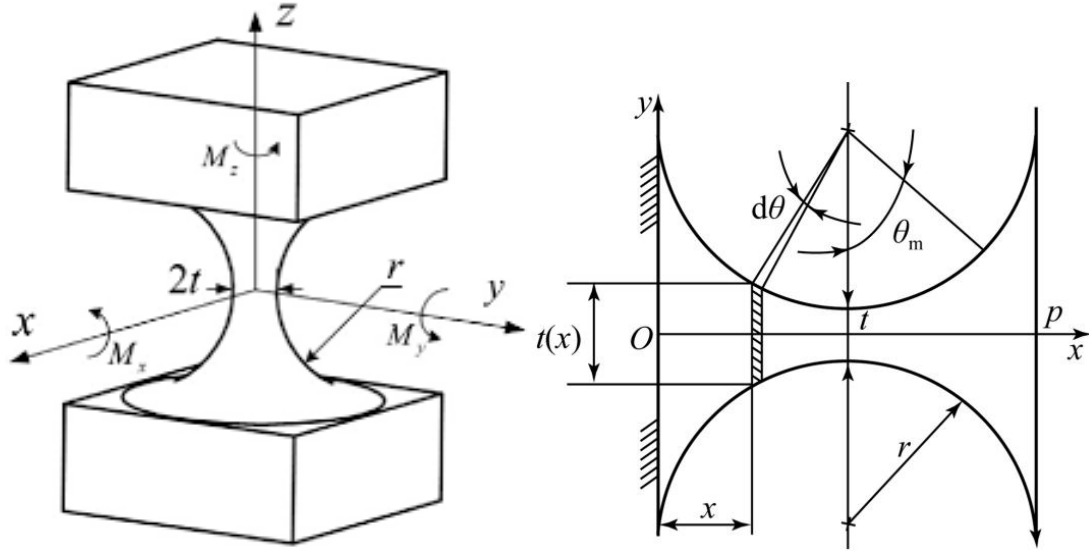


Figure 3.2. Right-circular flexure spherical hinge and its local frame.

The Compliance matrix C_R of a circular flexure hinge with respect to the local frames is given by [51]

$$\begin{bmatrix} \delta_x \\ \delta_y \\ \delta_z \\ \theta_x \\ \theta_y \\ \theta_z \end{bmatrix} = C_R \mathbf{F} = \begin{bmatrix} c_1 & 0 & 0 & 0 & c_3 & 0 \\ 0 & c_2 & 0 & -c_4 & 0 & 0 \\ 0 & 0 & c_5 & 0 & 0 & 0 \\ 0 & -c_4 & 0 & c_6 & 0 & 0 \\ c_3 & 0 & 0 & 0 & c_7 & 0 \\ 0 & 0 & 0 & 0 & 0 & c_8 \end{bmatrix} \begin{bmatrix} f_x \\ f_y \\ f_z \\ M_x \\ M_y \\ M_z \end{bmatrix}. \quad (3.3)$$

The approximation values of the factors of the Compliance matrix are shown in Table 3.1, where E and G are Young's modulus and shear modulus, respectively.

Table 3.1. Factors of the Compliance matrix of right-circular flexure hinge.

c_1	$\frac{9\pi r^{5/2}}{2Eb t^{5/2}} + \frac{3\pi r^{3/2}}{2Eb t^{3/2}}$
c_2	$\frac{12\pi r^2}{Eb^3} \left[\left(\frac{r}{t}\right)^{1/2} - \frac{1}{4} \right]$
c_3	$\frac{9\pi r^{3/2}}{2Eb t^{5/2}}$
c_4	$\frac{12r}{Eb^3} \left[\pi \left(\frac{r}{t}\right)^{1/2} - \frac{2 + \pi}{2} \right]$
c_5	$\frac{1}{Eb} \left[\pi \left(\frac{r}{t}\right)^{1/2} - \frac{\pi}{2} \right]$
c_6	$\frac{12r}{Eb^3} \left[\pi \left(\frac{r}{t}\right)^{1/2} - \frac{2 + \pi}{2} \right]$
c_7	$\frac{9\pi r^{1/2}}{2Eb t^{5/2}}$
c_8	$\frac{9\pi r^{3/2}}{4Gb t^{5/2}}$

And the compliance matrix \mathbf{C}_S of a right-circular flexure spherical hinge with respect to the local frame is given by [50]

$$\begin{bmatrix} \delta_x \\ \delta_y \\ \delta_z \\ \theta_x \\ \theta_y \\ \theta_z \end{bmatrix} = \mathbf{C}_S \mathbf{F} = \begin{bmatrix} C_{11} & 0 & 0 & 0 & 0 & 0 \\ 0 & C_{22} & 0 & 0 & 0 & C_{26} \\ 0 & 0 & C_{33} & 0 & C_{35} & 0 \\ 0 & 0 & 0 & C_{44} & 0 & 0 \\ 0 & 0 & C_{53} & 0 & C_{55} & 0 \\ 0 & C_{62} & 0 & 0 & 0 & C_{66} \end{bmatrix} \begin{bmatrix} f_x \\ f_y \\ f_z \\ M_x \\ M_y \\ M_z \end{bmatrix}. \quad (3.4)$$

The approximation values of the factors of the Compliance matrix are shown in Table 3.2. In this table, the value of κ is evaluated at 1 for average shear force; ν is the Poisson's ratio of the material, and E and G are Young's modulus and shear modulus, respectively. The values of I_1 , I_2 and I_4 can be found through the following

formulae:

$$I_1 = \frac{1}{2r} \left(\frac{1}{\xi(\xi+2)} + \frac{2}{(\xi(\xi+2))^{3/2}} \tan^{-1} \sqrt{\frac{\xi+2}{\xi}} \right), \quad (3.5)$$

$$I_2 = \frac{1}{8r^3(\xi(\xi+2))^3} \left(\frac{6\xi^5 + 30\xi^4 + 70\xi^3 + 90\xi^2 + 59\xi + 15}{6(\xi+1)^3} + \frac{4\xi^2 + 8\xi + 5}{\sqrt{\xi(\xi+2)}} \tan^{-1} \sqrt{\frac{\xi+2}{\xi}} \right), \quad (3.6)$$

$$I_4 = \frac{1}{8r^3(\xi(\xi+2))^3} \left(\frac{8\xi^4 + 32\xi^3 + 57\xi^2 + 50\xi + 15}{6(\xi+1)^2} + \frac{5(\xi+1)^2}{\sqrt{\xi(\xi+2)}} \tan^{-1} \sqrt{\frac{\xi+2}{\xi}} \right). \quad (3.7)$$

where $\xi = \frac{t}{2r}$.

Table 3.2. Factors of the Compliance matrix of right-circular flexure spherical hinge.

C_{11}	$\frac{4I_1}{\pi E}$
C_{22}	$\frac{64I_4 + \kappa(1+\nu)I_1}{\pi E}$
C_{33}	C_{22}
C_{44}	$(1+\nu)C_{66}$
C_{55}	C_{66}
C_{66}	$\frac{64I_2}{\pi E}$
$C_{26}=C_{62}$	rC_{55}
$C_{35}=C_{53}$	$-C_{26}$

3.2 Stiffness Modeling of One Limb

In this study, each limb of the compliant parallel robot has links in serial connections and links in parallel connections. For those compliant hinges which are considered as flexure members with the local stiffness \mathbf{K}_i and compliance matrix \mathbf{C}_i established in the local frame attached to that flexure member as shown in Figure 3.3. Since the stiffness of the link is far larger than the stiffness of the flexure joints, it is assumed that the deformations arise only from the compliant joints.

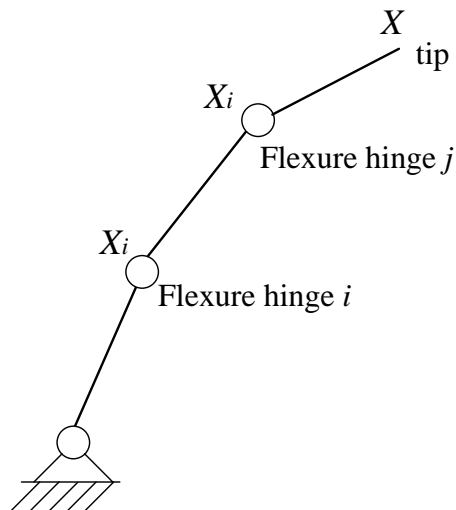


Figure 3.3. A serial chain.

For n flexure members in a serial chain, the accumulation of deformations \mathbf{X} at the tip is

$$\mathbf{X} = \sum_{i=1}^n \Delta \mathbf{X}_i , \quad (3.8)$$

where $\Delta \mathbf{X}_i$ is a 6×1 vector of elastic deformations at the tip of the chain with respect to the reference frame.

As the zero virtual work principle states, the Jacobian matrix \mathbf{J}_i^T transforms a vector \mathbf{F} of external force at the tip to a vector of reaction force \mathbf{F}_i at the flexure member. Therefore, we have

$$\begin{aligned}\mathbf{F}_i &= \mathbf{J}_i^T \mathbf{F} \text{ , and} \\ \Delta \mathbf{X}_i &= \mathbf{J}_i \mathbf{X}_i \text{ .}\end{aligned}\tag{3.9}$$

Equation (3.8) can be rewritten as

$$\mathbf{X} = \sum_{i=1}^n \Delta \mathbf{X}_i = \sum_{i=1}^n \mathbf{J}_i \mathbf{X}_i \text{ .}\tag{3.10}$$

The 6×6 Jacobian matrix \mathbf{J}_i transforms a 6×1 vector \mathbf{X}_i of elastic deformations of the flexure member with respect to a local frame, to a 6×1 vector $\Delta \mathbf{X}_i$ at the tip of the chain with respect to the reference frame. The Jacobian matrix is given by [52] as

$$\mathbf{J}_i = \begin{bmatrix} \mathbf{R}_i & -\mathbf{R}_i \mathbf{S}(\mathbf{r}_i) \\ \mathbf{0}_{3 \times 3} & \mathbf{R}_i \end{bmatrix} \text{ ,}\tag{3.11}$$

where \mathbf{R}_i denotes the orientation of reference frame with respect to local frame, \mathbf{r}_i indicating the position vector pointing from the origin of the reference frame to local frame, and $\mathbf{S}(\mathbf{r}_i)$ the skew-symmetric operator.

$$\mathbf{S}(\mathbf{r}_i) = \begin{bmatrix} 0 & -r_{iz} & r_{iy} \\ -r_{iz} & 0 & r_{ix} \\ r_{iy} & r_{ix} & 0 \end{bmatrix} \text{ .}\tag{3.12}$$

Let \mathbf{C}_i denote the local compliance matrix of the flexure members, from Equations (3.2), (3.8) and (3.9), we have

$$\mathbf{C}\mathbf{F} = \sum_{i=1}^n \mathbf{J}_i \mathbf{C}_i \mathbf{F}_i = \sum_{i=1}^n \mathbf{J}_i \mathbf{C}_i \mathbf{J}_i^T \mathbf{F}_i \text{ .}\tag{3.13}$$

Thus, the compliance of the flexure hinges in serial connections is obtained,

$$C = \sum_{i=1}^n J_i C_i J_i^T . \quad (3.14)$$

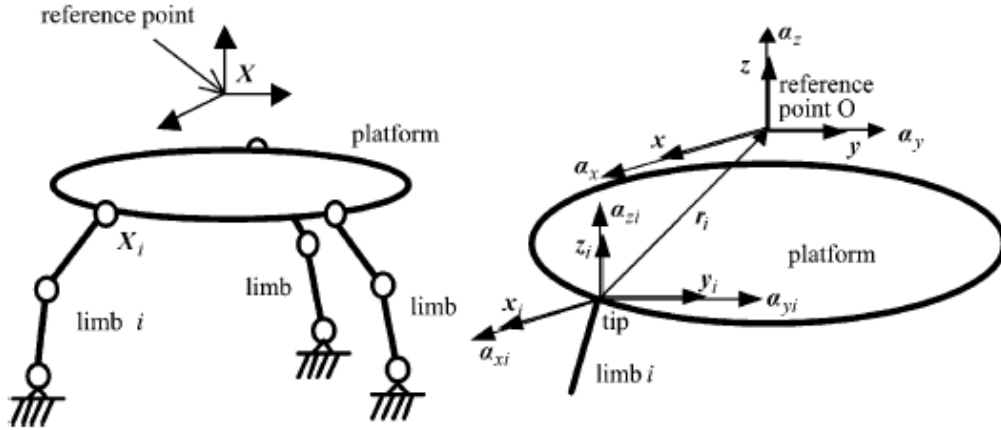


Figure 3.4. A parallel mechanism with local and reference coordinates [50].

For n flexure members in a parallel connections or n limbs in a parallel manipulator, it is assumed that the moving platform and tips of the limbs have the same angular displacement. Nevertheless, the linear displacements are different. The vector of the tip of the i th limb X_i can be transformed to the displacement vector of compliant parallel mechanism X by pre-multiplying a transformation matrix J_i , as shown in Figure 3.4.

$$X = J_i X_i , \quad (3.15)$$

where J_i is the transformation matrix from the reference of the i th limb, whose reference point is set at the tips of limbs, to the reference of the compliant parallel mechanism. Similarly, the force F applied on the platform described in the reference frame of the compliant parallel mechanism can be obtained by distributed force F_i described in the reference frame of the limbs [53].

$$\mathbf{F} = \mathbf{K}\mathbf{X} = \sum_{i=1}^n \mathbf{J}_{Fi} \mathbf{F}_i , \quad (3.16)$$

where \mathbf{J}_{Fi} is the transformation matrix of the applied force from the local frame to the reference frame [52]:

$$\mathbf{J}_{Fi} = \mathbf{J}_i^T = \begin{bmatrix} \mathbf{R}_i & \mathbf{0}_{3 \times 3} \\ -\mathbf{R}_i \mathbf{S}(\mathbf{r}_i) & \mathbf{R}_i \end{bmatrix} , \quad (3.17)$$

Let \mathbf{K} and \mathbf{K}_i be the stiffness matrix of the compliant parallel mechanism and the stiffness of the i th limb, respectively. From Equations (3.15) and (3.16), one can obtain that

$$\mathbf{F} = \mathbf{K}\mathbf{X} = \sum_{i=1}^n \mathbf{J}_{Fi} \mathbf{F}_i = \sum_{i=1}^n \mathbf{J}_{Fi} \mathbf{K}_i \mathbf{X}_i = \sum_{i=1}^n \mathbf{J}_i^T \mathbf{K}_i \mathbf{J}_i^{-1} \mathbf{X} . \quad (3.18)$$

Therefore, the stiffness of the parallel mechanism becomes

$$\mathbf{K} = \sum_{i=1}^n \mathbf{J}_i^{-T} \mathbf{K}_i \mathbf{J}_i^{-1} . \quad (3.19)$$

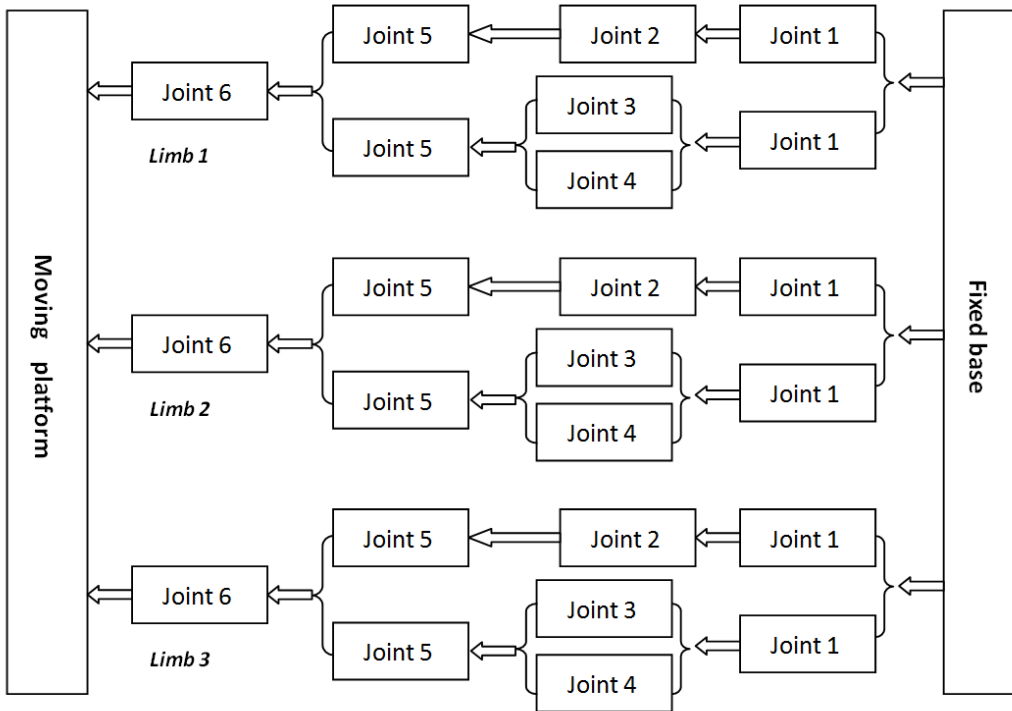


Figure 3.5. The link-pair relationship diagram of the compliant parallel mechanism.

In Figure 3.5, the moving platform and the fixed base are connected through three identical chains of limbs. Each limb consists of three parts, joint125, joint12345 and joint6, connected in serial chains. Joint2 and joint4, joint3 and joint5 are in serial chains, respectively, and the two serial chains comprise the joint2345 in a parallel chain. With assumption that the deformations only arise from the flexure joints, each joint is assumed to be a flexure member with the local stiffness matrix \mathbf{K}_i and the compliance matrix \mathbf{C}_i established in the local frame referring to Fig. 3.5, as shown in Fig.3.6.

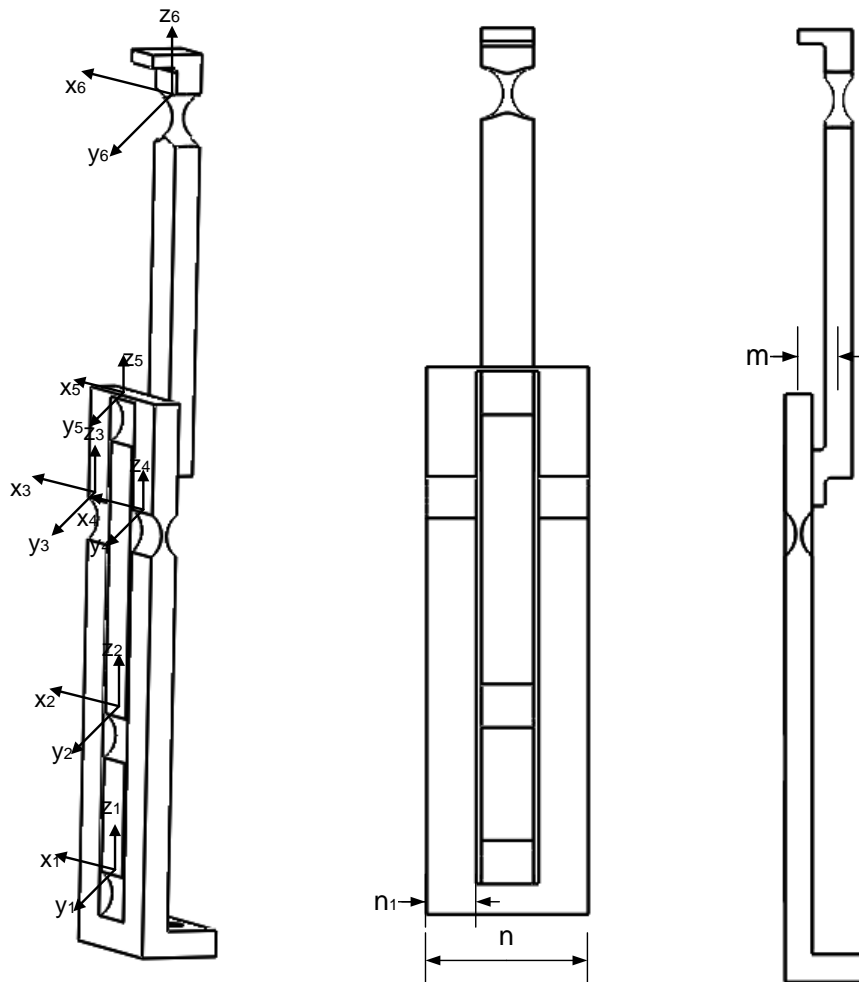


Figure 3.6. Geometry relationships among coordinate systems.

Setting up an intermediate frame O_i with its orientation is coinciding with the local frame of the joint1 and its original located at the local frame of the joint6. Then the transform matrices J_i of the joints2, 3, 4 and 5 can be obtained as follows:

$$J_1 = \begin{bmatrix} I_{3 \times 3} & -S(\mathbf{r}_1) \\ \mathbf{0}_{3 \times 3} & I_{3 \times 3} \end{bmatrix}, \quad (3.20)$$

$$J_2 = \begin{bmatrix} I_{3 \times 3} & -S(\mathbf{r}_2) \\ \mathbf{0}_{3 \times 3} & I_{3 \times 3} \end{bmatrix}, \quad (3.21)$$

$$J_3 = \begin{bmatrix} I_{3 \times 3} & -S(\mathbf{r}_3) \\ \mathbf{0}_{3 \times 3} & I_{3 \times 3} \end{bmatrix}, \quad (3.22)$$

$$J_4 = \begin{bmatrix} I_{3 \times 3} & -S(\mathbf{r}_4) \\ \mathbf{0}_{3 \times 3} & I_{3 \times 3} \end{bmatrix}, \quad (3.23)$$

$$J_5 = \begin{bmatrix} I_{3 \times 3} & -S(\mathbf{r}_5) \\ \mathbf{0}_{3 \times 3} & I_{3 \times 3} \end{bmatrix}. \quad (3.24)$$

The position vectors in Equations (3.20) through (3.24), pointing from the origins of local frames to the reference frame are found as follows:

$$\begin{aligned} \mathbf{r}_1 &= [0, -m, (a + d + e)]^T, \quad \mathbf{r}_2 = [0, -m, (c + e)]^T, \\ \mathbf{r}_3 &= \left[\frac{n - n_1}{2}, -m, (d + e) \right]^T, \quad \mathbf{r}_4 = \left[\frac{n - n_1}{2}, -m, (d + e) \right]^T, \text{ and} \\ \mathbf{r}_5 &= [0, -m, e]^T. \end{aligned} \quad (3.25)$$

The compliance of the serial chain containing Joint 1, 2, and 5 can be obtained,

$$\mathbf{C}_{125} = \mathbf{C}_1 + \mathbf{C}_2 + \mathbf{C}_5 = J_1 \mathbf{C}_R J_1^T + J_2 \mathbf{C}_R J_2^T + J_5 \mathbf{C}_R J_5^T. \quad (3.26)$$

And the compliance of the serial chain composed of Joint 1, 3, 4, and 5 can be calculated,

$$\mathbf{C}_{1345} = \mathbf{C}_1 + \mathbf{C}_{34} + \mathbf{C}_5 = J_1 \mathbf{C}_R J_1^T + J_5 \mathbf{C}_R J_5^T + \mathbf{C}_{34}. \quad (3.27)$$

Since Joint 3 is connected with Joint 4 in parallel structure, the compliance \mathbf{C}_{34} can be found via Equations (3.28) through (3.30),

$$\mathbf{C}_{34} = \mathbf{K}_{34}^{-1}, \quad (3.28)$$

$$\mathbf{K}_{34} = \mathbf{K}_3 + \mathbf{K}_4 = J_3^{-T} \mathbf{K}_R J_3^{-1} + J_4^{-T} \mathbf{K}_R J_4^{-1}, \text{ and} \quad (3.29)$$

$$\mathbf{K}_R = \mathbf{C}_R^{-1} . \quad (3.30)$$

Since the serial chain containing Joint 1, 2, and 5 is in parallel with another serial chain containing Joint 1, 3, 4, and 5, and then the new chain containing these two serial chains is in serial with Joint 6 as shown in Figure 3.5, then the compliance of one limb can be expressed as

$$\mathbf{C}_{limb} = \mathbf{J}_{12345} \mathbf{C}_{12345} \mathbf{J}_{12345}^T + \mathbf{C}_s = \mathbf{K}_{limb}^{-1} , \quad (3.31)$$

where \mathbf{C}_s is the compliance of Joint 6, which is a flexure spherical hinge, \mathbf{C}_{12345} is given by

$$\mathbf{C}_{12345} = \mathbf{K}_{12345}^{-1} , \text{ and}$$

$$\mathbf{K}_{12345} = \mathbf{K}_{125} + \mathbf{K}_{1345} = \mathbf{C}_{125}^{-1} + \mathbf{C}_{1345}^{-1} . \quad (3.32)$$

The Jacobian matrix \mathbf{J}_{12345} is given by

$$\mathbf{J}_{12345} = \begin{bmatrix} \mathbf{R}_y\left(-\frac{\pi}{2}\right) \mathbf{R}_z\left(-\frac{\pi}{2}\right) & \mathbf{0}_{3 \times 3} \\ \mathbf{0}_{3 \times 3} & \mathbf{R}_y\left(-\frac{\pi}{2}\right) \mathbf{R}_z\left(-\frac{\pi}{2}\right) \end{bmatrix} , \quad (3.33)$$

where the rotation matrices $\mathbf{R}_y(-\pi/2)$ and $\mathbf{R}_z(-\pi/2)$ denote the local frames rotating about y and z-axes, respectively to match the reference frame. The rotation matrices expressing the rotation of an angle θ about x, y, and z-axes are given below:

$$\begin{aligned} \mathbf{R}_x(\theta) &= \begin{bmatrix} 1 & 0 & 0 \\ 0 & c\theta & -s\theta \\ 0 & s\theta & c\theta \end{bmatrix}, \mathbf{R}_y(\theta) = \begin{bmatrix} c\theta & 0 & s\theta \\ 0 & 1 & 0 \\ -s\theta & 0 & c\theta \end{bmatrix}, \text{ and} \\ \mathbf{R}_z(\theta) &= \begin{bmatrix} c\theta & -s\theta & 0 \\ s\theta & c\theta & 0 \\ 0 & 0 & 1 \end{bmatrix} . \end{aligned} \quad (3.34)$$

3.3 Stiffness Modeling of the Compliant Parallel Mechanism

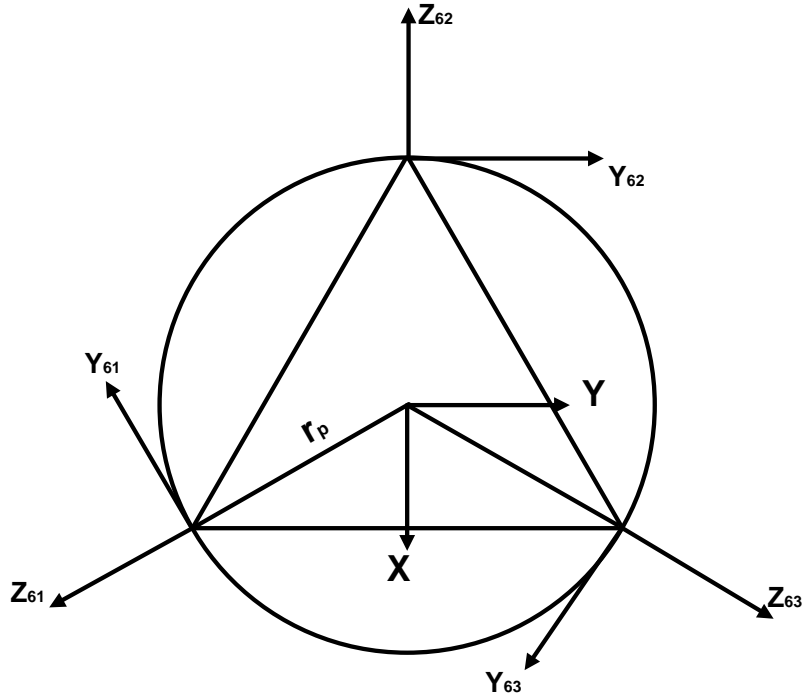


Figure 3.7. Geometry relationships among coordinate systems.

The stiffness of one limb has just been completed. Now the stiffness of the compliant parallel mechanism can be derived. Referring to Figure 3.7, the stiffness of the compliant mechanism can be found as,

$$\mathbf{K} = \mathbf{J}_{61}^{-T} \mathbf{K}_{limb} \mathbf{J}_{61}^{-1} + \mathbf{J}_{62}^{-T} \mathbf{K}_{limb} \mathbf{J}_{62}^{-1} + \mathbf{J}_{63}^{-T} \mathbf{K}_{limb} \mathbf{J}_{63}^{-1} , \quad (3.35)$$

where

$$\mathbf{J}_{61} = \begin{bmatrix} \mathbf{R}_y\left(\frac{\pi}{2}\right) \mathbf{R}_x\left(-\frac{2\pi}{3}\right) & -\mathbf{R}_y\left(\frac{\pi}{2}\right) \mathbf{R}_x\left(-\frac{2\pi}{3}\right) \mathbf{S}(\mathbf{r}_{61}) \\ \mathbf{0}_{3 \times 3} & \mathbf{R}_y\left(\frac{\pi}{2}\right) \mathbf{R}_x\left(-\frac{2\pi}{3}\right) \end{bmatrix} , \quad (3.36)$$

$$\mathbf{J}_{62} = \begin{bmatrix} \mathbf{R}_y\left(\frac{\pi}{2}\right) & -\mathbf{R}_y\left(\frac{\pi}{2}\right) \mathbf{S}(\mathbf{r}_{62}) \\ \mathbf{0}_{3 \times 3} & \mathbf{R}_y\left(\frac{\pi}{2}\right) \end{bmatrix} , \text{ and} \quad (3.37)$$

$$J_{63} = \begin{bmatrix} \mathbf{R}_y\left(\frac{\pi}{2}\right)\mathbf{R}_x\left(\frac{2\pi}{3}\right) & -\mathbf{R}_y\left(\frac{\pi}{2}\right)\mathbf{R}_x\left(\frac{2\pi}{3}\right)\mathbf{S}(\mathbf{r}_{63}) \\ \mathbf{0}_{3 \times 3} & \mathbf{R}_y\left(\frac{\pi}{2}\right)\mathbf{R}_x\left(\frac{2\pi}{3}\right) \end{bmatrix}. \quad (3.38)$$

And the position vectors $\mathbf{r}_{61}, \mathbf{r}_{62}, \mathbf{r}_{63}$ in the above Jacobian matrices are,

$$\mathbf{r}_{61} = \mathbf{r}_{62} = \mathbf{r}_{63} = [0, 0, -r_p]^T, \quad (3.39)$$

where r_p is the radius of the moving platform as shown in Figure 3.7.

3.4 Stiffness mapping and Discussions

Based on the stiffness modeling derived above, the stiffness mapping versus geometric parameters of the compliant parallel mechanism can be obtained and are graphically displayed in the Figures 3.8 to 3.10. For example, the lengths of link b and c, l_b and l_c are two parameters of interests. By varying the values of these two parameters while the other parameters are assigned to be constants, the stiffness mesh and contours graphs can be found as shown in the figures. From the graphs, one can intuitively view the stiffness distribution and evaluate the influence of every geometric parameter [54].

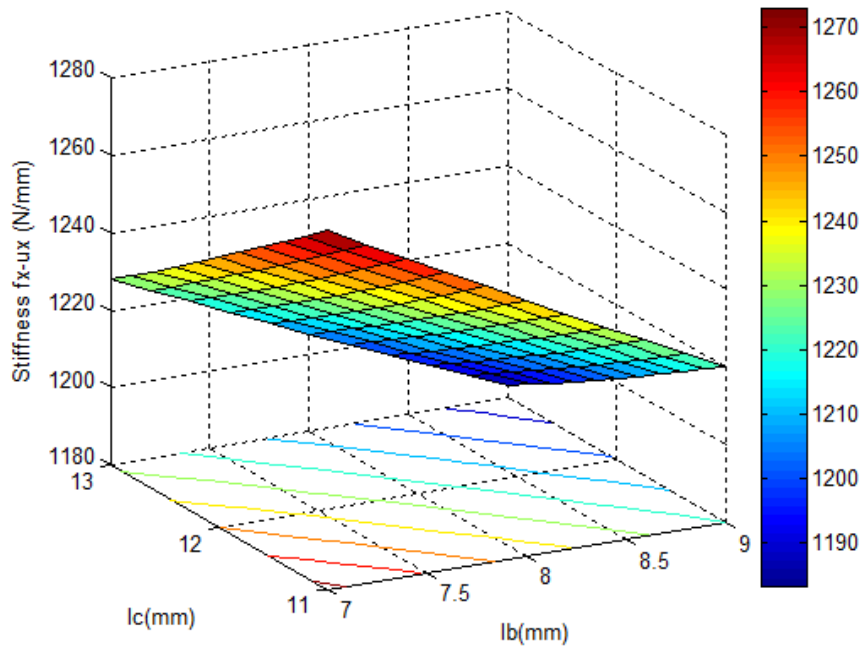


Figure 3.8. Stiffness factor f_{x-ux} versus parameters l_b and l_c .

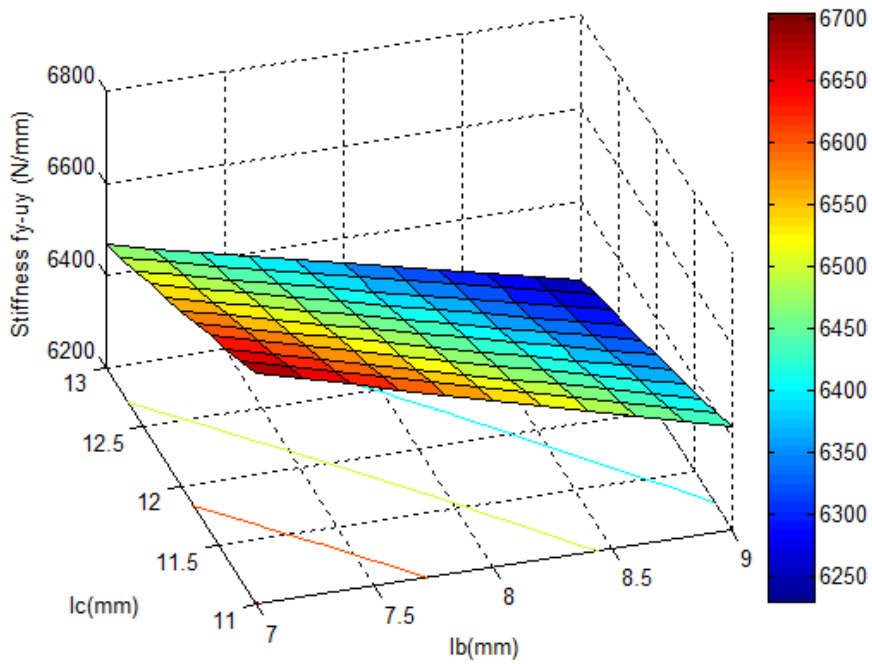


Figure 3.9. Stiffness factor f_{y-uy} versus parameters l_b and l_c .

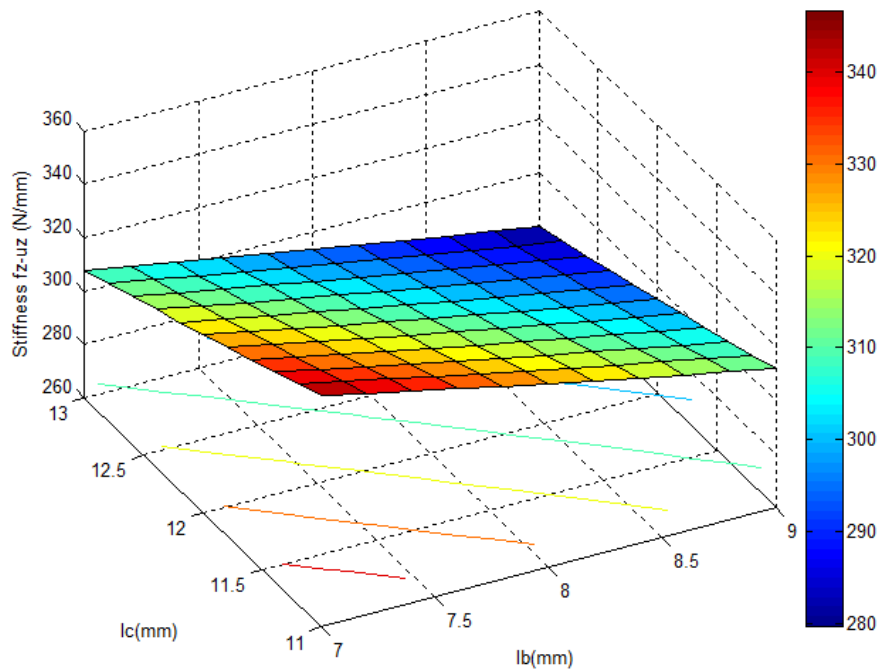


Figure 3.10. Stiffness factor fz-uz versus parameters l_b and l_c .

From the analysis and modeling above, it can be noted that the stiffness of the compliant parallel mechanism is related to the following geometric parameters: the length of link b, l_b ; the length of link c, l_c ; the length of link e, l_e ; the radius of the base, r_b ; and the radius of the platform, r_p . From the Stiffness mapping shown above, we can maximize the stiffness in some direction. However, if more geometric parameters are involved and the stiffness in all directions are needed to obtain a stiffness as large as possible, then the method of stiffness mapping as illustrated above might be very clumsy and time consuming. Therefore, the stiffness is in need to be optimized with regard to the geometric parameters. The optimization of stiffness will be discussed in detail in the following chapter with Genetic Algorithm.

3.5 Summary

This chapter presents the stiffness modeling of the limb and the compliant parallel mechanism. The stiffness of the mechanism was calculated by considering the compliance of the flexure hinges connecting the links with the base and the moving platform. The connecting pattern of the hinges are also considered and the stiffness matrices are constructed by the means of transforming matrices of compliance and the matrix method. Lastly, the stiffness mapping with respect to geometric parameters of interests was presented graphically.

Chapter 4 Optimization of the Compliant Parallel Robotic Surgical Instrument

4.1 Introduction

The workspace and stiffness are important performance indices of the parallel robotic mechanisms and have been analyzed in the above chapters. However, these indices are analyzed based on the preliminary parameters of the link lengths and the preliminary sizes of the platform and the base. They can be designed more properly with larger workspace volume and bigger stiffness in different directions as desired if the optimization method is utilized.

In this chapter, the workspace and directional stiffness will be optimized with respect to the lengths of the links and sizes of the platform and the base, employing the built-in MATLAB optimization toolbox.

An optimization is conducted with objective function being constructed. Objective function is the mathematic expression of the problem to be optimized. Single objective optimization will be explored as well as multiobjective optimization in the following sections. Since when one objective function is optimized to get an optimal value with a set of variables, it is very likely to make another objective function less optimal. For example, when workspace is optimized to have a largest

volume with a set of lengths of the links a , b , and c ; however, with these link lengths the stiffness in different directions might possibly be very poor. Hence, the multiobjective optimization is in need to solve this problem. For most cases, different objectives cannot achieve optimal values at the same time, but this multiobjective optimization provides a series of data points indicating some “optimal values” for decision makers to choose. With those visualized data points, one can choose a data point which satisfies a near optima of a more important performance index and meanwhile guarantees another performance index with a value in an acceptable range. More details will be explored in the section of multiobjective optimization with an example illustrated.

The Genetic Algorithm, a type of artificial intelligent optimization method is used in this study. Genetic Algorithm is well known to solve both linear and nonlinear problems by exploring all areas of state space and greatly employing promising regions through mutation, crossover, and selection operations applied to individuals in the population [55]. By evaluating possible the solutions/individuals with respect to the degree of fitness from exploring the population, it tells how well the solutions or individuals are to the optimization problems [56]. Basically, Genetic Algorithms have the advantages of robustness and good convergence, including not requiring the gradient information about the objective functions, not vulnerable to the discontinuities of the objective functions, applicable to various large scale problems [57]. how the optimization rationale of Genetic Algorithms. Figure 4.1 shows how the Genetic Algorithm works.

Since the Genetic Algorithm optimization and Genetic Algorithm optimization for multiobjective are integrated in MATLAB, the optimization toolbox is a great tool to use in this study.

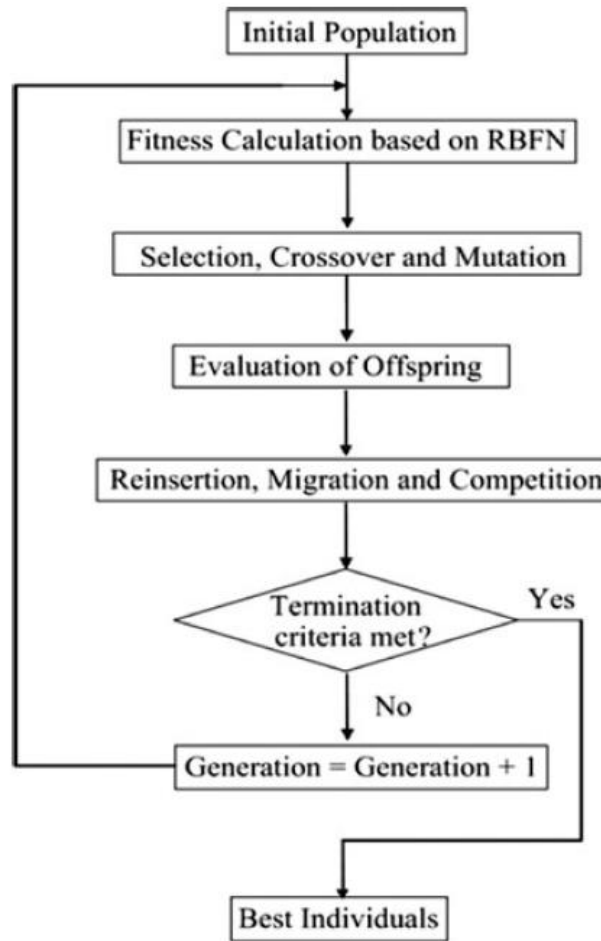


Figure 4.1. Schematic representation of the optimization rationale based on Genetic Algorithms [55].

4.2 Constraints and Optimization Setup

Due to the restricted surgical area inside the human body when surgeons are performing Minimally Invasive Surgeries, some constraints are imposing on the dimensions of the parallel robotic surgical instrument. Although the parallel robotic manipulator was first designed with preliminary parameters even considering the constraints, those parameters are not optimal to guarantee that it should have a large workspace and enough stiffness. Therefore, objective functions have to be set up and parameters have to be chosen to be optimized to redesign the parallel robotic manipulator in order to have a better performance, namely bigger workspace and larger stiffness.

Considering the practical constraints and from the derivations of inverse kinematics, forward kinematics and the stiffness analysis, the parameters are chosen as shown below as well as the boundaries of these parameters to be optimized.

The objective functions of workspace and stiffness are from the derivation of kinematics and stiffness analysis, respectively. And they are presented in the Chapter 2 and 3. Now here these objective functions can be expressed as:

$$f1 = \max(workspace), \quad workspace(lb, rb, rp) ; \quad (4.1)$$

$$f2 = \max(stiffness), \quad stiffness(rp, lb, lc, ld, le) ; \quad (4.2)$$

where r_b and r_p are the radii of the base and platform, respectively; l_b , l_c , l_d , l_e the length of link b, c, d, and e respectively. And the boundaries of these parameters to be optimized are shown in Table 4.1.

The detailed MATLAB codes for the calculations can be found in the Appendix. What is followed is that the optimizations using Genetic Algorithm with MATLAB Toolbox and results will be shown and analyzed.

Table 4.1. Boundaries of the geometric parameters to be optimized (mm).

Parameter	Range
r_b	(11.4, 15.6)
r_p	(9.6, 14.4)
l_b	(11.4, 15.6)
l_c	(11.4, 15.6)
l_d	(4, 6)
l_e	(8, 12)

4.3 Optimization of the Workspace

In the previous chapter, it has been shown that workspace needs to be optimized to get better performance out of the parallel manipulator. In this section, the workspace optimized using Genetic Algorithm with MATLAB Toolbox is shown in Figure 4.2. According to the derivation of kinematics, there are three parameters in the objective

function which can be found in the Appendix, and the range of the parameters are put into the optimization tool. After all the necessary iterations of implementing Genetic Algorithm, the results are given in Figure 4.3 and 4.4. Since this optimization tool solves only the minimization problem, but the maximization of workspace is needed here, the minus sign was added to the objective function in the front. That's why we got the negative maximum value of the volume at 361.2919 mm^3 , with the values of the parameters at $l_b = 15.59 \text{ mm}$, $r_b = 12.49 \text{ mm}$, and $r_p = 11.294 \text{ mm}$.

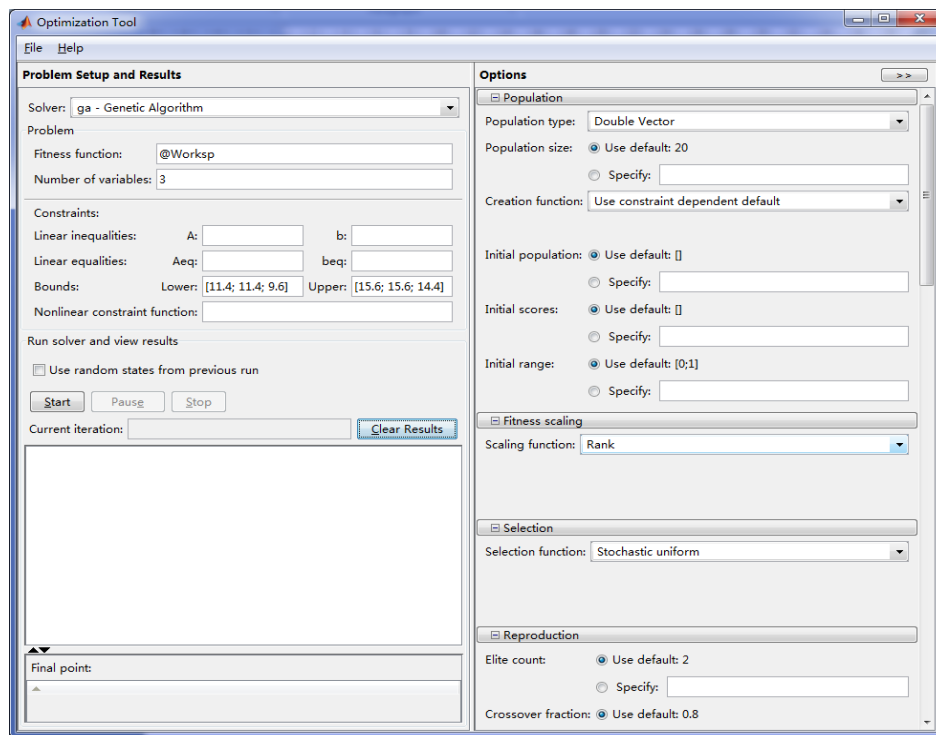


Figure 4.2. Optimization of workspace using MATLAB optimization toolbox.

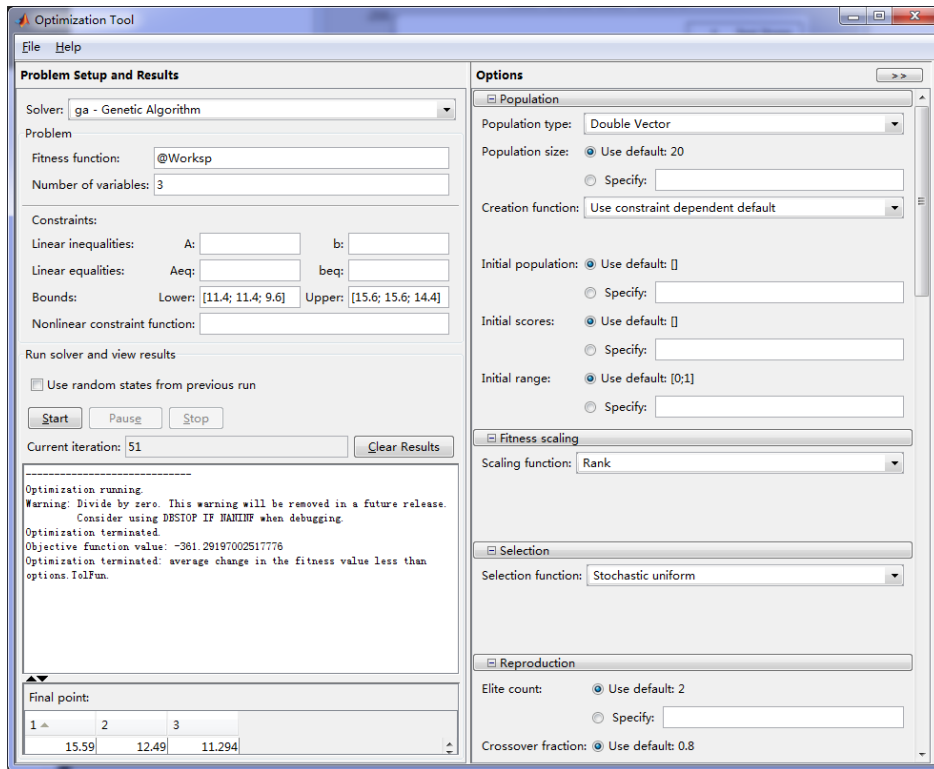


Figure 4.3. Optimization result of workspace.

These parameters are input to the function which evaluates the volume and graphically displays the workspace again to get the result presented in Figure 4.4 and 4.5. From this figure, one might notice that the volume has a very insignificant difference from that given by the optimization tool. That is because the round-off error, which can be neglected.

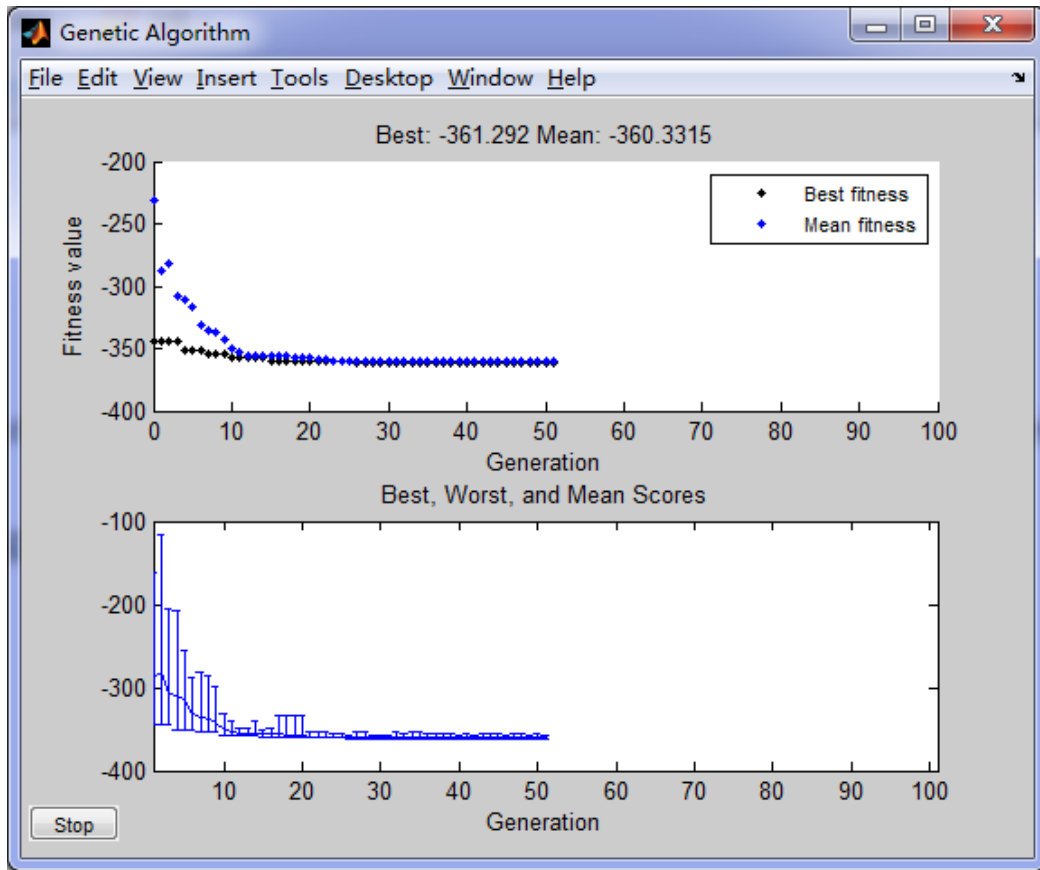


Figure 4.4. Optimization result of workspace.

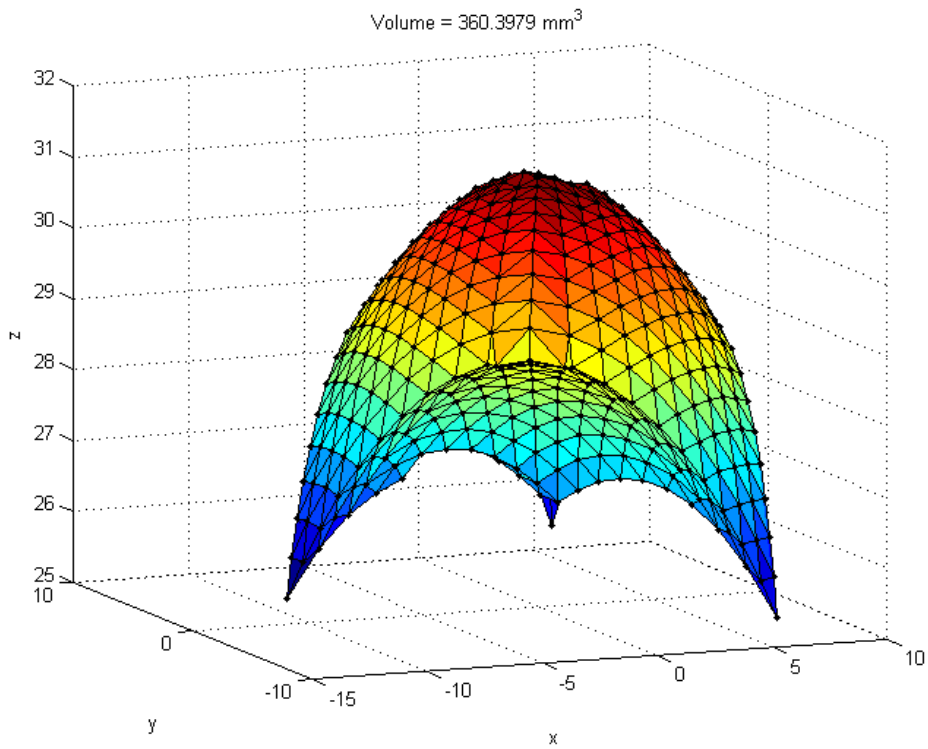


Figure 4.5. Optimized workspace and volume (view from the top).

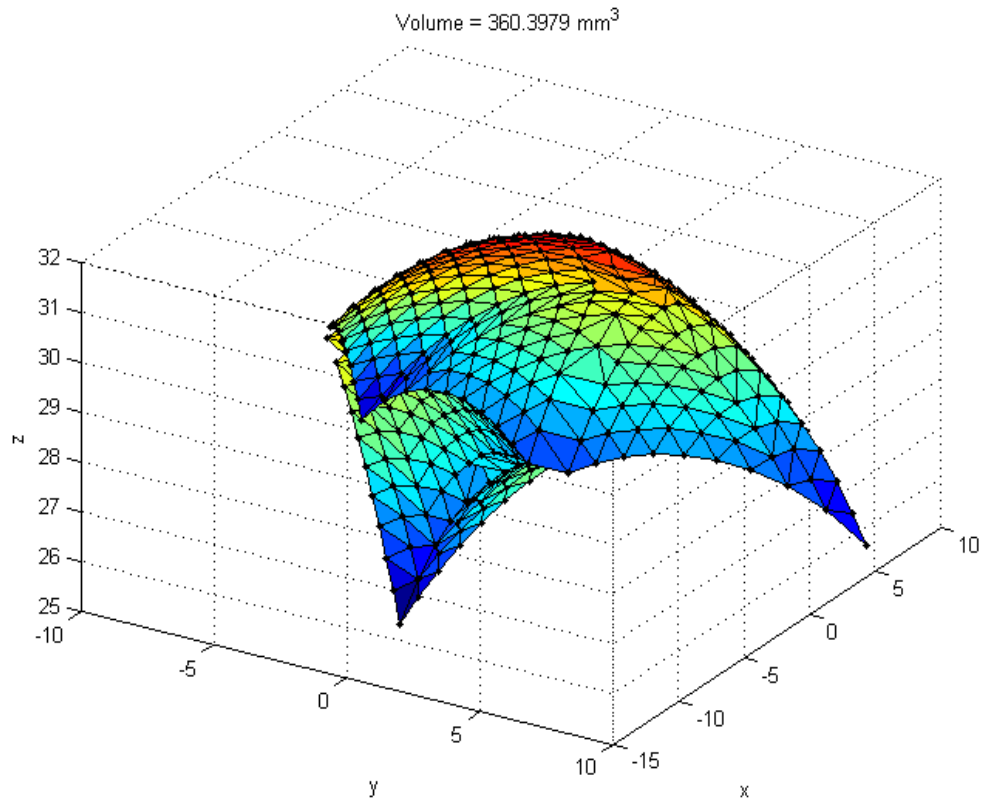


Figure 4.6. Optimized workspace and volume (view from the bottom).

4.4 Optimization of the Stiffness

Stiffness show the resistant ability of the mechanism to deformations. It is an important performance index of the mechanism since smaller stiffness means the mechanism may undergo large deformations due to external forces, which may decrease the accuracy of the mechanism. Thus the stiffness of a parallel mechanism is preferably to be higher. The Stiffness optimization using MATLAB Toolbox and its results are shown in Figure 4.7 and 4.8.

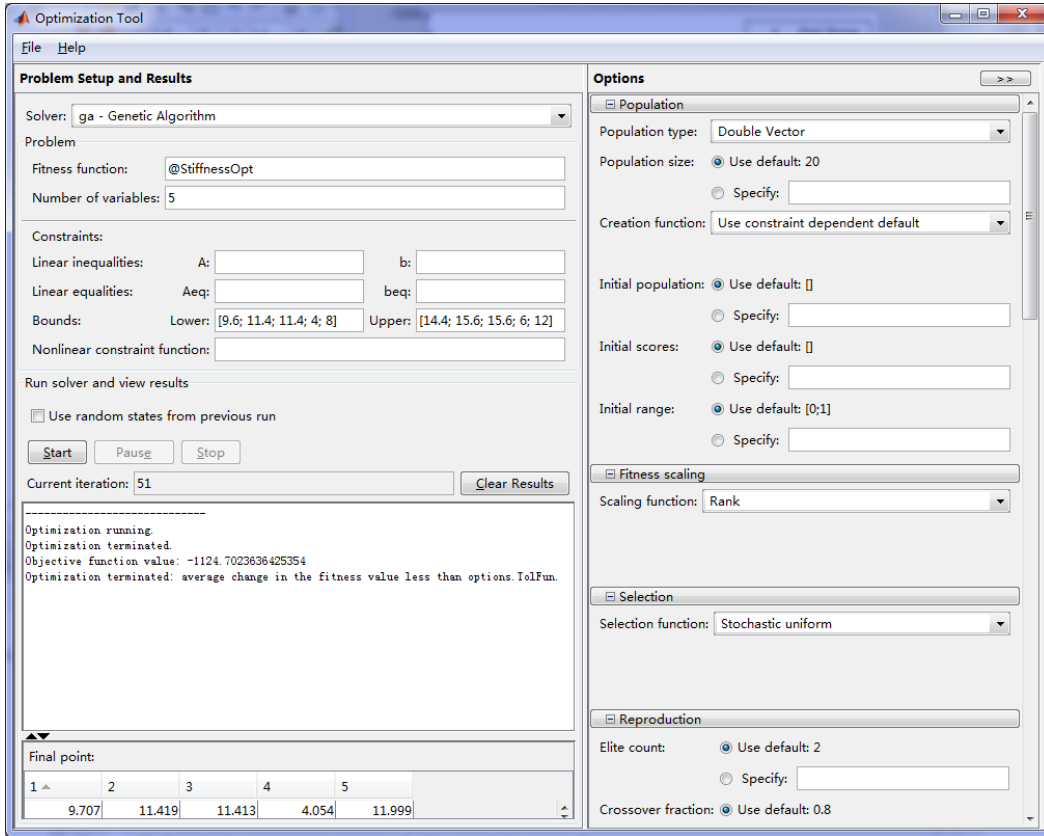


Figure 4.7. Stiffness optimization and the results.

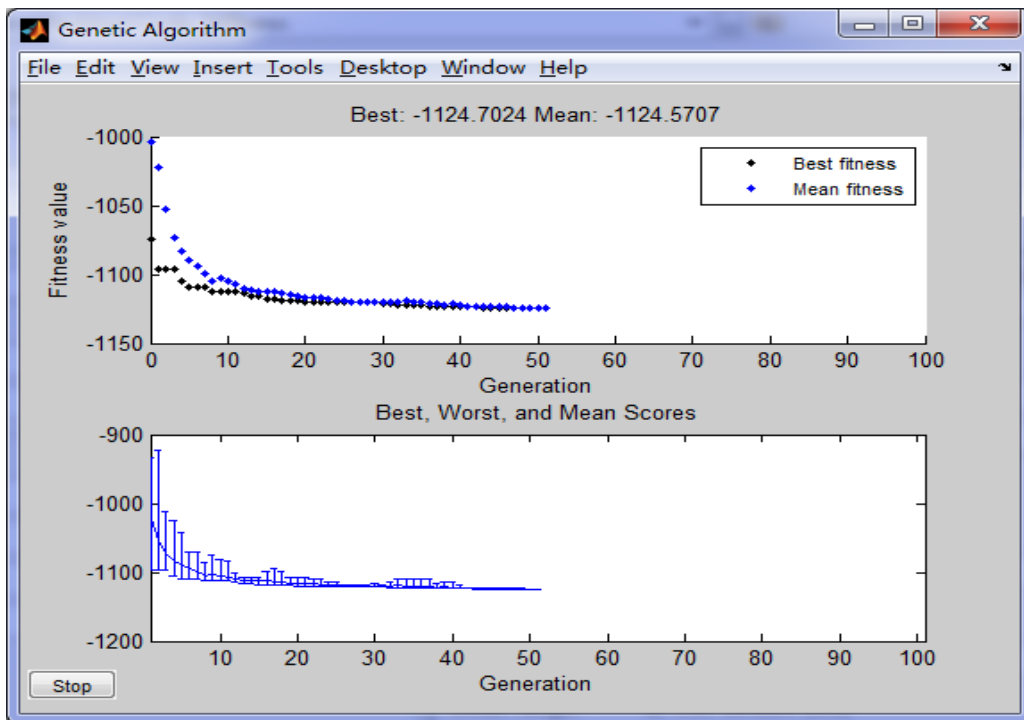


Figure 4.8. Stiffness optimization and the results.

The result shows the best value of stiffness is 1124.7024 N/mm, with the optimized parameters at $r_p = 9.707$ mm, $l_b = 11.419$ mm, $l_c = 11.413$ mm, $l_d = 4.054$ mm, and $l_d = 11.999$ mm.

4.5 Multiobjective Optimization

Since the calculated aspects of the stiffness in different directions have opposing effects on the design parameters selected for optimization, the stiffness in three directions cannot achieve their largest value at the same time. By setting the objective functions to be a combination of each of the individual objectives (stiffness in x, y, and z directions) an optimization problem is formulated.

$$\begin{cases} f_1 = \max(stiffness_x) \\ f_2 = \max(stiffness_y) \\ f_3 = \max(stiffness_z) \end{cases}$$

The results are displayed in Figure 4.9 and 4.10. Figure 4.10 shows the Pareto Front plot of the multiobjective optimization, which tells the best combination of the parameters. Since all these objective functions cannot get their optimal values at the same time, the decision maker has to choose which one combination should be used to modify the design based on the practical working conditions. And in Figure 4.11, all the Pareto front data are exported and then used to plot the Pareto front diagram as shown in Figure 4.10. The concept of Pareto method was originally introduced by Francis Ysidro, and then generalized by Vilfredo Pareto [58]. By comparing each

solution to every other solution, those solutions dominated by any other for all objectives are flagged as inferior [59].

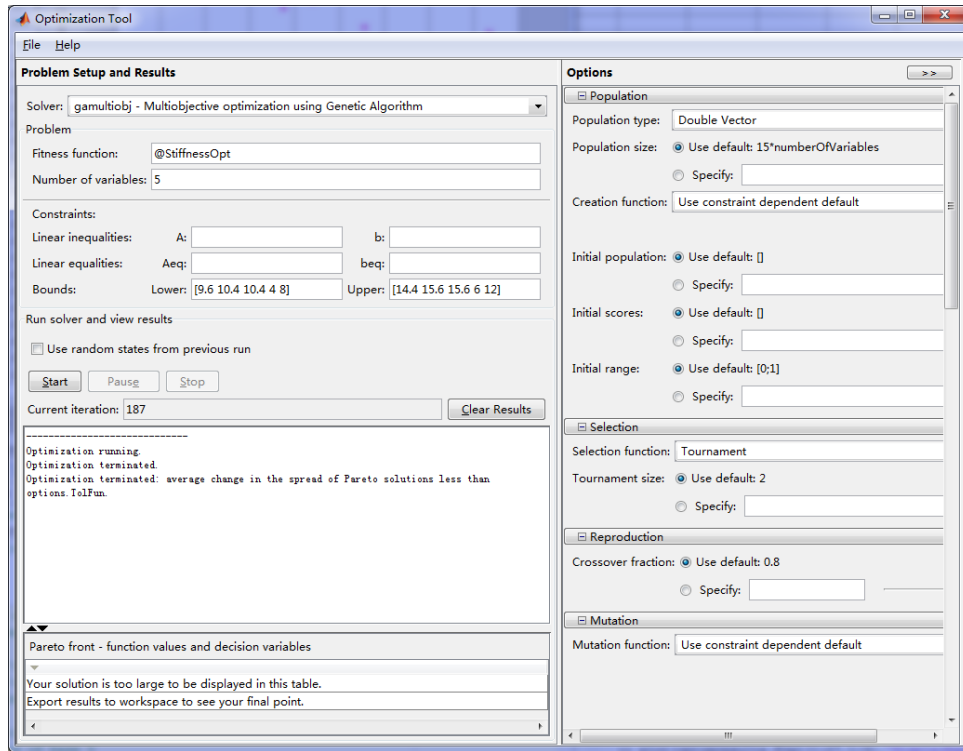


Figure 4.9. Multiobjective optimization and results.

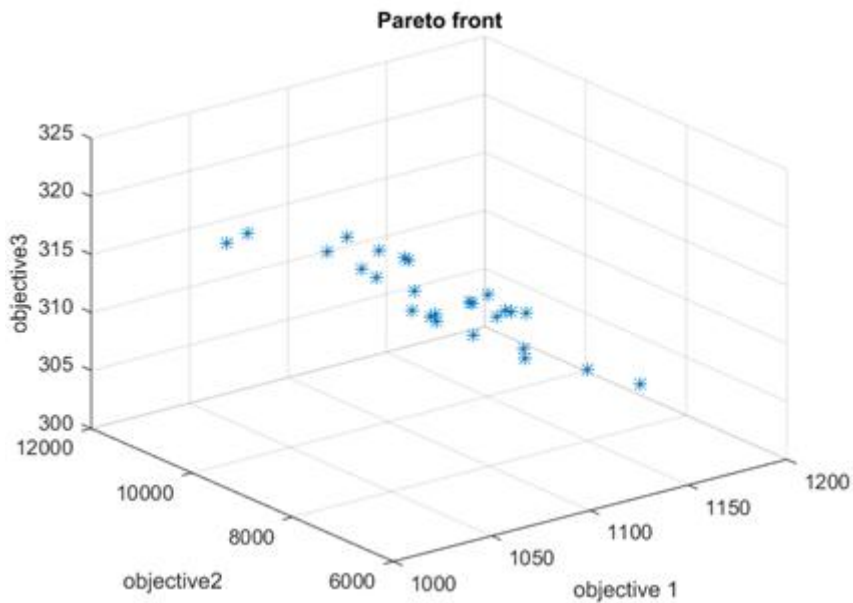


Figure 4.10. Pareto front data plot of multiobjective optimization results.

	1	2	3
1	-1.0170e+03	-6.4477e+03	-324.6757
2	-1.1624e+03	-7.4341e+03	-305.4629
3	-1.1522e+03	-1.1081e+04	-304.3501
4	-1.1406e+03	-1.0653e+04	-306.2657
5	-1.1242e+03	-1.0493e+04	-307.6233
6	-1.1557e+03	-9.4601e+03	-304.1418
7	-1.1055e+03	-8.6036e+03	-312.8063
8	-1.0275e+03	-7.3577e+03	-323.0952
9	-1.0170e+03	-6.4477e+03	-324.6757
10	-1.0891e+03	-7.2507e+03	-315.3665
11	-1.0206e+03	-6.5170e+03	-324.1506
12	-1.0555e+03	-7.7433e+03	-317.5159
13	-1.0891e+03	-7.9086e+03	-314.7732
14	-1.0949e+03	-8.9599e+03	-311.3047
15	-1.0832e+03	-6.8930e+03	-316.1610
16	-1.0195e+03	-8.0593e+03	-321.9746
17	-1.1501e+03	-1.0273e+04	-304.7640
18	-1.0231e+03	-9.7970e+03	-320.0059
19	-1.0693e+03	-6.8211e+03	-318.4405
20	-1.0943e+03	-7.0562e+03	-315.2298
21	-1.0055e+03	-9.5295e+03	-320.5691
22	-1.0838e+03	-9.6134e+03	-313.9855
23	-1.0541e+03	-8.7350e+03	-317.6270
24	-1.1150e+03	-8.4390e+03	-311.4621
25	-1.1517e+03	-9.3444e+03	-305.3587
26	-1.1582e+03	-8.3384e+03	-305.1206
27	-1.0167e+03	-7.5820e+03	-324.2383

Figure 4.11. Exported Pareto Front data, stiffness results after optimization

Figure 4.10 shows the Pareto optimal solutions of this multiobjective optimization problem. From these solutions the designers can choose a solution based on the importance of the stiffness in which direction.

4.6 Summary

In the chapter, the optimization of workspace and stiffness, and multiobjective optimization are conducted using Genetic Algorithm with MATLAB Toolbox. The

results are shown in the tables which can be used to design the parallel robotic surgical instrument with better performance. Compared with those performance indices evaluated with preliminary parameters in chapter 2 and 3, it is obvious that the performance indices were improved.

Chapter 5 Design and Analysis of the Multifunctional Forceps

5.1 Introduction

During Minimally Invasive surgery, surgeons tend to switch between different types of surgical tools to perform various operations frequently. The frequent tool exchanges result in increased surgery time and reduced surgical efficiency.

Consequently, there is a urgent need in developing multifunctional tools which are able to perform multiple surgical tasks. The concept of a single tool being used to perform multiple surgical tasks is referred to as tool multifunctionality [60]. In addition to improving surgical efficiency using multifunctional tools, it can also limit the likelihood of iatrogenic injury by reducing the frequency of instrument exchanges [61]. Moreover, reduced surgery times and mitigation in potential injuries decrease the invasiveness of MIS [60].

Frecker et al. conducted a study of instrument utilization for laparoscopic to evaluate the dynamics of instrument maneuver and exchange [62], which demonstrated that a combination of curved dissector (forceps)-scissors instrument that could be used to cut, dissect, and hold tissue during clipping was identified as a useful multifunctional surgical instrument [60]. Alcon Manufacturing, Ltd. has also

conducted a similar instrument utilization study for vitreoretinal surgery [63]. These studies show that surgeons may modify their current surgical techniques for Minimally Invasive Surgery if multifunctional forceps-scissors instruments are available and useful, surgeons may be likely to modify their current surgical techniques [63].

5.2 Multifunctional Forceps Geometric Structure and Design

Since many advantages were found in using multifunctional forceps during the Minimally Invasive Surgeries, it would bring great benefits to both the surgeons and patients if more multifunctional forceps are developed and introduced to be used in MIS. This study focuses on a multifunctional forceps capable of scissor-cutting and grasping. With such instrument surgeons can conduct MIS procedures more freely without worrying about switching between these two instruments, forceps and scissors, and thus shorten the surgery time significantly.

The 3D design of multifunctional forceps-scissors instrument is shown in Figure 5.1. In this proposed design, one jaw of the forceps with a piece of scissor blade is fixed, attaching to the base as shown in the figure. Another jaw is pinned with the fixed jaw, which is connected with the actuators with pin as well. This jaw is actuated to rotate around the pin connecting the fixed jaw and the moving jaw. When the linear piezoelectric actuator is dragging the shaft downwards, the forceps closes, ready to

cut tissues or to grasp tissues. Since the grasping jaws were designed with a curve going upwards, angled with the cutting blades, they would not interfere with the cutting function. And in turns when using the grasping function, the scissors would not just cut good tissues by accident since the scissors cutting blades were designed behind of the grasping jaws and they are not in the same plane with the grasping jaws. This design provides adequate cutting and grasping functions and avoids unwanted injuries to the tissue. Figure 5.2 and 5.3 present the design of multifunctional forceps from different view. In Figure 5.2, the grasping surfaces were designed larger and small teeth were added to the inner grasping surfaces to improve the gripping ability.

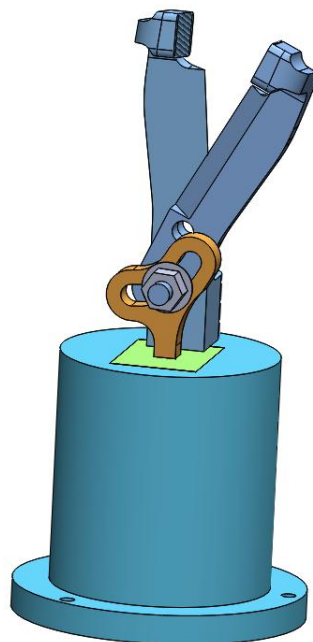


Figure 5.1. 3D model of the multifunctional forceps mounted on the upper base, actuated by a linear piezoelectric motor.

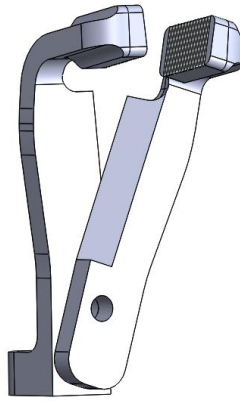


Figure 5.2. 3D model of the fixed jaw (left), and the moving jaw (right).

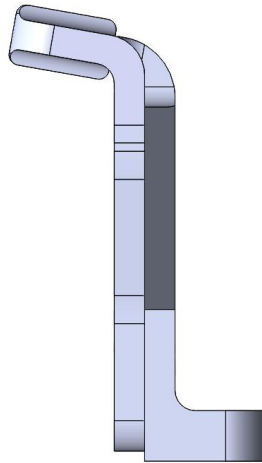


Figure 5.3. Side view of the 3D model of multifunctional forceps-scissors.

5.3 Design Constraints and Parameters

Considering the fabrication feasibility and surgical practicality, the design constraints can be set up and used to instruct the parameters of this design. Since the relatively low cost and the ability to generate needed features for the design, the manufacturing method of Wire electrical discharge machining (EDM) was chosen to fabricate the

multifunctional forceps.

The constraints imposed by the limitations of the EDM fabrication method are 0.15 mm minimum thickness and 0.25 mm minimum diameter for machined holes. For surgical practicality [39], the forceps are required to be able open a minimum angle of 90° to operate on adequate amount of tissues. The working lengths of cutting blades should be 10 mm at minimum to cut tissues effectively. Based on the surgical experience, the graspers are desired to be able to apply 1-2 N of grasping force without yielding. Such force would be necessary to grasp and manipulate tissue during surgery. Additionally, the length of inner grasping surface is required to be at least 5 mm to secure enough force can be applied to adequate amount of tissue.

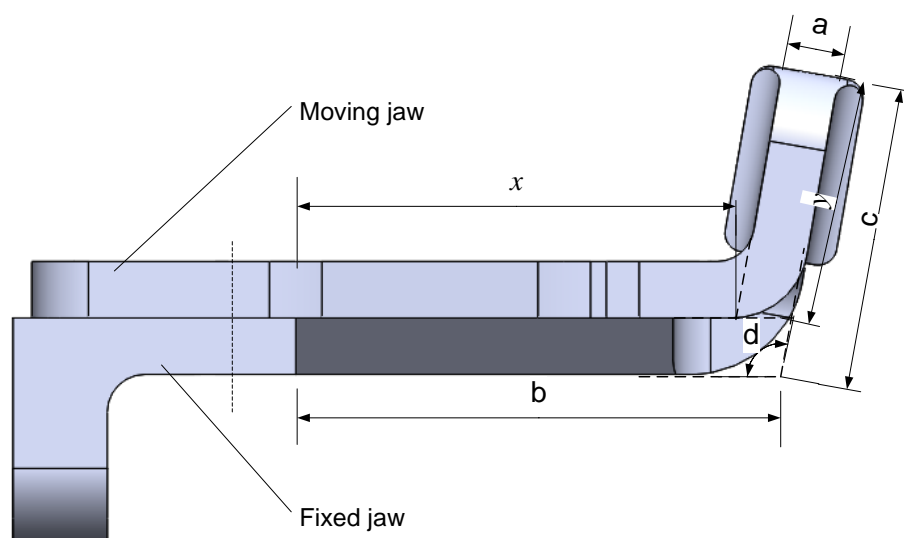


Figure 5.4. Representation of the jaw design with parameters.

Figure 5.4 shows the jaw geometry and design parameters. In this figure, the design parameters of the fixed jaw was first considered, the thickness a ; the length b

measured from the lower edge of the cutting blade to the extension of the curvature of the grasper; the length c ; and the angle d between b and c . Since the grasping surfaces are desired to match with each other, the design of the moving jaw are required to be based on the design parameters of the fixed jaw, which can be expressed as the equation (5.1) and (5.2).

$$x = b + a/\tan (\pi - d) , \quad (5.1)$$

$$y = c - a/\sin (\pi - d) , \quad (5.2)$$

where the length x is measured from the lower edge of the cutting blade of the moving jaw to the extension of the curvature of the grasper as shown in the Figure 5.4.

Besides, the grasping surface was designed with the geometry of at least 5×3 mm² to provide enough grasping force and enough area to manipulate a multitude of tissue.

5.4 Finite Element Modeling of the Multifunctional Forceps

Finite Element Modeling was applied to the design of the multifunctional forceps to verify that with the designed parameters the forceps can withstand the grasping forces as required without yielding. During this FEA, the fixed jaw and the moving jaw were examined respectively to determine whether the proposed design met the minimum grasping force of 2N. Through repetition of Finite Element Modeling with different geometric parameters, the dimensional parameters can be modified to improve the

grasping and cutting capability, as well as the stress and strain distribution.

The material for the jaws were chosen to be 316 stainless steel due to its high yield strength, machinability, and biocompatibility [39]. Relevant material properties of 316 stainless steel are given in Table 5.1.

Table 5.1. Relevant material properties for 316 stainless steel.

Property	Value
Young's modulus, E	193 GPa
Poisson's ratio, ν	0.3
Yield strength, σ_y	240 MPa

As the Figure 5.5 shows, the FEA model was simplified by removing the small teeth on the grasping surface, which would not affect the simulation result significantly.

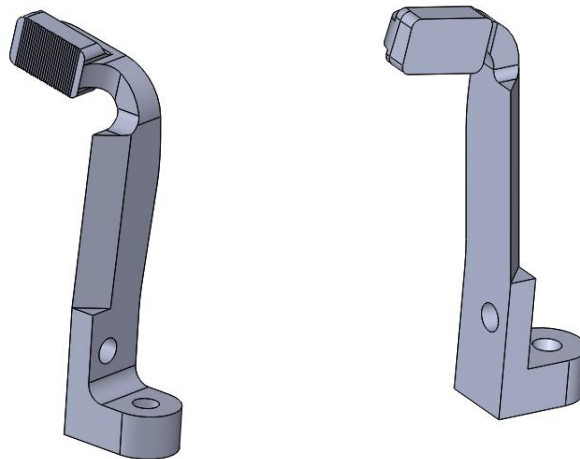


Figure 5.5. Jaw geometry with small teeth (left), FEA model geometry without small teeth (right).

The fixed jaw is attached to a base through a pin, so the pin hole is fixed and constrained as shown in Figure 5.6. The force of 2N was applied to the grasping surface. After meshing in SolidWorks and then the Finite Element Analysis was conducted, with the results displayed in Figure 5.7 to 5.8 , showing the von Mises stress, the displacement and strain respectively. Among these results, the stress distribution draws the most attention, since we need the surgical tool be safe during the surgeries, meaning the largest stress should not pass the yield strength of the material applied to the forceps. From the given result of stress, the largest stress is about $2.546e07$, which is much lower than the yield strength $1.379e08$. The safety factor is around 5. Therefore, this design meets the requirements of this application.

The same analysis process applies to the moving jaw. And from the results shown in Figure 5.10 to 5.11 .we can draw the conclusion that the design of Jaw 2 also met the requirements of this application.

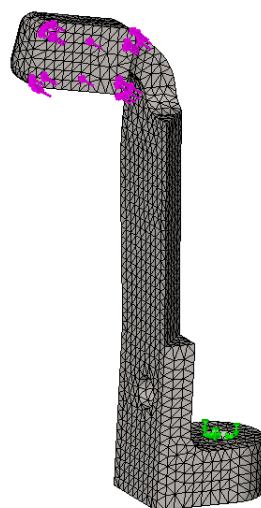


Figure 5.6. 2N force is applied to the grasping surface and the fixed jaw was fixed at the pin hole and meshed.

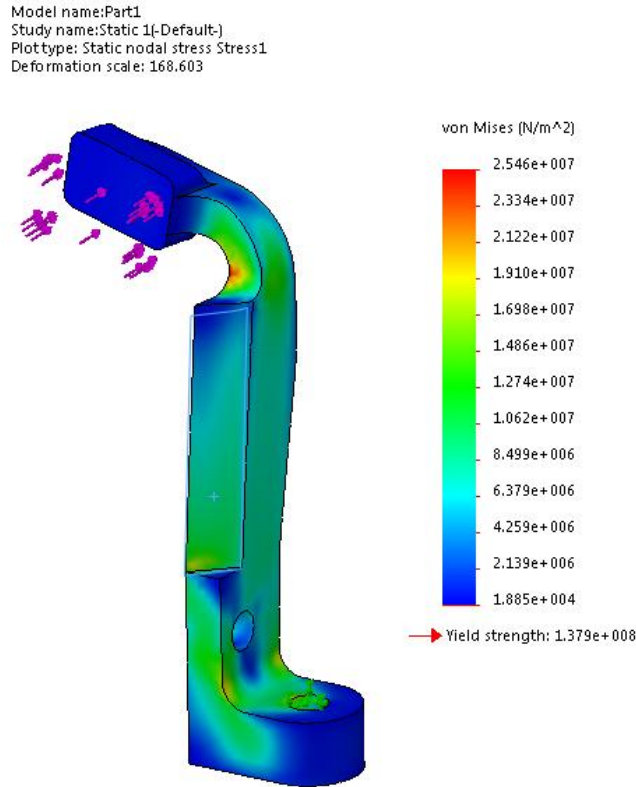


Figure 5.7. FEA result of stress distribution of the fixed jaw.

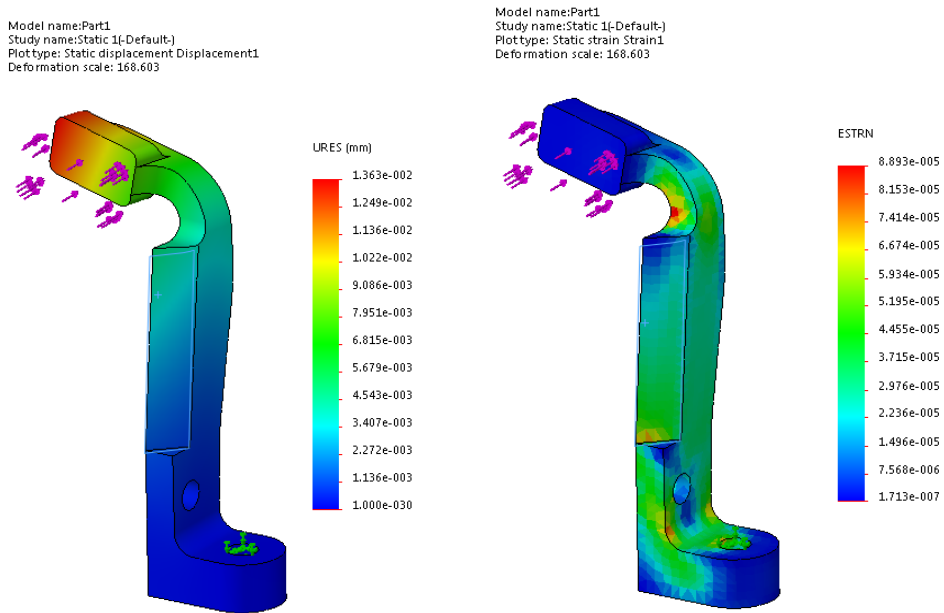


Figure 5.8. FEA result of displacement (left) and strain distribution (right) of the fixed jaw.

Note that the deformation scale is about 168 times as large as the original

deformation. For instance, the largest displacement of the jaw is around 0.01363 mm, which is totally unnoticeable and can be ignored in this application.

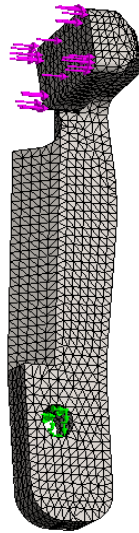


Figure 5.9. 2N force is applied to the grasping surface and the moving jaw was fixed at the pin hole and meshed.

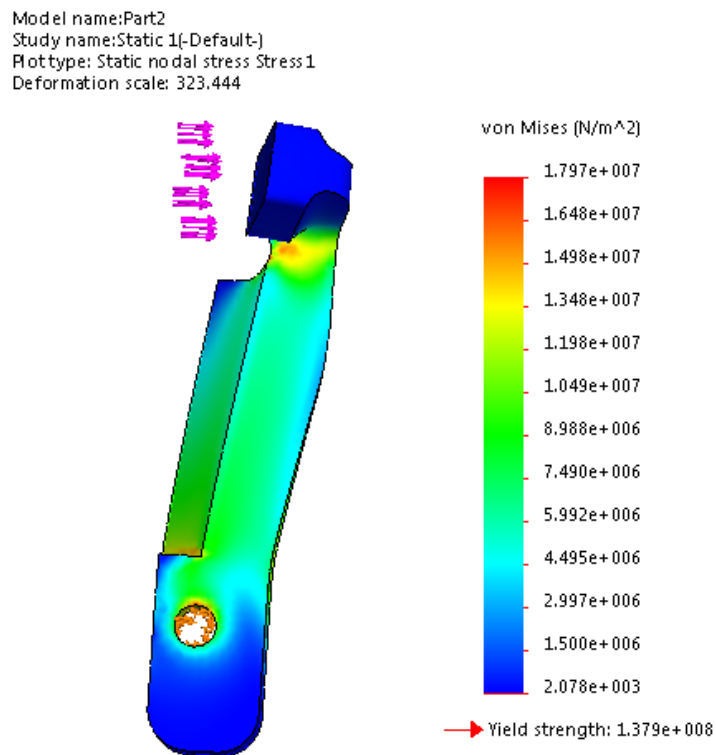


Figure 5.10. FEA result of stress distribution of the fixed jaw.

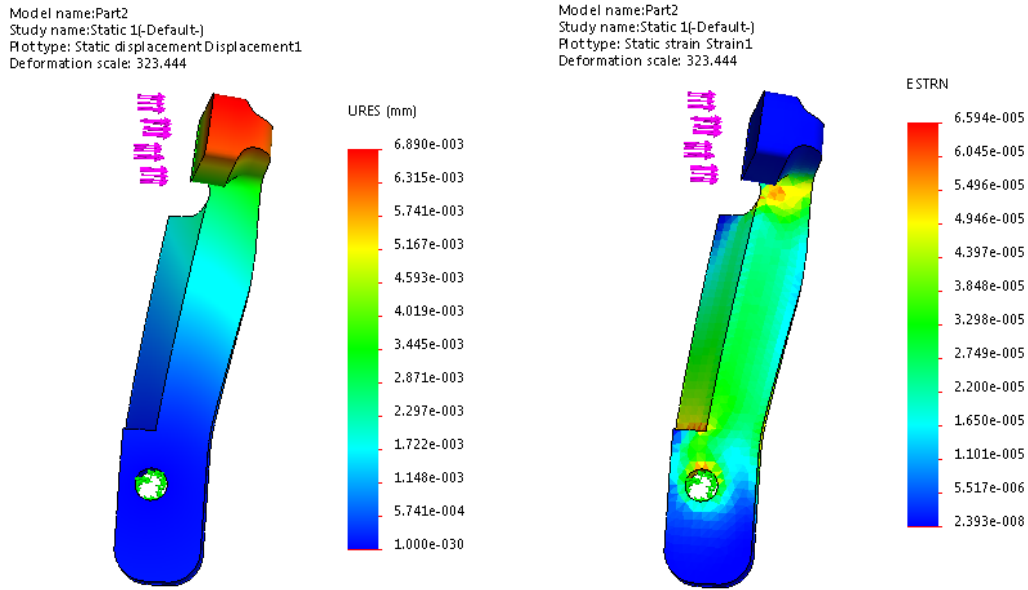


Figure 5.11. FEA result of displacement (left) and strain distribution (right) of the fixed jaw.

5.5 Integration of Cautery Ability

The cauterization is a technique often used in surgery to dissect tissues or stop the bleeding in tissues by causing blood coagulation with thermal energy applied to tissues through surgical tools [64, 66, 67]. If the Cautery ability can be integrated to the multifunctional forceps, then the forceps can be extended to have more utilities other than cutting and grasping, and thus further improve the effectiveness in MIS.

During Cautery process, the surgical tool, generally a metal probe is heated by electric current, known as Joule heating, and then used to cauterize tissues. Thus, the tissues are included in the electrical current [66, 69]. The cautery can be categorized

into two types, unipolar and bipolar, by the difference of the way the electrode is placed and the difference in size between the supply and return electrodes [66, 70].

In unipolar cauterization, the surgeon approaches the tissue with a small supply electrode with a grounding pad placed on the patient to complete the electric circuit. Since the current travels through the patient's body as pictured in Figure 5.12, the unipolar needs more current than bipolar. However, the deeper penetration of thermal damage can be yielded [70] and this type of cauterization is preferred in some applications, including the hemostasis of gastric ulcers [70]. The drawback of this technique are including collateral damage to surrounding tissue, interference with other conductive medical implants [65, 66, 68]. Therefore, when a patient is implanted a pacemaker, this technique should be avoided.

Bipolar cautery passes the current between two tips of a forceps-like tool, one being a supply electrode and the other being the return electrode. Consequently, this technique includes a very small amount of tissue in the circuit. The advantage of bipolar technique is that it can obtain highly thermal damage to the tissue accurately without too much temperature rise in the surrounding tissue [71] as the current path is limited and the current can be focused and delivered to that part of the tissue in between the electrodes. These two techniques both have their own advantages and disadvantages. Nonetheless, one or both can be used to operate cauterization while still can achieve desirable clinical outcomes depending on the surgical needs and patient's condition.

The amount of heat generated depends on size of contact area, power setting or frequency of current, duration of application, and waveform. To avoid the electrocution, the output frequency used to implement cauterization is elevated [66], as shown in Figure 5.13.

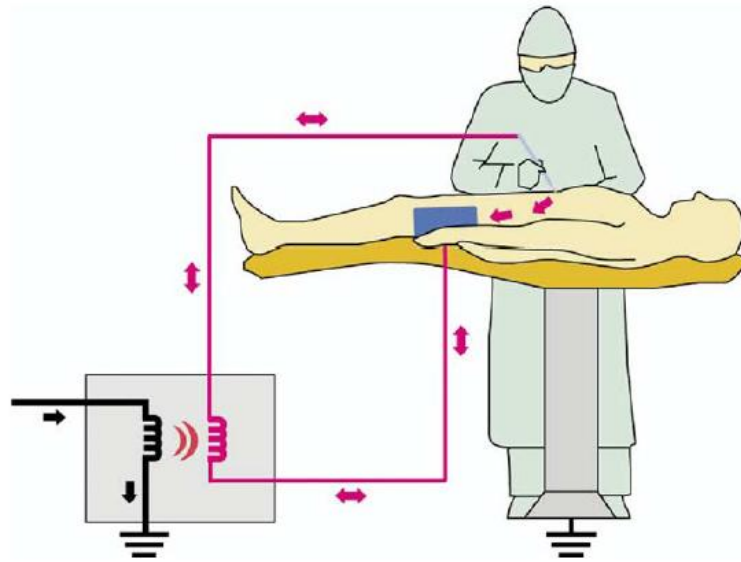


Figure 5.12. Diagram of current paths for unipolar Cautery technique. [66]

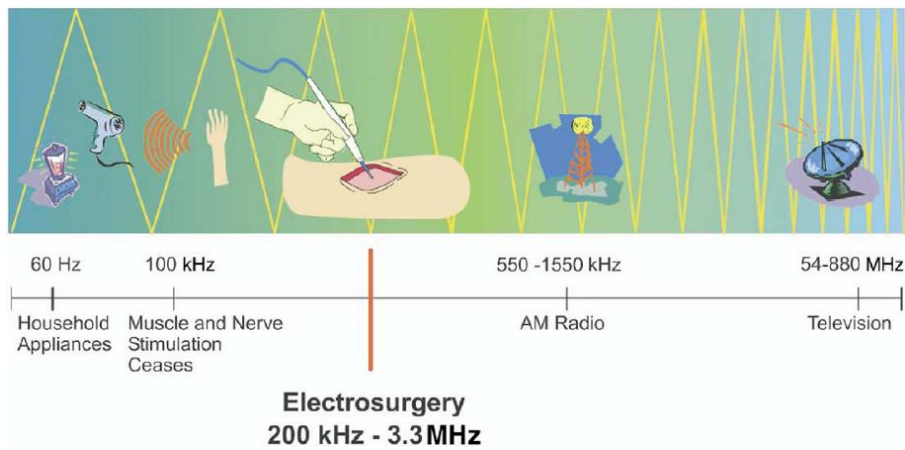


Figure 5.13. Applications of different current frequencies [66]

There are two main parts in the Cautery system, the Cautery tools and the generators that provide electrical current. The Cautery system is designed to have different clinical outcomes since the cauterization may range from cutting and

ablating tissues to simple bleeding coagulation. This is realized by controlling the output of the generator and having different power settings like cut mode, coagulate mode, and some intermediate mode [66, 72]. These power settings can be obtained by modulating the magnitude of the applied voltage and the waveform used to deliver the electrical current, as shown in Figure 5.14.



Figure 5.14. Common voltage waveform outputs for electrosurgical generators [66].

One example of integrating the Cautery ability into a multifunctional surgical tool is shown in Figure 5.15. Eitenmueller et al. developed a bipolar multifunctional coagulation scissors in laparoscopic surgery. This tool is composed of scissors and a pushing rod working as conducting electrodes. The Cautery device was used in more than 160 laparoscopic surgeries and demonstrated minimal complication and positive performance [64] within a short period of time.

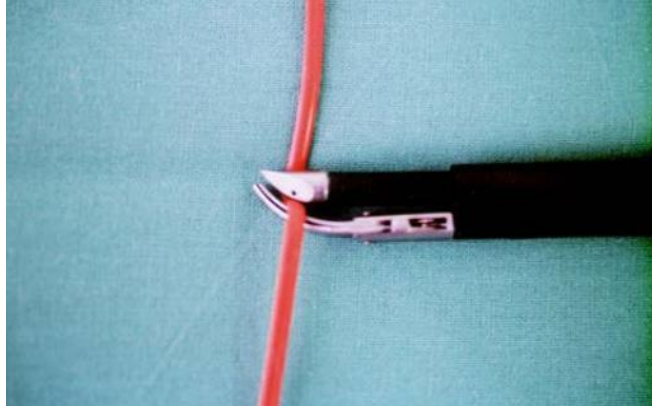


Figure 5.15. Tip of the instrument with forward pushed rod in coagulating position

[64].

5.6 Summary

In this chapter, the multifunctional forceps with scissor-cutting and grasping functions was introduced. The design of the forceps under the constraints was proposed, analyzed and modified to meet the requirements of the surgical application. Besides, the mechanical advantage was introduced and this concept was employed to optimize the design of multifunctional forceps by maximizing the mechanical advantage. Lastly, the Cautery ability integrated into the multifunctional forceps was introduced. Thus, such multifunctional forceps is capable of scissor-cutting, grasping and Cautery with only one single set of tool. This design would bring great benefits to both surgeons and patients since the surgery efficiency can be improved, and surgery time can be reduced.

Chapter 6 Conclusions, Contributions, and Future Work

6.1 Conclusions

In conclusion, this work has proposed a compliant parallel robotic surgical instrument with multifunctional forceps for Minimally Invasive Surgery. This idea is attempting to cope with the drawbacks of the existing surgical tools which are composed of rigid interacting components. These drawbacks are holding this MIS technique from advancing further to become more invasive, more versatile to different types of surgeries. This thesis first introduces the compliant parallel mechanism by describing its geometry. It is followed by looking into the kinematics analysis, including mobility calculation, inverse kinematics, and Jacobian derivation. Once the kinematics analysis is obtained, we can understand what the parameters are that determine the workspace, and then this thesis continues to evaluate the workspace of the compliant parallel mechanism in MATLAB. The workspace is an important index to parallel mechanism, even though it is small compared with its serial counterpart. By varying the values preliminary parameters, the workspace and its volume are obtained and it is found out that the workspace is not optimal. Therefore, the workspace is optimized later using Genetic Algorithm with respect to relevant parameters. As the results show, the

workspace is improved about 50% after the optimization.

The stiffness is another important index to parallel mechanism. Since this parallel mechanism developed in this study is compliant, the stiffness modeling of compliant mechanism is very different from that of its rigid counterpart. The stiffness modeling of one limb is fully explained as the other two limbs are identical. There are serial chains and parallel structures even in one limb. Therefore, the stiffness modeling of one limb deals with the stiffness and compliance matrices of these serial chains and parallel structures by the means of matrix method and transformation matrices. When the stiffness modeling of one limb is completed, the stiffness modeling of the parallel mechanism is at hand since three identical limbs are spreading evenly in 360 degree. The stiffness mapping in different directions with respect to various parameters are presented and illustrated. The results are analyzed. The optimization of stiffness is also conducted later in MATLAB using the method of Genetic Algorithm. Since the stiffness in different directions are preferable to be as large as possible, the stiffness in three directions, namely x, y, and z are taken into consideration for multiobjective optimization. The Pareto Front of the results are displayed, however, the decision maker have to decide what values to use to design the parallel mechanism as they can achieve their largest at the same time. Therefore, one has to make a decision which has the most priority and which to “sacrifice”.

Based on the extensive review of previous work done by researchers in the literature and the existing product in the market, the requirements and constraints for the design of the multifunctional forceps were defined. The dimensional geometry of

the forceps also considered that fabrication limitation. Then the 3D model of the multifunctional forceps was built in SolidWorks and the Finite Element Analysis was conducted to verify that the design meets the requirements. The multifunctional forceps is capable of scissor-cutting and grasping. In order to make the surgical instrument more versatile, the electric Cautery ability was also considered in this study to be integrated into this tool.

Overall, this thesis put forward a novel, compact, dexterous, multiple degree-of-freedom conceptual design of a compliant parallel robotic surgical instrument for MIS. Meanwhile, the forceps is multifunctional, convenient and reliable. The ideas proposed in this thesis might be able to contribute to the advances in MIS procedures and helping more patients in the future.

6.2 Contributions

This thesis has contributed to proposing the idea and the design by employing the compliant parallel mechanism to develop the surgical instrument that could lead to advances in Minimally Invasive Surgery. For the compliant parallel mechanism, the Lamina Emergent Mechanisms are adopted in this parallel mechanism making it really compact and easy to scale down, meanwhile achieving large displacement and multiple degrees of freedom. This new design has yielded a satisfactory result towards coping with the challenges arise from the advances of MIS.

This thesis has also studied the compliant parallel mechanism thoroughly by investigating the kinematics of it by the means of vector-loop equation. With the kinematics being studied, the performance of this mechanism then can be disclosed and understood. Therefore, this thesis continues to find out the workspace of this compliant parallel mechanism by calculating all the reachable points, and at the same time the volume and the workspace can be displayed in the graph simultaneously. Another performance index of the compliant parallel mechanism, the stiffness has been found by constructing the model for one limb first and then for the whole mechanism which consists of three identical limb. These stiffness modeling are established through matrix method and transformation matrices, considering the flexure hinges in a serial chain and/or in a parallel structure.

The performance indices of the compliant parallel mechanism, workspace and stiffness, have been improved significantly by performing Genetic Algorithm optimization separately in MATLAB. The multiobjective optimization problem has been constructed and solved as well with Genetic Algorithm in MATLAB.

This thesis has gone through a big amount of research papers, product dialogues to set up the constraints and provides the geometric information for designing the multifunctional forceps. And the forceps has been designed within the constraints and tested reliable to be capable of three-fold functions: scissor-cutting, grasping and electric Cautery.

Lastly, this thesis provides the investigation into the piezo motors which could be

used to actuate the mechanisms and to enable the end effector to rotate completely. The investigation presented in this thesis have led to the integration of rotational function to the instrument which is predicted to be very practical.

In conclusion, this thesis has designed a conceptual compliant parallel robotic surgical instrument, which can be inserted into human body to do the surgical operations effectively, particularly when this instrument is coupled with multifunctional forceps.

6.3 Future Work

This thesis has studied the properties and performances of the compliant parallel mechanism and optimized the performances. Besides, the multifunctional forceps has been designed and examined through FEA verification. However, there are still some work can be done to carry on this study and improve this surgical instrument.

The previous chapter has derived and analyzed the kinematics of the compliant parallel mechanism, however, the dynamics analysis of the mechanism can be conducted to facilitate the control of the mechanism with more accuracy. Besides, control algorithm should also be investigated in the future to cope with the problems such as the tremor of surgeon's hand during the operations.

The prototype of the compliant parallel mechanism can be fabricated based on the

design. With the prototypes, experiments can be conducted to verify the functionalities and the real movements and displacements although these analyses have been performed throughout this study. Experiments can also show the potential problems of the conceptual design. Afterwards the mechanism can be further optimized and improved based on the experiments.

There have been some investigation about the piezoelectric actuators in this thesis. However, with the fast developments in the field of piezoelectric motors and other actuators, there will be very likely that more powerful actuators with smaller size will be available in the market soon. Since the limitations of the actuators in the existing market, the size of the instrument might not be satisfactory compared with the demands of the advances in the MIS. Therefore, the investigation into the actuators can be done again in the future. If appropriate actuators are in the market, then this complaint parallel mechanism can be further miniaturized to be more compact, which could contribute to the advances in MIS significantly.

The prototype of the multifunctional forceps should also be fabricated to optimize some geometric parameters, for example the angle between the cutting blade and the grasper. Experiments should be conducted to see how much the angle should be in order that the cutting blade can cut tissues with the least interference from the grasper, and the grasper can grasp tissues without unwanted cut into the good tissues.

Since the electric Cautery ability has been integrated into the multifunctional forceps in the design stage, the thermal effect on the forceps should be analyzed

through experiments. By experiments, the effectiveness of the electric Cautery can be found and then the design of the forceps could be modified to meet the requirements from this medical application in MIS.

References

- [1] https://en.wikipedia.org/wiki/Minimally-invasive_procedures
- [2] Vecchio, R., MacFayden, B. V., & Palazzo, F. (2000). History of laparoscopic surgery. *Panminerva medica*, 42(1), 87-90.
- [3] Salerno, M., Zhang, K., Menciassi, A., & Dai, J. S. (2014). A Novel 4-DOFs Origami Enabled, SMA Actuated, Robotic End-Effector for Minimally Invasive Surgery. In *Robotics and Automation (ICRA), 2014 IEEE International Conference on* (pp. 2844-2849). IEEE.
- [4] Aguirre, M. E., & Frecker, M. (2008). Design innovation size and shape optimization of a 1.0 mm multifunctional forceps-scissors surgical instrument. *Journal of Medical Devices*, 2(1), 015001.
- [5] Yamashita, H., Hata, N., Hashizume, M., & Dohi, T. (2004). Handheld laparoscopic forceps manipulator using multi-slider linkage mechanisms. In *Medical Image Computing and Computer-Assisted Intervention–MICCAI 2004* (pp. 121-128). Springer Berlin Heidelberg..
- [6] Lim, J. J., & Erdman, A. G. (2003). A review of mechanism used in laparoscopic surgical instruments. *Mechanism and Machine Theory*, 38(11), 1133-1147.
- [7] Aguirre, M. E., & Frecker, M. (2007). Size and Shape Optimization of a 1.0 mm Multifunctional Forceps-Scissors Instrument for Minimally Invasive Surgery. In *ASME 2007 International Design Engineering Technical Conferences and*

Computers and Information in Engineering Conference (pp. 671-679). American Society of Mechanical Engineers.

[8] <http://worldofvirtualsurgery.synthasite.com/>

[9] Herder, J. L., Horward, M. J., & Sjoerdsma, W. (1997). A laparoscopic grasper with force perception. *Minimally Invasive Therapy & Allied Technologies*, 6(4), 279-286.

[10] Jansen, A. (1993). Laparoscopic-assisted colon resection. Evolution from an experimental technique to a standardized surgical procedure. In *Annales chirurgiae et gynaecologiae* (Vol. 83, No. 2, pp. 86-91).

[11] Moyer, M. T., Pauli, E. M., Haluck, R. S., & Mathew, A. (2007). A self-approximating transluminal access technique for potential use in NOTES: an ex vivo porcine model (with video). *Gastrointestinal endoscopy*, 66(5), 974-978.

[12] Hawes, R. H., Rattner, D. W., ... & Thompson, C. C. (2008). NOTES™: where have we been and where are we going?. *Gastrointestinal Endoscopy*, 67(6), 779-780.

[13] Rattner, D., & Kalloo, A. (2006). ASGE/SAGES working group on natural orifice transluminal endoscopic surgery. *Surgical Endoscopy and Other Interventional Techniques*, 20(2), 329-333.

[14] <http://www.davincisurgery.com/da-vinci-urology/conditions/kidney-disorders/treatment.php>

[15] <http://www.intuitivesurgical.com/>

[16] Frede, T., Hammady, A., Klein, J., Teber, D., Inaki, N., Waseda, M., ... & Rassweiler, J. (2007). The Radius Surgical System—a new device for complex

- minimally invasive procedures in urology?. *European urology*, 51(4), 1015-1022.
- [17] Vitale, G. C., Sanfilippo, J. S., & Perissat, J. (1995). *Laparoscopic surgery: an atlas for general surgeons*. Lippincott Williams & Wilkins.
- [18] Kota, S., Lu, K. J., Kreiner, Z., Trease, B., Arenas, J., & Geiger, J. (2005). Design and application of compliant mechanisms for surgical tools. *Journal of biomechanical engineering*, 127(6), 981-989.
- [19] Lim, J. J., & Erdman, A. G. (2003). A review of mechanism used in laparoscopic surgical instruments. *Mechanism and Machine Theory*, 38(11), 1133-1147.
- [20] Arata, J., Saito, Y., & Fujimoto, H. (2010). Outer shell type 2 DOF bending manipulator using spring-link mechanism for medical applications. In *Robotics and Automation (ICRA), 2010 IEEE International Conference on* (pp. 1041-1046). IEEE.
- [21] Salerno, M., Zhang, K., Menciassi, A., & Dai, J. S. (2014). A Novel 4-DOFs Origami Enabled, SMA Actuated, Robotic End-Effector for Minimally Invasive Surgery. In *Robotics and Automation (ICRA), 2014 IEEE International Conference on* (pp. 2844-2849). IEEE.
- [22] Rotinat-Libersa, C., & Solano, B. (2012). Optimal Design of Compliant Joint and Gripper for Miniature Robotic Devices: Application to Surgery. In *ASME 2012 International Design Engineering Technical Conferences and Computers and Information in Engineering Conference* (pp. 393-402). American Society of Mechanical Engineers.
- [23] Stapel, A., & Herder, J. L. (2004). Feasibility study of a fully compliant statically balanced laparoscopic grasper. In *ASME 2004 International Design Engineering*

Technical Conferences and Computers and Information in Engineering Conference (pp. 635-643). American Society of Mechanical Engineers.

[24] Lassooij, J., Tolou, N., Tortora, G., Caccavaro, S., Menciassi, A., & Herder, J. L. (2012). A statically balanced and bi-stable compliant end effector combined with a laparoscopic 2DoF robotic arm. *Mechanical Sciences*, 3 (2), 2012.

[25] Jacobsen, J. O., Winder, B. G., Howell, L. L., & Magleby, S. P. (2010). Lamina emergent mechanisms and their basic elements. *Journal of Mechanisms and Robotics*, 2(1), 011003.

[26] Lusk, C. P., & Howell, L. L. (2006). Design space of single-loop planar folded micro mechanisms with out-of-plane motion. *Journal of Mechanical Design*, 128(5), 1092-1100.

[27] Gollnick, P. S., Black, J. D., Savage, E. E., Bowen, L. A., Qiu, L., Magleby, S. P., & Howell, L. L. (2011, January). A preliminary study of actuation approaches for lamina emergent mechanisms. In *ASME 2011 International Design Engineering Technical Conferences and Computers and Information in Engineering Conference* (pp. 191-202). American Society of Mechanical Engineers.

[28] Jacobsen, J. O., Chen, G., Howell, L. L., & Magleby, S. P. (2009). Lamina emergent torsional (LET) joint. *Mechanism and Machine Theory*, 44(11), 2098-2109.

[29] Wilding, S. E., Howell, L. L., & Magleby, S. P. (2012). Introduction of planar compliant joints designed for combined bending and axial loading conditions in lamina emergent mechanisms. *Mechanism and Machine Theory*, 56, 1-15.

[30] Winder, B. G., Magleby, S. P., & Howell, L. L. (2008). A study of joints suitable

for lamina emergent mechanisms. In *ASME 2008 International Design Engineering Technical Conferences and Computers and Information in Engineering Conference* (pp. 339-349). American Society of Mechanical Engineers.

[31] Ferrell, D. B., Isaac, Y. F., Magleby, S. P., & Howell, L. L. (2011). Development of criteria for lamina emergent mechanism flexures with specific application to metals. *Journal of Mechanical Design*, 133(3), 031009.

[32] Gollnick, P. S. (2010). Design Principles and Preliminary Actuation Approaches for Novel Multiple-Layer Lamina Emergent Mechanisms.

[33] Melzer, A. (1996). Endoscopic instruments: conventional and intelligent. *Endosurgery*. New York: Churchill Livingstone, 69-95.

[34] Mehta, N. Y., Haluck, R. S., Frecker, M. I., & Snyder, A. J. (2002). Sequence and task analysis of instrument use in common laparoscopic procedures. *Surgical Endoscopy And Other Interventional Techniques*, 16(2), 280-285.

[35] Frecker, M. I., Schadler, J., Haluck, R. S., Culkar, K., & Dziedzic, R. (2005). Laparoscopic multifunctional instruments: design and testing of initial prototypes. *JSLs, Journal of the Society of Laparoendoscopic Surgeons*, 9(1), 105-112.

[36] Frecker, M., & Snyder, A. J. (2005). Surgical robotics: multifunctional end effectors for robotic surgery. *Operative Techniques in General Surgery*, 7(4), 165-169.

[37] Aguirre, M. E., & Frecker, M. (2008). Design innovation size and shape optimization of a 1.0 mm multifunctional forceps-scissors surgical instrument. *Journal of Medical Devices*, 2(1), 015001.

- [38] Frecker, M. I., Powell, K. M., & Haluck, R. (2005). Design of a multifunctional compliant instrument for minimally invasive surgery. *Journal of biomechanical engineering*, 127(6), 990-993.
- [39] Rau, A. C., Frecker, M., Mathew, A., & Pauli, E. (2011). Multifunctional Forceps for Use in Endoscopic Surgery—Initial Design, Prototype, and Testing. *Journal of Medical Devices*, 5(4), 041001.
- [40] Balázs, M., Feussner, H., Hirzinger, G., Omote, K., & Ungeheuer, A. (1998). A new tool for minor-access surgery. *Engineering in Medicine and Biology Magazine, IEEE*, 17(3), 45-48.
- [41] Sastry, S. S., Cohn, M., & Tendick, F. (1997). Milli-robotics for remote, minimally invasive surgery. *Robotics and Autonomous Systems*, 21(3), 305-316.
- [42] Cohn, M. B., Crawford, L. S., Wendlandt, J. M., & Sastry, S. S. (1995). Surgical applications of milli - robots. *Journal of robotic systems*, 12(6), 401-416.
- [43] Kolesa, M. S., Aranyi, E., & Kappel, G. S. (1997). *U.S. Patent No. 5,609,601*. Washington, DC: U.S. Patent and Trademark Office.
- [44] Oren, R., & Moor, D. (2000). *U.S. Patent No. 6,102,925*. Washington, DC: U.S. Patent and Trademark Office.
- [45] Bacher, U. (2001). *U.S. Patent No. 6,299,625*. Washington, DC: U.S. Patent and Trademark Office.
- [46] Tsai, L. W. (1999). *Robot analysis: the mechanics of serial and parallel manipulators*. John Wiley & Sons.
- [47] Lobontiu, N. (2002). *Compliant mechanisms: design of flexure hinges*. CRC

press.

[48] Li, Y., & Xu, Q. (2006). Kinematic analysis and design of a new 3-DOF translational parallel manipulator. *Journal of Mechanical Design*, 128(4), 729-737.

[49] Tsai, L. W., & Joshi, S. (2002). Kinematic analysis of 3-DOF position mechanisms for use in hybrid kinematic machines. *Journal of Mechanical Design*, 124(2), 245-253.

[50] Pham, H. H., & Chen, I. M. (2005). Stiffness modeling of flexure parallel mechanism. *Precision Engineering*, 29(4), 467-478.

[51] Koseki, Y., Tanikawa, T., Koyachi, N., & Arai, T. (2002). Kinematic analysis of a translational 3-dof micro-parallel mechanism using the matrix method. *Advanced Robotics*, 16(3), 251-264.

[52] Sciavicco, L., & Siciliano, B. (2012). *Modelling and control of robot manipulators*. Springer Science & Business Media.

[53] Yao J., Li L., Yang W., & Zhao Y. (2014). *Analytical calculation of compliance matrix for right-circular flexure spherical hinge*. Editorial Office of Optics and Precision Engineeri, 22(7), 1857-1863.

[54] Liang, Q., Zhang, D., Chi, Z., Song, Q., Ge, Y., & Ge, Y. (2011). Six-DOF micro-manipulator based on compliant parallel mechanism with integrated force sensor. *Robotics and Computer-Integrated Manufacturing*, 27(1), 124-134.

[55] Zhang, D., Gao, Z., & Fassi, I. (2011). Design optimization of a spatial hybrid mechanism for micromanipulation. *International Journal of Mechanics and Materials in Design*, 7(1), 55-70.

- [56] Pan, M., Zhang, D., & Chi, Z. (2011). Novel design of a three DOFs MEMS-based precision manipulator. In *Mechatronics and Automation (ICMA), 2011 International Conference on* (pp. 80-85). IEEE.
- [57] Zhang, D. (2009). *Parallel robotic machine tools*. Springer Science & Business Media.
- [58] Coello, C. A. C., Van Veldhuizen, D. A., & Lamont, G. B. (2002). *Evolutionary algorithms for solving multi-objective problems* (Vol. 242). New York: Kluwer Academic.
- [59] Fieldsend, J. E., & Singh, S. (2005). Pareto evolutionary neural networks. *Neural Networks, IEEE Transactions on*, 16(2), 338-354.
- [60] Frecker, M., & Snyder, A. J. (2005). Surgical robotics: multifunctional end effectors for robotic surgery. *Operative Techniques in General Surgery*, 7(4), 165-169.
- [61] Wafapoor, H., & Peyman, G. A. (1996). A new instrument (forceps/scissors) for preretinal membrane peeling, segmentation. *Archives of ophthalmology*, 114(1), 99-99.
- [62] Mehta, N. Y., Haluck, R. S., Frecker, M. I., & Snyder, A. J. (2002). Sequence and task analysis of instrument use in common laparoscopic procedures. *Surgical Endoscopy And Other Interventional Techniques*, 16(2), 280-285.
- [63] Cazzini, K., & Booth, D. (2004). Utilization Study of Ophthalmic Instruments. *Alcon Manufacturing, Ltd. Internal Report*.
- [64] Eitenmueller, J. P., & Volckmann, E. (2008). Clinical experience with bipolar multifunctional coagulation scissors in laparoscopic surgery. *Surgical*

endoscopy, 22(2), 421-425.

[65] Ayodeji, I. D., Hop, W. C. J., Tetteroo, G. W. M., Bonjer, H. J., & De Graaf, E. J. R. (2004). Ultracision Harmonic Scalpel and multifunctional tem400 instrument complement in transanal endoscopic microsurgery: a prospective study. *Surgical Endoscopy and Other Interventional Techniques*, 18(12), 1730-1737.

[66] Massarweh, N. N., Cosgriff, N., & Slakey, D. P. (2006). Electrosurgery: history, principles, and current and future uses. *Journal of the American College of Surgeons*, 202(3), 520-530.

[67] Dodde, R. E., Miller, S. F., Geiger, J. D., & Shih, A. J. (2008). Thermal-electric finite element analysis and experimental validation of bipolar electrosurgical cautery. *Journal of manufacturing science and engineering*, 130(2), 021015.

[68] Dumot, J. A., & Greenwald, B. D. (2008). Argon plasma coagulation, bipolar cautery, and cryotherapy: ABC's of ablative techniques. *Endoscopy*, 40(12), 1026-1032.

[69] Harrell, A. G., Kercher, K. W., & Heniford, B. T. (2004). Energy sources in laparoscopy. *Surgical Innovation*, 11(3), 201-209.

[70] Nduka, C. C., Super, P. A., Monson, J. R., & Darzi, A. W. (1994). Cause and prevention of electrosurgical injuries in laparoscopy. *Journal of the American College of Surgeons*, 179(2), 161-170.

[71] Ramsay, J. W. A., Shepherd, N. A., Butler, M., Gosling, P. T., Miller, R. A., Wallace, D. M. A., & Whitfield, H. N. (1985). A comparison of bipolar and monopolar diathermy probes in experimental animals. *Urological Research*, 13(2),

99-102.

[72] Rodriguez, S. A., Adler, D. G., Chand, B., Conway, J. D., Diehl, D. L., Kantsevoy, S. V., ... & Tierney, W. M. (2008). Mucosal ablation devices. *Gastrointestinal Endoscopy*, 68(6), 1031-1042.